UNIVERSIDADE FEDERAL DE MINAS GERAIS
Instituto de Ciências Exatas
Programa de pós-graduação em Física

Alessandra Chioquetta

STABILITY OF QUANTUM MANY-BODY SCARS ON THE PXP MODEL

Belo Horizonte
2025

Alessandra Chioquetta

STABILITY OF QUANTUM MANY-BODY SCARS ON THE PXP MODEL

Tese apresentada ao Programa de Pós-Graduação em Física do Instituto de Ciências Exatas da Universidade Federal de Minas Gerais como requisito parcial para obtenção do título de Doutor em Ciências.

Orientador: Raphael Campos Drumond

Belo Horizonte

2025

Dados Internacionais de Catalogação na Publicação (CIP)

C539s Chioquetta, Alessandra.
Stability of quantum many-body scars on the PXP model / Alessandra Chioquetta. – 2025.
94 f. : il.

Orientador: Raphael Campos Drumond.
Tese (doutorado) – Universidade Federal de Minas Gerais, Departamento de Física.
Bibliografia: f. 77-84.

1. Mecânica quântica. 2. Caos. I. Título. II. Drumond, Raphael Campos. III. Universidade Federal de Minas Gerais, Departamento de Física.

CDU – 530.145 (043)

Ficha catalográfica elaborada por Romário Martins Ribeiro – CRB6 3595
Biblioteca Professor Manoel Lopes de Siqueira – Departamento de Física - UFMG

UNIVERSIDADE FEDERAL DE MINAS GERAIS

INSTITUTO DE CIÊNCIAS EXATAS

COLEGIADO DO CURSO DE PÓS-GRADUAÇÃO EM FÍSICA

FOLHA DE APROVAÇÃO

A presente tese, intitulada **"Estabilidade de cicatrizes quânticas de muitos corpos no modelo PXP",** de autoria de **ALESSANDRA CHIOQUETTA** submetida à Comissão Examinadora, abaixo-assinada, foi aprovada para obtenção do grau de **DOUTOR EM CIÊNCIAS, área de concentração Física,** em vinte e três de outubro de 2025.

Belo Horizonte, 23 de outubro de 2025.

Prof. Raphael Campos Drumond
Orientador da estudante
Departamento de Matemática/UFMG

Profa. Maria Carolina de Oliveira Aguiar
Departamento de Física /UFMG

Prof. Leonardo Teixeira Neves
Departamento de Física /UFMG

Prof. Diogo de Oliveira Soares Pinto
FCI-USP-São Carlos

Prof. Lucas Chibebe Céleri
Instituto de Física/UFG

Documento assinado eletronicamente por **Maria Carolina de Oliveira Aguiar**, **Professora do Magistério Superior**, em 24/10/2025, às 11:43, conforme horário oficial de Brasília, com fundamento no art. 5º do Decreto nº 10.543, de 13 de novembro de 2020.

Documento assinado eletronicamente por **Diogo de Oliveira Soares Pinto**, **Usuário Externo**, em 24/10/2025, às 13:19, conforme horário oficial de Brasília, com fundamento no art. 5º do Decreto nº 10.543, de 13 de novembro de 2020.

Documento assinado eletronicamente por **Leonardo Teixeira Neves**, **Professor do Magistério Superior**, em 26/10/2025, às 18:34, conforme horário oficial de Brasília, com fundamento no art. 5º do Decreto nº 10.543, de 13 de novembro de 2020.

Documento assinado eletronicamente por **Raphael Campos Drumond**, **Professor do Magistério Superior**, em 28/10/2025, às 10:02, conforme horário oficial de Brasília, com fundamento no art. 5º do Decreto nº 10.543, de 13 de novembro de 2020.

Documento assinado eletronicamente por **Lucas Chibebe Céleri**, **Usuário Externo**, em

12/11/2025, às 15:54, conforme horário oficial de Brasília, com fundamento no art. 5º do Decreto nº 10.543, de 13 de novembro de 2020.

A autenticidade deste documento pode ser conferida no site https://sei.ufmg.br/sei/controlador_externo.php?acao=documento_conferir&id_orgao_acesso_externo=0, informando o código verificador **4671937** e o código CRC **A12481D6.**

Referência: Processo nº 23072.265097/2025-12 SEI nº 4671937

Agradecimentos

This work was supported by the Conselho Nacional de Desenvolvimento Científico e Tecnológico (CNPq). I'm grateful for this support, which made this research possible and allowed me to focus fully on it.

I'm very thankful to my advisor, Prof. Raphael Campos Drumond, for his helpful guidance, his patience when things were tough, and his consistent encouragement throughout this project. He was always there to help me think through problems.

I also thank my colleagues and collaborators for our good discussions and their everyday help. And to the department staff for being so professional and kind.

I'm grateful to my parents for their support and for reminding me to keep things in perspective. I thank my husband for his patience and encouragement, and for making room for this project even when our schedules were busy. I also appreciate my family and friends for understanding during intense periods, for checking in when it mattered, and for sharing the important moments along the way. Their support helped me get this work done.

Some scars are just dynamics refusing to forget.

—

Resumo

As *quantum many-body scars* (QMBS) surgiram como uma exceção à Hipótese de Termalização por Autovalores (*Eigenstate Thermalization Hypothesis* - ETH), oferecendo um mecanismo inesperado de quebra fraca da ergodicidade em sistemas não integráveis. Esta tese apresenta um estudo abrangente da estabilidade dos QMBS no modelo PXP, que descreve de forma efetiva a dinâmica de cadeias de átomos de Rydberg sujeitas a restrições cinéticas.

Investigamos sistematicamente o impacto de defeitos no estado inicial e de perturbações na Hamiltoniana sobre a dinâmica com scars. Modificações controladas no estado inicial, incluindo inversões de spin localizadas que preservam ou violam a restrição de bloqueio de Rydberg, revelam mecanismos distintos de decaimento da fidelidade e crescimento da entropia de emaranhamento. Notavelmente, defeitos que quebram a restrição podem induzir efeitos de congelamento local, aumentando a estabilidade das scars ao isolar cineticamente regiões da cadeia.

No que diz respeito à Hamiltoniana, exploramos os efeitos de correções fisicamente motivadas derivadas de uma expansão de Schrieffer-Wolff a partir do modelo microscópico de Rydberg, além de perturbações genéricas com e sem desordem. Simulações numéricas, realizadas por diagonalização exata e evolução temporal de cadeias finitas, mostram que as correções de Schrieffer-Wolff introduzem apenas pequenas deformações na dinâmica com scars, enquanto a presença de desordem — especialmente quando combinada com termos que quebram a restrição — exerce um papel dominante na supressão dos revivals.

Ao analisar observáveis como fidelidade, correlações locais, entropia de emaranhamento e sobreposição espectral, este trabalho caracteriza os efeitos das restrições cinéticas, da desordem e das perturbações microscópicas sobre a persistência da dinâmica com scars. Os resultados fornecem uma compreensão quantitativa de como diferentes mecanismos preservam ou degradam os revivals no modelo PXP. Este estudo contribui para o avanço da compreensão sobre dinâmicas não termais em sistemas quânticos restritos e oferece diretrizes para futuros esforços experimentais voltados à engenharia e estabilização desses estados.

Palavras-chave: quantum many-body scars; modelo PXP; dinâmica não termal; sistemas com restrições; átomos de Rydberg; termalização quântica.

Abstract

Quantum many-body scars (QMBS) have emerged as a striking exception to the Eigenstate Thermalization Hypothesis (ETH), offering an unexpected mechanism for weak ergodicity breaking in nonintegrable systems. This thesis presents a comprehensive study of the stability of QMBS in the paradigmatic PXP model, which effectively captures the dynamics of Rydberg atom chains under kinetic constraints.

We systematically investigate the impact of both initial state defects and Hamiltonian perturbations on scarred dynamics. Controlled modifications to the initial state, including localized spin flips that either preserve or violate the Rydberg blockade, reveal distinct mechanisms of fidelity decay and entanglement growth. Notably, defects that break the blockade constraint can induce local freezing effects, paradoxically enhancing scar stability by kinetically isolating regions of the chain.

Regarding the Hamiltonian, we explore the effects of physically motivated corrections derived from a Schrieffer-Wolff expansion of the microscopic Rydberg Hamiltonian, as well as generic perturbations with and without disorder. Numerical simulations, performed through exact diagonalization and time evolution of finite chains, reveal that Schrieffer-Wolff corrections introduce only minor deformations to the scarred dynamics, while the presence of disorder—especially when combined with constraint-breaking terms—plays a dominant role in suppressing revivals.

By analyzing observables such as fidelity, local correlations, entanglement entropy, and spectral overlap, this work characterizes the competing effects of kinetic constraints, disorder, and microscopic perturbations on the persistence of scarred dynamics. The results provide quantitative insights into how different mechanisms either preserve or degrade revivals in the PXP model. This study contributes to a deeper understanding of nonthermal behavior in constrained quantum systems and offers guidance for future experimental efforts aimed at engineering and stabilizing scarred states.

Keywords: quantum many-body scars; PXP model]; nonthermal dynamics, constrained systems; Rydberg atoms; quantum thermalization.

Sumário

1 Introduction

It is said that the flap of a butterfly's wings in Brazil can set off a tornado in Texas. This evocative image, the heart of the "butterfly effect," is more than just a poetic metaphor; it captures the essence of one of the most profound concepts in physics: chaos. In the world of classical mechanics, many systems, from the seemingly simple double pendulum to the complex dance of planetary orbits, exhibit this extreme sensitivity to initial conditions. A minuscule, almost immeasurable change at the start can lead to dramatically different outcomes down the line. For these chaotic systems, long-term prediction becomes not just difficult, but fundamentally impossible, forcing us to trade the certainty of single trajectories for the language of statistics and probability. This chaotic behavior is the very foundation of statistical mechanics, explaining how systems composed of countless particles eventually forget their origins and settle into a state of thermal equilibrium [1–3].

While our understanding of chaos in classical systems is now well established, extending these ideas into the quantum domain is far from straightforward. Unlike their classical counterparts, quantum systems evolve in a high-dimensional Hilbert space rather than in phase space, and their observables are governed by probabilistic amplitudes instead of deterministic trajectories. This shift in perspective invites a deeper question: if chaos relies on the exponential sensitivity of trajectories, how should we reinterpret this notion in a framework where such trajectories do not exist? Developing a consistent conceptual and mathematical framework for "quantum chaos" became one of the central motivations in bridging the classical and quantum descriptions of dynamical complexity.

However, the transition from the classical to the quantum description of a system presents an even more fundamental obstacle. The Schrödinger equation, the foundational equation governing quantum dynamics, is strictly linear. This linearity seems to preclude the exponential divergence of trajectories that defines classical chaos, suggesting that quantum systems should preserve the memory of their initial state indefinitely [4]. This raises a monumental question: How do the concepts of chaos and thermalization, so crucial for describing our world, emerge from a quantum framework that appears to forbid them?

The characterization of chaos in quantum systems, therefore, required a different approach. Instead of looking for chaotic trajectories, which do not exist in the quantum world, the focus shifted to the statistical properties of the system, such as the distribution of its energy levels, which serve as "fingerprints" of chaos. For systems whose classical counterparts were chaotic, these quantum fingerprints appeared consistently, leading to the establishment of "quantum chaos" as a field [5, 6]. The prevailing consequence of this

quantum chaos was believed to be universal: isolated, complex quantum systems should act as their own heat baths, a process described by the Eigenstate Thermalization Hypothesis (ETH). According to the ETH, if you wait long enough, any subsystem should become indistinguishable from a thermal state, effectively forgetting any special information about how it started [7, 8].

For decades, this principle stood as a central pillar in our understanding of quantum statistical mechanics. The picture seemed complete: complex quantum systems, left to their own devices, would inevitably thermalize. However, nature, as it often does, had a surprise in store. In a landmark 2017 experiment, a team of physicists prepared a quantum simulator of 51 Rydberg atoms in a simple, ordered initial state. According to the ETH, this highly excited state should have rapidly relaxed into a featureless thermal equilibrium. Instead, the researchers observed something astonishing: the system resisted thermalization. It displayed persistent, coherent oscillations, periodically returning to its initial configuration, thereby retaining a "memory" of its origin for an unexpectedly long time [9].

This unexpected behavior, a clear violation of the standard thermalization paradigm, was attributed to the presence of a small set of special, non-thermal eigenstates hiding within an otherwise chaotic spectrum. These states were named quantum many-body scars (QMBS). They are like islands of regularity in a sea of thermal chaos, exceptional states that weakly break the system's ergodicity and defy the predictions of the ETH [10–12]. Their discovery opened a new frontier, challenging our understanding of the very foundations of quantum statistical mechanics.

The existence of these remarkable states immediately raises a critical question, which forms the central motivation for this thesis: How robust are quantum many-body scars? Are they a delicate phenomenon, destroyed by the slightest imperfection, or do they possess a degree of resilience that could make them useful? To answer this, this work undertakes a systematic investigation into the stability of QMBS in the paradigmatic PXP model, the very model that effectively describes the dynamics of the Rydberg atom experiment. We introduce a variety of controlled perturbations designed to mimic both realistic experimental imperfections and theoretical deformations, including local defects in the initial state, corrections to the Hamiltonian, and the introduction of disorder. By analyzing a suite of dynamical and spectral observables, we map out the stability of these scars, revealing a surprisingly complex interplay between kinetic constraints, disorder, and the microscopic nature of the perturbations themselves. Ultimately, this exploration aims to shed light on the fundamental mechanisms that allow quantum systems to evade thermalization, a crucial step toward understanding and eventually controlling complex quantum dynamics.

In this thesis, we address these questions through a systematic investigation of the

stability of quantum many-body scars in the PXP model, an effective spin-$\frac{1}{2}$ Hamiltonian that captures the dynamics of Rydberg atom chains under the so-called blockade constraint, where adjacent excitations are energetically forbidden. This model provides a minimal yet remarkably rich platform for studying nonthermal quantum dynamics in constrained systems. By combining analytical considerations with exact numerical simulations, we explore how controlled perturbations — such as defects in the initial state, Schrieffer–Wolff corrections to the effective Hamiltonian, and various forms of disorder — influence the persistence of nonthermal dynamics. We analyze observables including fidelity, local correlations, entanglement entropy, and spectral overlap to quantify the robustness of scarred revivals and to identify the mechanisms that either preserve or degrade them. This approach bridges conceptual understanding and numerical evidence, providing a comprehensive view of scar stability in constrained quantum systems.

The remainder of this thesis is organized as follows. Chapter 2 presents the theoretical background, introducing the concepts of classical and quantum chaos, the Eigenstate Thermalization Hypothesis, and the emergence of quantum many-body scars in the PXP model. Chapter 3 classifies and motivates the perturbations considered in this work, ranging from initial state defects to Hamiltonian deformations. Chapter 4 reports the numerical results, detailing how each perturbation affects scar stability and discussing their comparative influence. Finally, Chapter 5 summarizes the main conclusions and outlines perspectives for future research on nonthermal dynamics and constrained quantum systems.

2 Background

2.1 Classical chaos and ergodicity

In classical mechanics, chaos emerges in systems with a high degree of nonlinearity, where small perturbations in initial conditions can lead to drastically different outcomes over time. This sensitivity is not a failure of determinism, but rather a consequence of the equations of motion amplifying such deviations. A well-known example is the double pendulum: despite being governed by deterministic laws, its trajectories vary wildly under minimal changes in initial angles — a phenomenon often referred to as the "butterfly effect".

In non-chaotic systems, the distance $\Delta(t)$ between a reference trajectory and a perturbed one remains bounded or increases algebraically. In contrast, chaotic systems display *exponential divergence*:

$$\Delta(t) \approx \Delta(0)\, e^{\gamma t},$$

where γ is a local expansion rate. This behavior is quantified by the *Lyapunov exponent*, which measures the average rate at which nearby trajectories separate. The *maximum Lyapunov exponent* λ is defined as:

$$\lambda = \lim_{t\to\infty} \lim_{\Delta(0)\to 0} \frac{1}{t} \ln \frac{\Delta(t)}{\Delta(0)}.$$

A positive Lyapunov exponent indicates exponential sensitivity to initial conditions, and thus characterizes a system as chaotic [1].

Another essential concept in this context is *ergodicity*, foundational to statistical mechanics. A classical system is said to be ergodic if, over long times, its trajectory densely explores all states allowed by conservation laws (e.g., energy), and does so with equal weight. In this case, time averages of observables converge to ensemble averages. This is the essence of the *ergodic hypothesis* proposed by Boltzmann, which allows the replacement of detailed trajectory-based descriptions by statistical ensembles [2, 3].

Chaotic dynamics typically ensure ergodic behavior, as the system effectively samples the full phase space in a pseudo-random way. As a result, chaotic classical systems tend toward *thermal equilibrium*, with macroscopic observables exhibiting statistical regularity despite the microscopic determinism.

While the concept of chaos is well established in classical dynamics, its extension to quantum systems is less straightforward. The linearity of the Schrödinger equation seems to preclude exponential sensitivity to initial conditions [4], and the absence of phase

space trajectories challenges the direct application of classical chaos indicators. However, the *correspondence principle* demands that quantum mechanics smoothly recover classical behavior in the appropriate limit - motivating the development of quantum analogs of classical chaos. These ideas will be explored in the next section.

2.2 Quantum chaos and scars

The definition of quantum chaos is not unique until today, but at a first approach, a quantum system is considered chaotic if it has a classical chaotic counterpart [13]. However, it is not always clear whether a quantum system even has a classical analog and, therefore, an independent characterization of quantum chaos would be desirable.

In 1977, Berry and Tabor [5] proposed a theoretical argument claiming that the energy spectrum of a quantized classically integrable Hamiltonian system consists of a sequence of uncorrelated numbers, i.e., the energy levels of the system are not influenced by one another and their distribution is random. Additionally, fluctuations in the energy spectrum of such a system are said to obey Poissonian statistics [14], which implies that the probability of finding two energy levels at a certain distance from each other is proportional to the exponential of the average number of energy levels in that range. Their proposition is now known as the Berry-Tabor conjecture.

On the other side, Bohigas *et al.* [15] conjectured that the statistical properties of highly ergodic systems were described by random matrix ensembles (BGS conjecture), which was supported by both numerical and theoretical evidence [16–19]. In such systems, the energy levels exhibit strong correlations, resulting in level repulsion, and their statistics are very well approximated by the Wigner-Dyson distribution [20].

In this sense, chaos in quantum systems is often identified through analyzing energy level statistics. Initially, this approach was primarily applied to systems with a clear classical counterpart, where classical chaotic behavior provided a basis for comparison. Over time, however, analyzing energy level statistics has become a more general method for identifying chaos in a wide variety of quantum systems.

The eigenstates are also expected to have a specific structure in chaotic systems. Indeed, due to the correspondence principle, if a classical system is ergodic, the highly excited eigenstates of the quantized Hamiltonian should be thermalized. That is, a measurement of any observable should match the expectation value of the microcanonical ensemble. However, observations have shown that certain chaotic dynamical systems may have some special states that do not exhibit thermalization, but rather maintain a probability density concentrated near a periodic trajectory. This suggests that the link between chaos and thermalization may not be as straightforward as previously thought. Those exceptional states are considered to be an instance of weak ergodicity breaking, and were named

quantum scars.

Despite these advances, certain quantum systems exhibited deviations from these expectations. A particularly striking example was presented by Heller, also in 1984 [21]. Studying the stadium billiard — a two-dimensional system whose classical dynamics is chaotic — Heller found that some quantum eigenstates showed enhanced probability density along the paths of unstable periodic orbits. This was in contrast to the Berry conjecture and became known as the phenomenon of *quantum scarring.*

Quantum scars, in this original sense, are visualized in Fig. Figura 1, where the wavefunction intensity in the stadium billiard is concentrated along a classical unstable orbit. The figure also includes the classical trajectory and its Poincaré section, revealing the contrast between the irregularity of classical motion and the localized features of the quantum state. The emergence of such scars suggests that classical instabilities do not completely erase dynamical memory at the quantum level [22].

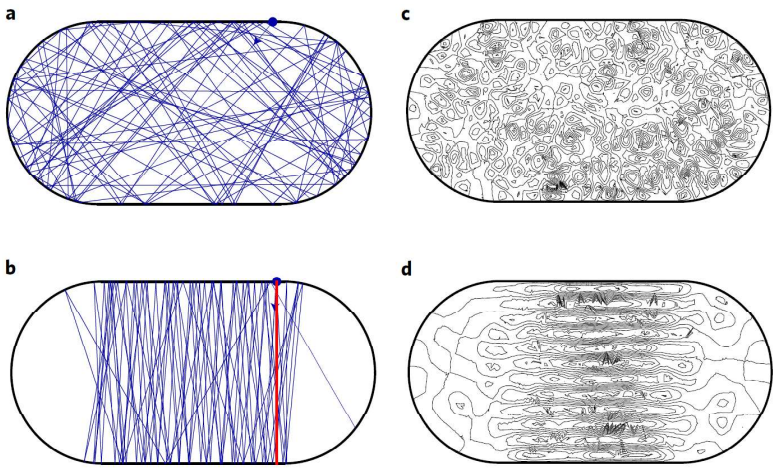

Figura 1 – (a) A classical particle initialized away from a periodic trajectory displays chaotic motion. (b) In contrast, when launched near a "bouncing-ball" trajectory (shown in red), the particle spends a long time in its vicinity before escaping. (c) The probability density of a typical highly excited eigenstate of the billiard resembles a collection of random plane waves. (d) The probability density of a quantum-scarred eigenstate looks very different from a collection of plane waves, instead being strongly concentrated near the periodic trajectory. Figure adapted from [22].

The special eigenstates can be detected by comparing the wave function probability density (Figura 1 c and Figura 1 d) with the classical orbit (Figura 1a and Figura 1b). Wave packets "launched" in the vicinity of a periodic orbit will tend to cluster around the orbit, exhibiting a higher return probability than wave packets launched elsewhere in phase space. They can also be expanded over a small number of eigenstates with approximately similar energy spacing, unlike a generic wave packet [21, 22]. Numerical investigations have demonstrated this phenomenon for both the bouncing ball trajectories and more complex unstable periodic trajectories [23].

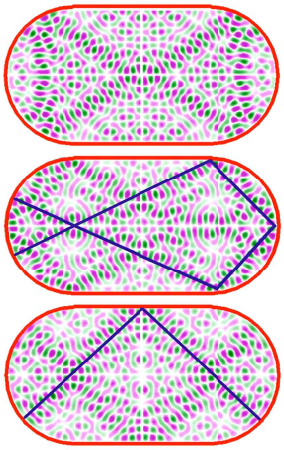

Figura 2 – Typical scarred eigenstates of the Bunimovich stadium. The panels show the probability density for three different eigenstates. Bright regions of concentrated probability correspond to quantum scars generated by unstable periodic orbits, two of which are illustrated. Adapted from Wikimedia Commons, original image available at `https://commons.wikimedia.org/wiki/File:Stadium_scar.png`, licensed under CC BY 4.0 International (`https://creativecommons.org/licenses/by/4.0/`).

The emergence of quantum scars can be visualized more directly by examining the spatial structure of individual eigenstates of the stadium billiard. While Figure 1 illustrates how a single wavefunction can display enhanced probability density along a classical periodic trajectory, the corresponding state represents one particular example of this phenomenon. A broader view is shown in Figure 2, which presents distinct eigenstates of the Bunimovich stadium. Each of these wavefunctions exhibits regions of concentrated probability density, referred to as scars.

More recently, however, a different class of quantum scars has been discovered — one that appears in *many-body systems* with interactions and constraints. These *quantum many-body scars* are fundamentally distinct from the single-particle scars described by Heller. They manifest as *nonthermal eigenstates* embedded within otherwise thermal spectra, and give rise to anomalous dynamics, such as periodic revivals and reduced entanglement growth [10, 11, 24]. These scars are not a consequence of classical periodic orbits. Instead, quantum many-body scars are nonthermal eigenstates embedded in an otherwise thermal spectrum, and various mechanisms have been proposed to explain their emergence. Including constrained dynamics, emergent dynamical symmetries, the existence of approximately closed subspaces, and forward scattering constructions — all of which can lead to atypical coherent dynamics starting from special initial states.

This thesis focuses on the study of quantum many-body scars, particularly in the context of the *PXP model*, which captures the dynamics of Rydberg atom chains under blockade constraints. In the following sections, we will explore the mechanisms behind these scars, their spectral structure, and their sensitivity to various perturbations.

2.3 Eigenstate Thermalization Hypothesis

The first significant steps toward understanding thermalization of quantum states were made by John von Neumann in the 1920s and 1930s [25]. Von Neumann introduced the Quantum Ergodic Theorem (QET) and provided a statistical foundation for the approach to equilibrium in quantum systems. According to the QET, for a typical finite family of commuting macroscopic observables, every initial wave function ψ_0 from a micro-canonical energy shell so evolves that for most times t in the long run, the joint probability distribution of these observables obtained from ψ_t is close to their micro-canonical distribution [26]. Indeed, considering a Hamiltonian $\hat{H}$, we can expand an initial state in the eigenstate basis as $|\psi(0)\rangle = \sum_\alpha C_\alpha |\Psi_\alpha\rangle$, where $C_\alpha = \langle\Psi_\alpha|\psi(0)\rangle$ and α runs over all the basis eigenstates ψ_α. Therefore, the time evolution is given by

$$|\psi(t)\rangle = e^{-i\hat{H}t}\,|\psi(0)\rangle = \sum_\alpha C_\alpha e^{-iE_\alpha t}\,|\Psi_\alpha\rangle\,, \tag{2.1}$$

where E_α are the eigenstate energies. For an observable $\hat{A}$, the quantum-mechanical mean evolves as,

$$\langle\hat{A}(t)\rangle = \langle\psi(t)|\,\hat{A}\,|\psi(t)\rangle = \sum_\alpha |C_\alpha|^2 A_{\alpha\alpha} + \sum_{\alpha,\beta} C^*_\alpha C_\beta e^{i(E_\alpha - E_\beta)t} A_{\alpha\beta}, \tag{2.2}$$

where the second sum runs for $\alpha \neq \beta$ and $A_{\alpha\beta} = \langle\Psi_\alpha|\,\hat{A}\,|\Psi_\beta\rangle$. The long-time average, without degeneracies, is then

$$\overline{\langle\hat{A}\rangle} = \lim_{\tau\to\infty}\int_0^\tau dt\langle\hat{A}(t)\rangle = \sum_\alpha |C_\alpha|^2 A_{\alpha\alpha}. \tag{2.3}$$

Von Neumann argued that, up to small corrections, the long-time average in Eq. 2.3 coincides with the microcanonical average over the same energy window, provided that the distribution $|C_\alpha|^2$ is sufficiently concentrated around a given energy E — a condition typically satisfied by physically relevant initial states [8, 27, 28]. This early result already suggests a form of thermalization rooted in typicality, and anticipates the more refined statement later formalized by the Eigenstate Thermalization Hypothesis (ETH).

Despite these advances, the specific mechanisms by which individual quantum states could exhibit thermal behavior remained elusive. However, in the early 1990s, two pivotal papers by Mark Srednicki [29] and, independently, by J. M. Deutsch [7] provided a breakthrough. They proposed what is now known as the Eigenstate Thermalization Hypothesis (ETH). According to ETH, for non-integrable systems, the expectation value of a generic observable in an eigenstate of the Hamiltonian is equal to the microcanonical ensemble average at the same energy. This hypothesis suggested that individual eigenstates themselves encode thermal properties, thus resolving the apparent paradox between unitary evolution and thermalization.

Interestingly, it was shown that the QET condition relies on a technical assumption that is essentially equivalent to the ETH proposed by Srednicki in 1994, who considered random matrix theory assumptions in his work. Conceptually, the hypothesis states that closed quantum systems thermalize at the level of individual eigenstates [4]. Mathematically, for an N-body system, the diagonal matrix elements (in the energy eigenbasis) of a few-body observable depend only on the energy E of an eigenstate, and should be given by the expected value of a thermodynamic ensemble at energy E. The off-diagonal matrix elements should decay exponentially with the energy difference of the eigenstates. Moreover, both diagonal and off-diagonal elements will present some fluctuations that are, however, exponentially small in N [28]. To sum up, for a local observable $\hat{O}$ we should have:

$$O_{mn} \equiv \langle m|\,\hat{O}\,|n\rangle = O(\overline{E})\delta_{mn} + e^{-S(\overline{E})/2} f_O(\overline{E},\omega) R_{mn}, \tag{2.4}$$

where $|m\rangle$ and $|n\rangle$ are the eigenstates with energies E_m and E_n, $\overline{E} = (E_m + E_n)/2$, $\omega = E_n - E_m$, $S(E)$ is the thermodynamic entropy at energy E, R_{mn} is a random number and, importantly, $O(\overline{E})$ and $f_O(\overline{E},\omega)$ are smooth functions of their arguments. The first term at the right-hand side of Eq. (2.4) describes the behavior of the microcanonical ensemble as a smooth function of energy, while the second term characterizes the fluctuations about the microcanonical prediction [30].

In other words, ETH provides a bridge between quantum mechanics and statistical mechanics by proposing that the properties of individual energy eigenstates are sufficient to describe thermalization [28]. However, there are two sides of the hypothesis: (i) the strong ETH [7], on which the expectation value of O for every eigenstate $|E\rangle$ is approximately the thermal expectation value of the same observable at the energy corresponding to $|n\rangle$:

$$\langle n|\,\hat{O}\,|n\rangle \approx \langle O(E_n)\rangle_{\text{thermal}}, \tag{2.5}$$

implying that every individual eigenstate is "thermal" in the sense that measuring any observable in such a state yields results consistent with thermal equilibrium. And (ii) the weak ETH, that instead of requiring every individual eigenstate to have expectation values matching thermal values, it suggests that thermal properties emerge from the statistical average over a small energy window or over an ensemble of eigenstates within that energy range. It allows for the possibility that some individual eigenstates may not appear thermal, but when considering many such states together, the system still behaves thermally [31].

The physical consequences of ETH become especially clear when considering the evolution of generic initial states. If the initial state $|\psi(0)\rangle = \sum_\alpha C_\alpha\,|\Psi_\alpha\rangle$ has energy components $|C_\alpha|^2$ concentrated within a narrow energy window, and if the diagonal matrix elements $A_{\alpha\alpha}$ vary smoothly with energy, then the long-time average of the observable becomes

$$\sum_\alpha |C_\alpha|^2 A_{\alpha\alpha} \approx \langle \hat{A}\rangle_{\text{micro}}. \tag{2.6}$$

This shows that, for most physically relevant initial conditions — i.e., states that have a well-defined energy (with small fluctuations), broad overlap with many nearby eigenstates, and no fine-tuned correlations designed to avoid thermalization — the expectation value of observables relaxes to thermal values at long times. Importantly, this happens despite the global evolution being unitary and the system remaining in a pure state. In this sense, ETH provides a microscopic foundation for thermalization: unitary dynamics alone is sufficient to reproduce the predictions of equilibrium statistical mechanics for local observables.

The properties of ergodic systems were then conjectured to be governed by the ETH [7, 29], which is considered a key feature for dynamical systems that reach thermal equilibrium [28]. This theoretical perspective gained strong support from numerical studies and experiments on isolated quantum systems, which confirmed the predictions of ETH in a variety of non-integrable models. Additionally, the Wigner-Dyson statistics observed in the distribution of energy level spacings is now recognized as a fundamental characteristic for classifying a quantum system as chaotic, even in the absence of a classical counterpart [32].

An important contribution to this field was made by Rigol, Dunjko, and Olshanii in 2008 [8]. Their study demonstrated that generic isolated quantum many-body systems relax to states well described by standard statistical-mechanical prescriptions, thereby providing robust empirical support for ETH.

In their work, the authors examined the relaxation dynamics of hard-core bosons on a lattice and showed that the system's long-time behavior matched the predictions of the microcanonical ensemble. They highlighted that thermalization in these systems occurs at the level of individual eigenstates, as proposed by ETH. This finding was significant because it confirmed that knowledge of a single many-body eigenstate within a specific energy window is sufficient to predict thermal averages.

Beyond bosonic systems, spin chains also provide robust platforms to test ETH. For example, the generic spin-$\frac{1}{2}$ Heisenberg chain with next-nearest neighbor interactions constitutes a paradigmatic non-integrable model. In this regime, the system exhibits chaotic dynamics, which leads to thermalization consistent with the predictions of ETH. After a quench, the system evolves towards a thermal state, where the long-time averages of local observables align with the values expected from statistical mechanics [32]

Despite its success in describing a wide class of chaotic systems, ETH is not universally valid. In particular, both its strong and weak forms fail to capture the dynamics of all types of systems. For example, it does not accurately predict the behavior of non-chaotic systems such as integrable models [33–35], characterized by an extensive number of conserved quantities, or many-body localized (MBL) systems [12, 36–38], where strong disorder leads to the localization of many-body states in Fock space. In these cases, transport is inhibited, memory of the initial conditions is preserved over long times, and thermalization fails. Local observables thus do not relax to thermal values, signaling a

breakdown of the ETH. This failure is reflected in the transition of energy level statistics from the Wigner–Dyson to the Poisson distribution [5, 10, 39]. Such violations exemplify strong ergodicity breaking, where all eigenstates remain non-thermal [30].

Figure 3 illustrates the contrasting energy level spacing statistics of integrable and chaotic quantum systems. Integrable or localized systems follow Poisson statistics, indicating the absence of correlations between neighboring levels. In contrast, chaotic systems obey the Wigner–Dyson distribution predicted by random matrix theory, which captures the phenomenon of level repulsion—an essential fingerprint of quantum chaos.

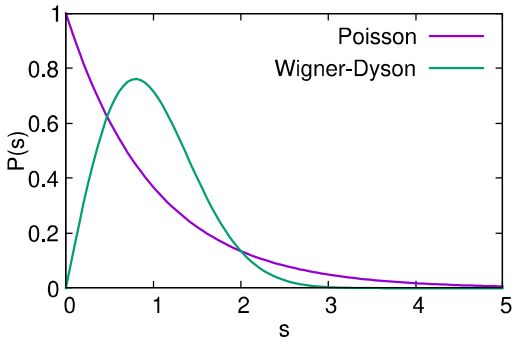

Figura 3 – Energy level spacing statistics for integrable and chaotic quantum systems. The Poisson distribution (purple) characterizes uncorrelated energy levels typical of integrable or localized systems, where adjacent levels can cluster freely. The Wigner–Dyson distribution (green) exhibits level repulsion and describes the correlated spectra of chaotic systems, serving as a hallmark of quantum chaos.

Interestingly, not all violations of ETH result in a complete absence of thermalization. In between fully ergodic and integrable regimes, systems can exhibit what is known as weak ETH violation. In these cases, while the majority of the system's eigenstates comply with ETH and thermalize as expected, there exists a special subset of states that do not follow this rule. These exceptional eigenstates retain non-thermal characteristics, leading to a failure of thermalization despite the chaotic nature of the surrounding spectrum. These non-thermal states, which evade the typical ergodic behavior and persist in a coherent, low-entropy configuration, were then naturally called many-body scars.

Together with many-body localization, the discovery of quantum many-body scars challenges our understanding of ergodicity in quantum systems. While MBL arises from strong disorder and localization mechanisms, the phenomenon of many-body scarring occurs in clean, constrained systems and reveals a new path for weak ergodicity breaking — the focus of the next section.

2.4 Quantum many-body scars

The ETH provides a robust framework for understanding the thermalization of isolated quantum many-body systems. However, recent discoveries have shown that not

all systems adhere strictly to this paradigm. A notable exception arises in the form of *quantum many-body scars* (QMBS), a phenomenon that represents a weak violation of ETH. These states form a small subset of eigenstates that evade typical thermalization dynamics, persisting in low-entropy, coherent configurations despite the chaotic nature of the surrounding spectrum.

The first experimental indication of QMBS emerged from a study of a 51-atom quantum simulator using an array of trapped neutral cold atoms coupled to highly excited Rydberg states [9]. The system was initialized in a period-two charge density wave (CDW) configuration, the Néel state $|\mathbb{Z}_2\rangle$, and evolved under unitary dynamics. Surprisingly, instead of displaying rapid thermalization, this state exhibited persistent, coherent oscillations in local observables far beyond the expected thermalization timescale [11]. This behavior defied conventional expectations from ETH, suggesting that some eigenstates of the system were special, forming what are now called QMBS.

From a theoretical perspective, these nonthermal states were later explained in the framework of constrained models, particularly the PXP model, which effectively describes the Rydberg blockade mechanism. The PXP Hamiltonian constrains the Hilbert space by preventing adjacent excitations, leading to a nontrivial quantum dynamics where QMBS can emerge [10, 40]. The identification of a special set of eigenstates with anomalously low entanglement and approximately regular energy spacing led to the proposal of spectrum-generating algebras as an underlying structure [41, 42].

A defining feature of QMBS is their entanglement entropy scaling. In generic thermalizing systems, entanglement entropy follows a volume law, growing proportionally with subsystem size. However, QMBS states deviate from this pattern, displaying subextensive entanglement entropy scaling, which is closer to an area law or logarithmic growth [22]. This characteristic differentiates QMBS from both thermal eigenstates and fully localized states, positioning them as a new class of weakly ergodic-breaking states.

However, this distinction is not absolute. Rainbow scars [43], for instance, challenge this conventional behavior by exhibiting extensive bipartite entanglement entropy. If the system is randomly partitioned, the entropy scales with the size of the cut, resembling thermal behavior. Yet for specific bipartitions aligned with their underlying mirror symmetry, these states maintain subextensive entanglement scaling, highlighting their hybrid nature.

The reason rainbow scars exhibit this dual entanglement behavior for random bipartitions and subextensive for specific ones comes from the unique structure of these states and their underlying symmetries. Rainbow scars are constructed in such a way that they encode a particular pattern of entanglement across the system, where each site is strongly correlated with a corresponding "mirror" site on the opposite end of the system. This mirroring creates a highly organized and symmetric entanglement structure. For

generic bipartitions, this structured entanglement manifests as extensive entropy because the partition likely disrupts these mirror pairs, leading to a large number of entangled links being cut, similar to what happens in a thermal state. However, when the system is partitioned in a way that respects the mirror symmetry, for example, being cut exactly between these paired sites, the entanglement entropy does not grow as quickly, resulting in subextensive scaling.

In some models, QMBS have been linked to a broader phenomenon called Hilbert space fragmentation, in which the Hilbert space breaks into dynamically disconnected subspaces, preventing full thermalization [44]. The AKLT model [22,41,44–49], for example, hosts exact QMBS due to emergent algebraic constraints, reinforcing the idea that symmetry and dynamical constraints play a key role in sustaining nonthermal states.

A different perspective on QMBS also comes from quantum circuit models, where certain initial states lead to nonthermal dynamics despite chaotic unitary evolution. This has drawn connections between QMBS and dynamical symmetries in quantum many-body evolution [50].

One of the most well-understood mechanisms leading to QMBS is the existence of scar towers, a structure where a sequence of equally spaced eigenstates appears within the many-body spectrum [42,50–52]. The mathematical foundation for this behavior is based on spectrum-generating algebras, where a set of ladder operators creates an energy hierarchy of special eigenstates separated by a fixed spacing [44, 52]. These algebraic structures provide a deeper understanding of QMBS and have led to proposals for constructing parent Hamiltonians that stabilize these nonthermal states in a controlled manner [53, 54].

The dynamical signature of a scarred tower can be captured by the fidelity, defined as the return probability to the initial state: $\mathcal{F}(t) = |\langle\psi(0)|\psi(t)\rangle|^2$. Consider an initial state that overlaps predominantly with a set of scarred eigenstates $\{|E_n\rangle\}$ forming a tower with uniform energy spacing ε, i.e., $E_n = E_0 + n\varepsilon$. Then, the time evolution of such a state can be written as $|\psi(0)\rangle = \sum_n c_n |E_n\rangle$, and the fidelity becomes

$$\mathcal{F}(t) = \sum_{n,m} |c_n c_m|^2 e^{i(E_m - E_n)t}. \tag{2.7}$$

Since the energy differences $E_m - E_n$ are integer multiples of ε, all phases rephase periodically, leading to perfect revivals at times $T = \frac{2\pi}{\varepsilon}$. In this way, the periodic structure of the tower manifests dynamically through recurrent peaks in the fidelity.

While the existence of an equally spaced tower of nonthermal eigenstates is essential, the emergence of coherent revivals relies on the spectral composition of the initial state. Specifically, it is the concentration of its weight on the scarred eigenstates that enables the appearance of revivals. In many cases, simple product states naturally satisfy this condition, coupling selectively to the tower due to their structure and symmetry.

The first analytical example of such a tower of eigenstates was found in the spin-1 AKLT model [50, 51] and later in spin-1 XY [52], as well as in models exhibiting η-pairing, originally studied in the context of the Hubbard model [42].

The discovery of QMBS has far-reaching implications across quantum physics. Their ability to sustain long-lived coherence suggests applications in a range of fields, from condensed matter physics to quantum information science [55–60]. In particular, the controlled preparation of QMBS could lead to error-resilient quantum information protocols, leveraging their slow entanglement growth and robust coherence properties.

Another key open question is the stability of QMBS under perturbations. While weak integrability-breaking terms can destabilize scars, recent studies suggest that specific perturbations may actually enhance or even generate new QMBS [61]. Understanding the precise conditions under which QMBS persist remains a crucial challenge.

Several works have explored this question in detail. Generic perturbations tend to hybridize scarred eigenstates with the thermal bulk, suppressing revivals and destroying coherence [24, 62]. However, there exist classes of carefully engineered perturbations — including quasi-local corrections [53, 61], kinetic constraints [44], and Schrieffer–Wolff-type expansions— that can stabilize or even induce scarred dynamics. Identifying and characterizing such perturbations remains central to understanding the robustness and practical relevance of QMBS.

In this work, we focus on the first model on which the existence of quantum many-body scars was detected [9]: the spin-1/2 model with nearest-neighbor interactions in the Rydberg-atom chain limit — also known as the *Rydberg blockade model* or *PXP Hamiltonian* [10, 40, 63].

2.5 The PXP model

The Rydberg model, which describes systems of highly excited Rydberg atoms, has garnered significant attention in the field of quantum physics due to its unique properties and wide range of applications [9, 64–66]. Rydberg atoms are atoms in which one or more electrons are in a highly excited state, characterized by a large principal quantum number. These atoms possess exaggerated properties, such as an unusually large size, a long lifetime, and are extremely sensitive to electric fields [66–68]. In particular, they exhibit strong dipole-dipole interaction with each other and can be laser cooled to form a frozen Rydberg gas, in which the effect of thermal motion can be considered negligible over the timescale of interactions [65].

To understand the effective description of a Rydberg atom chain, let us consider a pair of atoms with ground and excited Rydberg states denoted by $|g\rangle$ and $|r\rangle$, respectively.

When two atoms are simultaneously excited to the Rydberg state $|rr\rangle$, they experience strong interactions due to their large polarizability. In the absence of resonant dipole coupling, the dominant interaction is of van der Waals type, which induces an energy shift that scales as $1/R^6$ with the interatomic distance R.

Each atom can thus be mapped to a two-level system, identifying $|\circ\rangle \equiv |g\rangle$ and $|\bullet\rangle \equiv |r\rangle$, forming an effective spin-1/2 representation, where $|\circ\rangle$ corresponds to spin-down and $|\bullet\rangle$ to spin-up. Under coherent laser driving with Rabi frequency Ω and detuning δ, the full Hamiltonian for an ensemble of atoms is given by [11, 65, 69]:

$$H = \sum_{i}^{N} \left(\frac{\Omega}{2} X_i - \delta Q_j \right) + \sum_{j<i}^{N} V_{i,j} Q_i Q_j \tag{2.8}$$

where Q_i is a diagonal operator $Q_i = (\mathbb{1} + Z_i)/2$ corresponding to the density of excitations on a given site, with $Z_i = (|\bullet\rangle \langle\bullet| - |\circ\rangle \langle\circ|)$ being the Pauli Z matrix acting on site i. Ω is the Rabi frequency (required frequency to cause the transition between energy levels), δ is the detuning parameter (how far the light is off-resonance relative to the transition), and $V_{i,j} \propto 1/|j-i|^6$ is the van der Waals interaction between atoms. We thus model the system as a chain of L spin-1/2 sites, each representing the state of a single atom. The Pauli operator X_i flips the spin at site i between $|\downarrow\rangle$ and $|\uparrow\rangle$ (i.e., $|\circ\rangle$ and $|\bullet\rangle$), representing the Rabi coupling.

Let us introduce a projector P_i onto the ground state at site i:

$$P_i \equiv |\circ_i\rangle \langle\circ_i| = \frac{\mathbb{1} - Z_i}{2}. \tag{2.9}$$

In contrast to Q_i, the projector corresponds to the density of atoms in the ground state, and it will be convenient to the next steps.

As discussed previously, we focus on the regime where the van der Waals interaction between nearest-neighbor atoms dominates over both the laser driving and interactions at longer distances. In this case, we approximate $V \approx V_{i,i+1} \gg \Omega$, and we consider the resonant condition $\delta = 0$ for simplicity. This regime defines the so-called Rydberg blockade: when the interaction energy V exceeds the Rabi frequency Ω, the simultaneous excitation of two neighboring atoms becomes energetically unfavorable, effectively suppressing the population of configurations where adjacent sites are both in the Rydberg state.

Rescaling the Hamiltonian by $1/V$ and introducing the parameter $\epsilon = \Omega/(2V)$, we have:

$$H = H_0 + \epsilon H_1 = \sum_i Q_i Q_{i+1} + \epsilon \sum_i X_i. \tag{2.10}$$

The first and dominant term H_0 counts the number of adjacent excitations and has highly degenerate eigenvalues. The perturbative term H_1 is the trivial paramagnet.

An effective Hamiltonian can be obtained through the use of the Schrieffer-Wolff (SW) method, a version of degenerate perturbation theory. This method is applicable when the interactions between the atoms are strong, characterized by small ϵ values. The SW method works by applying a unitary transformation to the exact Hamiltonian, effectively decoupling the low-energy and high-energy subspaces, resulting in a H_{eff} that describes the low-energy dynamics of the system [70]. In this sense, the projector into the subspace spanned by a configuration without adjacent spin-up states can be written as

$$\mathcal{P} = \prod_i (\mathbb{1} - Q_i Q_{i+1}). \tag{2.11}$$

In Rydberg atom chains under strong blockade conditions, configurations in which two neighboring atoms are simultaneously in the spin-up state are energetically penalized. These high-energy states, associated with adjacent excitations, define the sector that will be projected out in the effective low-energy description. Within this restricted subspace, the first term of the Hamiltonian vanishes, and the leading-order non-trivial contribution arises from the projected perturbation $H_{\text{SW}} = \epsilon\, \mathcal{P} H_1 \mathcal{P}$. Removing the overall scale ϵ, the effective PXP model is obtained:

$$H = \sum_{i=1}^{N} P_{i-1} X_i P_{i+1}. \tag{2.12}$$

This model preserves the subspace where first neighbors are not simultaneously in the spin-up state, e.g., for the term $P_1 X_2 P_3$ acting on $|\circ\circ\circ\rangle$ gives $|\circ\bullet\circ\rangle$ (and vice versa). Therefore, initial states in that subspace will remain in it.

2.5.1 Time evolution and spectral analysis

The time evolution of the system is governed by the Schrödinger equation,

$$i\frac{d}{dt}|\psi(t)\rangle = H|\psi(t)\rangle \tag{2.13}$$

with a formal solution, for a time-independent Hamiltonian,

$$|\psi(t)\rangle = e^{-iHt}\,|\psi(0)\rangle\,. \tag{2.14}$$

Expressing the dynamics in the energy eigenbasis provides direct insight into the mechanisms underlying coherence and thermalization. Given the spectral decomposition

$$H\,|E_n\rangle = E_n\,|E_n\rangle\,, \tag{2.15}$$

the time-evolved state can be written as

$$|\psi(t)\rangle = \sum_n e^{-iE_n t}\langle E_n|\psi(0)\rangle|E_n\rangle. \tag{2.16}$$

The evolution is therefore a coherent superposition of eigenstates oscillating with phases determined by their energies. The long-time behavior is controlled by the interference pattern between these phases. When the initial state has significant overlap with a large number of eigenstates whose energy differences are incommensurate or effectively random — as expected in thermalizing systems — the phases rapidly lose coherence. This destructive interference leads to dephasing, a suppression of coherent oscillations, and convergence to thermal-like expectation values, in accordance with ETH.

In contrast, the presence of quantum many-body scars is associated with an anomalous structure in the spectrum. If the initial state has substantial weight on a set of eigenstates organized into a ladder with approximately equal energy spacings — the so-called scar tower — the corresponding phase factors evolve in a correlated way. Instead of dispersing, the phases periodically realign, producing constructive interference at specific times. This results in robust revivals in fidelity and suppressed entanglement growth, distinguishing scarred dynamics from both ergodic and fully localized behavior.

The key mechanism behind scars is therefore the existence of a dynamically relevant subspace embedded within an otherwise thermalizing spectrum. The spectral structure of this subspace — characterized by approximately uniform energy spacings — supports long-lived coherent dynamics that violate the typical predictions of ETH.

2.5.2 Observables

The dynamical behavior of the system is characterized by a set of observables that provide complementary insights into coherence, spatial correlations, entanglement growth, and spectral structure. During time evolution, the wavefunction $|\psi(t)\rangle$ is saved at each time step, and time-dependent observables are computed via post-processing based on these stored states. In contrast, the spectral decomposition is performed within the constrained Hilbert space (when applicable) and is used to compute quantities that directly depend on the eigenstate structure, such as the spectral overlap.

The combination of these observables offers a comprehensive framework for diagnosing scarred dynamics, contrasting it with both ergodic thermalizing behavior and dynamics under various perturbations.

Fidelity

The fidelity is defined as

$$F(t) = |\langle\psi(0)|\psi(t)\rangle|^2 \tag{2.17}$$

and quantifies the return probability to the initial state at time t. In thermalizing systems, the fidelity typically decays rapidly due to dephasing arising from the incoherent interference

of eigenstate phases. In contrast, the presence of quantum many-body scars is signaled by robust, long-lived revivals in fidelity, reflecting the periodic rephasing associated with the scar tower structure in the spectrum.

Average nearest-neighbor correlation

The average nearest-neighbor correlation is defined as

$$C(t) = \frac{1}{L-1} \sum_{i=1}^{L-1} \langle Z_i(t) Z_{i+1}(t) \rangle. \tag{2.18}$$

This observable captures the time evolution of local correlations in the Z-basis. In thermalizing systems, $C(t)$ rapidly relaxes to a steady value, reflecting the loss of spatial order and the equilibration of the system. In contrast, the presence of quantum many-body scars is associated with persistent oscillations in $C(t)$, mirroring the revivals observed in the fidelity. These oscillations indicate that the system retains memory of the spatial ordering present in the initial state, resisting the homogenization characteristic of thermal dynamics.

The use of both fidelity and nearest-neighbor correlation as primary diagnostics of scarred dynamics is well established in the literature [10,11,22]. Together, these observables capture complementary aspects of coherence and spatial structure during the system's evolution.

Bipartite entanglement entropy

The bipartite entanglement entropy is calculated by partitioning the chain into two subsystems and evaluating the von Neumann entropy of the reduced density matrix of one part. Although equal bipartitions are commonly used, considering subsystems of varying size is useful for identifying different scaling behaviors, such as volume-law and area-law entanglement. The entropy is given by

$$S(t) = -\mathrm{Tr}_A \left(\rho_A(t) \log \rho_A(t) \right), \tag{2.19}$$

where $\rho_A(t) = \mathrm{Tr}_B \left| \psi(t) \right\rangle \left\langle \psi(t) \right|$ is obtained by tracing out one half of the system.

In thermalizing systems, the entanglement entropy typically grows rapidly until it saturates at the so-called *Page value*, which corresponds to the average entanglement entropy of a random pure state in the Hilbert space. This saturation reflects the maximum entropy expected in thermalized systems up to finite-size corrections. The Page value for a bipartition at the center of a spin-$\frac{1}{2}$ chain of length L scales approximately as

$$S_{\mathrm{Page}} \approx \frac{L}{2} \log 2 - \frac{1}{2}. \tag{2.20}$$

The scaling behavior of the entanglement entropy is a key diagnostic of ergodicity. In ergodic systems, entanglement of eigenstates follows a *volume law*, growing proportionally

to the size of the subsystem. In contrast, scarred dynamics exhibit suppressed entanglement growth, often saturating at values consistent with an *area law* or logarithmic growth, reflecting the effective confinement of the dynamics to a low-entanglement subspace embedded within the full Hilbert space.

Spectral overlap

The spectral overlap quantifies how the initial state decomposes in the eigenbasis of the Hamiltonian,

$$P_n = |\langle E_n|\psi(0)\rangle|^2. \tag{2.21}$$

As discussed in the previous section, the time evolution of the wavefunction can be expressed as a coherent superposition of eigenstates oscillating with phase factors determined by their energies. The spectral overlap distribution directly measures the contribution of each eigenstate to the initial state.

In thermalizing systems, P_n is broadly distributed over a large number of eigenstates, reflecting the absence of coherent structure in the dynamics. In contrast, scarred dynamics are characterized by a highly non-uniform P_n, with significant weight concentrated on a small set of nonthermal eigenstates forming the scar tower. This spectral fingerprint provides direct insight into the mechanism responsible for coherent revivals and reduced entanglement growth.

2.5.3 Revivals and special states

Using the PXP is very appealing to this research, since experiments [9] and numerical simulations on small systems [71, 72] have shown that the relaxation of the system under unitary dynamics strongly depends on the initial state. Further, the period-2 CDW states

$$|\mathbb{Z}_2\rangle = |\bullet \circ \bullet \circ ...\rangle\,, \qquad |\mathbb{Z}_2^{'}\rangle = |\circ \bullet \circ \bullet ...\rangle \tag{2.22}$$

revealed long-time oscillations of local observables, such as the correlation between atoms and slower entanglement entropy growth compared to other initial states. Similarly, although to a lesser extent, states such as $|\mathbb{Z}_3\rangle = |\bullet \circ \circ \bullet \circ \circ ...\rangle$ displayed slower entanglement entropy growth as well [9, 10], as shown in the Figura 4.

Also, the fidelity of initial states such as $\mathbb{Z}_2$ does not yield a perfect return to their initial states, as shown in Figura 5. These imperfect revivals are due to the fact that PXP scars are only approximately equally spaced in energy, which means they do not form a proper energy tower.

However, the observed partial revivals can be attributed to the substantial overlap between these states and the quantum scars within the system's Hamiltonian [10]. As

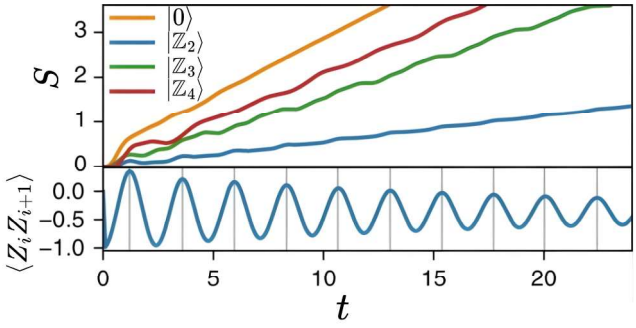

Figura 4 – Logarithm of the squared overlap $|\langle \mathbb{Z}_2|\psi_i\rangle|^2$ between the $|\mathbb{Z}_2\rangle$ initial state and the many-body eigenstates $|\psi_i\rangle$ of the PXP Hamiltonian, obtained by exact diagonalization [10]. The horizontal axis shows the eigenstate energy E_i, and the vertical axis quantifies the overlap amplitude. Colors represent the density of eigenstates in this plane: bright regions indicate energy ranges where many states have similar small overlaps, while darker regions correspond to sparser distributions. A small group of eigenstates near the center of the spectrum displays unusually large overlaps, forming a well-defined cluster separated from the thermal bulk. Figure adapted from [10]

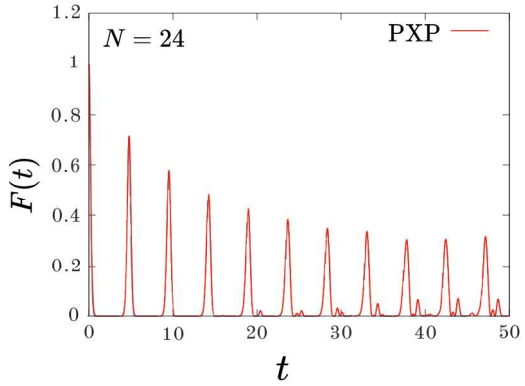

Figura 5 – Time evolution of the fidelity $F(t)$ for the PXP model with 24 sites and periodic boundary conditions, initialized in $|\psi(0)\rangle = |\mathbb{Z}_2\rangle$. The fidelity exhibits pronounced revivals, indicating that the system periodically returns close to its initial configuration instead of relaxing to a thermal steady state. Figure adapted from [73].

we can see in Figura 6, $|\mathbb{Z}_2\rangle$ has a high overlap with a special band separated from the remaining eigenstates.

The first observation of coherent oscillations in observables associated with quantum many-body scars was reported by Bernien *et al.* (2017) [9] in an experiment with Rydberg atom arrays. In this setup, individual ^{87}Rb atoms were trapped in an optical lattice and coherently driven between the ground $|g\rangle$ and highly excited Rydberg $|r\rangle$ states by a two-photon transition, as illustrated in Fig. 7. The excitation lasers, with wavelengths of 420 nm and 1013 nm, couple the atomic states with effective Rabi frequency Ω and detuning Δ, while strong van der Waals interactions V_{ij} between nearby Rydberg atoms impose the so-called *Rydberg blockade*, preventing simultaneous excitation of neighboring

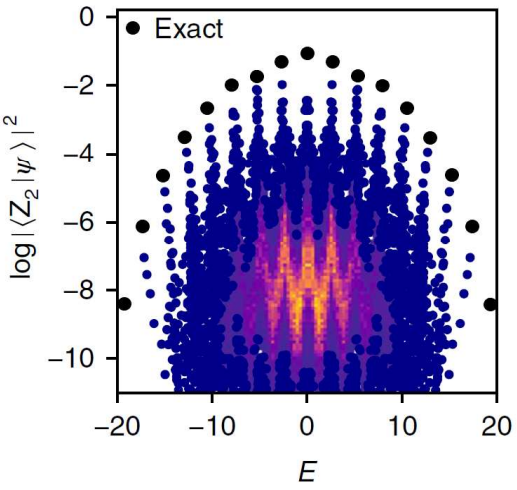

Figura 6 – Logarithm of the squared overlap $|\langle \mathbb{Z}_2|\psi_i\rangle|^2$ between the $|\mathbb{Z}_2\rangle$ initial state and the many-body eigenstates $|\psi_i\rangle$ of the PXP Hamiltonian, obtained by exact diagonalization. The horizontal axis shows the eigenstate energy E_i, and the vertical axis quantifies the overlap amplitude. Colors represent the density of eigenstates: bright regions indicate energy ranges where many states have similar small overlaps, while darker regions correspond to sparser distributions. A small set of eigenstates near the center of the spectrum displays unusually large overlaps, forming a distinct band separated from the thermal bulk. These states are approximately equally spaced in energy by $\Omega \approx 1.33$, which determines the frequency of the fidelity revivals observed in the dynamics. Figure adapted from [10].

atoms. This interaction constraint effectively maps the system onto a one-dimensional spin chain governed by the PXP Hamiltonian [Eq. (2.12)]. Starting from an ordered Néel-like configuration $|\mathbb{Z}_2\rangle$, the experiment revealed unexpected long-lived oscillations in the domain-wall density, defined as the spatial average of the nearest-neighbor anti-correlation. The temporal evolution is shown in Fig. 8.

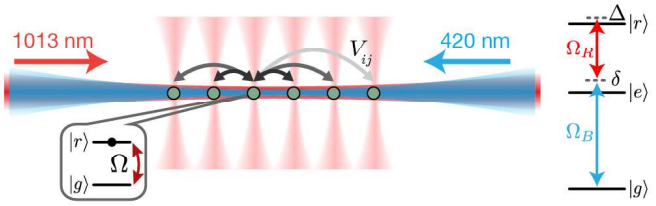

Figura 7 – Schematic representation of the Rydberg atom experiment by Bernien *et al.* [9]. Each atom (green circle) is trapped in an optical tweezer and coupled to a highly excited Rydberg state $|r\rangle$ via a two-photon transition with laser wavelengths 420 nm and 1013 nm. The strong van der Waals interaction V_{ij} between neighboring Rydberg atoms produces the *Rydberg blockade*, which forbids simultaneous excitations of adjacent atoms. This constraint realizes an effective spin-1/2 chain described by the PXP Hamiltonian. The energy-level diagram on the right shows the two-photon coupling between $|g\rangle$ and $|r\rangle$ with intermediate detuning δ and total Rabi frequency Ω. Figure adapted from [9].

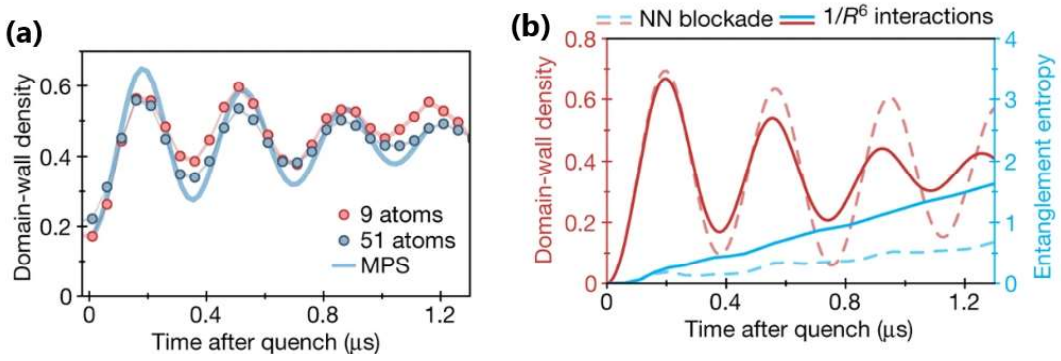

Figura 8 – Comparison between experimental and theoretical dynamics of Rydberg atom chains [9]. **(a)** Time evolution of the domain-wall density measured experimentally for chains of 9 and 51 atoms (dots) together with matrix product state simulations (lines). **(b)** Numerical simulations of the PXP model: domain-wall density (red) and bipartite entanglement entropy (blue) as functions of time. Dashed lines correspond to the ideal blockade constraint, while solid lines include the full Rydberg interaction potential. Both experiment and theory show coherent oscillations of the domain-wall density, revealing long-lived nonthermal dynamics characteristic of the $|\mathbb{Z}_2\rangle$ initial state. Figure adapted from [9].

2.5.4 Constrained Hilbert Space and Effective Dynamics

The PXP model operates under a strict dynamical constraint: two neighboring sites cannot be simultaneously in the spin-up state due to the Rydberg blockade mechanism. This restriction effectively projects the full Hilbert space of a spin-1/2 chain onto a smaller subspace, where the configurations $|\cdots \bullet\bullet \cdots\rangle$ are forbidden. As shown in Eq. (2.12), the Hamiltonian includes projectors that enforce this constraint dynamically. As a result, the evolution is not only confined to the allowed subspace, but this subspace is strictly preserved by H_{PXP}, meaning that no transitions out of it are possible under the dynamics.

This constraint leads to a substantial reduction in the dimensionality of the Hilbert space. While the full spin-1/2 chain has 2^N basis states for a chain of N sites, the constrained subspace — often referred to as the *Fibonacci Hilbert space* — grows asymptotically as φ^N, where $\varphi = (1+\sqrt{5})/2$ is the golden ratio. This behavior arises because each spin-up site must be followed by a ground state, yielding a recursive structure analogous to Fibonacci sequences [10]. For instance, for $N = 30$, the constrained space contains approximately 1.6×10^6 states, in contrast to over 10^9 in the full space.

The effects of the Rydberg blockade become more evident when analyzing the structure of the accessible configuration space. In the PXP model, each spin configuration that satisfies the blockade constraint can be represented as a node in a graph, and two configurations are connected by an edge if they are coupled by the Hamiltonian, that is, if one can be obtained from the other by flipping a single spin that is allowed under the constraint. Figure 9 shows this connectivity graph for a short chain of length $L = 6$, containing only configurations without adjacent excitations. This representation highlights

how the Rydberg blockade limits the connectivity of the Hilbert space, producing a structured network of states that constrains the system's dynamics within a reduced portion of the full configuration space [10].

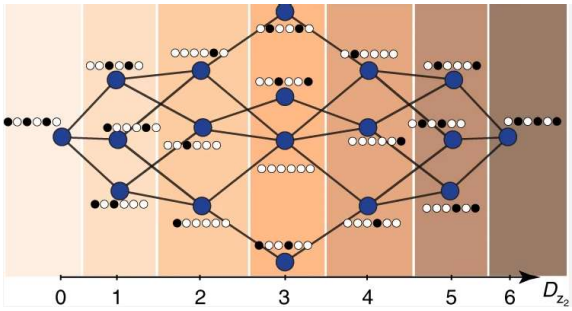

Figura 9 – Connectivity graph of the constrained Hilbert space for a short PXP chain ($L = 6$) [10]. Each node represents a valid spin configuration that satisfies the Rydberg blockade constraint, and edges denote allowed transitions between configurations generated by the PXP Hamiltonian. This restricted connectivity illustrates how the blockade constraint fragments the full Hilbert space into a smaller, structured subspace, providing an intuitive picture of the nonthermal dynamics that arise in the PXP model. Figure adapted from [10].

This structure results in a reduced and highly nontrivial pattern of connectivity among the remaining configurations. Unlike unconstrained spin systems, where the connectivity graph is typically uniform and densely connected due to the action of local terms that can flip any spin independently, the PXP model exhibits a much more structured topology. In models such as the transverse-field Ising or Heisenberg chains, each basis configuration is connected to many others through single-site or two-site operators acting freely across the entire chain. As a result, the graph of basis states in these systems forms a highly regular and symmetric structure, with each node linked to a large and roughly equal number of neighbors. In contrast, the Rydberg blockade imposes local constraints that eliminate many of these transitions, leading to a sparse and heterogeneous connectivity pattern. These constraints shape the dynamical evolution of the system and are believed to be directly responsible for the emergence of anomalous non-thermal behavior [30].

Importantly, certain initial states such as the Néel-like configuration $|\mathbb{Z}_2\rangle = |\bullet\circ\bullet\circ\cdots\rangle$ are dynamically restricted to a narrow region of this graph. Their evolution remains within a low-dimensional sector, where transitions to other configurations are suppressed. This limited exploration of the available state space gives rise to non-thermal behavior, including long-lived oscillations and revivals in local observables and fidelity [9, 10].

Thus, the constrained Hilbert space is not just a technical feature of the PXP model, but a central element in its dynamical properties. The blockade-induced projection breaks the assumptions typically associated with thermalization, such as uniform sampling of the full Hilbert space, and creates conditions favorable for the appearance of quantum

many-body scars. Understanding the geometry and connectivity of this subspace is essential for analyzing how robust these scars are under various perturbations, as will be explored in the following chapters.

2.6 Scar towers and the origin of nonthermal dynamics

A hallmark of quantum many-body scars is the presence of a small set of eigenstates that violate the eigenstate thermalization hypothesis (ETH). These states are not isolated anomalies but form an approximately equidistant sequence within the many-body spectrum, referred to as the *scar tower*. Their presence is directly linked to the long-lived coherent oscillations, reduced entanglement growth, and weak ergodicity breaking observed in constrained systems such as the PXP model.

Regularity in the energy spectrum

The characteristic tower of scarred eigenstates discussed in Section 2.4 is clearly reflected in the spectral structure of the PXP model. When the system is initialized in the Néel state $|\mathbb{Z}_2\rangle$, a small number of eigenstates exhibit large overlap with the initial state and are arranged with nearly uniform energy spacing. This regular spacing leads to constructive quantum interference at periodic intervals, manifesting as revivals in the fidelity. The revival period is set by the inverse of the energy spacing ε through the relation

$$T = \frac{2\pi}{\varepsilon}.$$

The distribution of overlaps between the eigenstates of the PXP Hamiltonian and the Néel state, shown in Fig. 6, highlights the characteristic spectral structure associated with scarred dynamics. The eigenstates with the largest overlaps stand out from the thermal bulk, forming a nearly harmonic ladder centered around zero energy. This structure, however, is only approximately regular. By adding vertical markers to the overlap distribution, as shown in Fig. 10, one can visualize that the eigenstates with the most significant overlaps with the $|\mathbb{Z}_2\rangle$ state are approximately equally spaced in energy. These states correspond to the scarred eigenstates responsible for the quasi-tower structure and the periodic revivals observed in the dynamics.

The Forward Scattering Approximation (FSA)

The regularity observed in the scarred eigenstates of the PXP model, discussed in the previous section, suggests that the dynamics initialized in the Néel state $|\mathbb{Z}_2\rangle$ is effectively confined to a highly restricted subspace of the full Hilbert space. The Forward Scattering Approximation (FSA) is a variational framework designed to capture this subspace and describe the associated nonthermal dynamics.

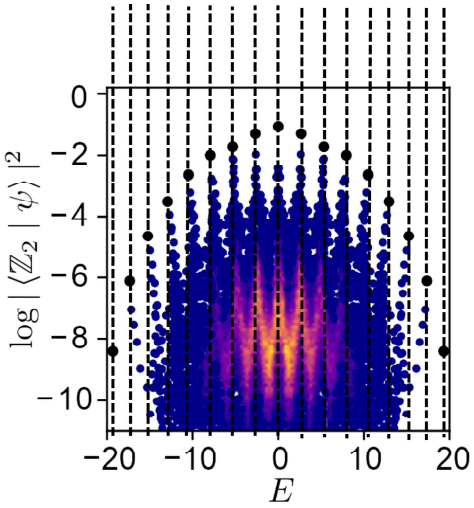

Figura 10 – Same data as in Fig. 6, now with vertical dashed lines added as visual guides to highlight the approximately regular energy spacing between the eigenstates with the largest overlaps with the $|\mathbb{Z}_2\rangle$ state. Figure adapted from [10].

The construction of the FSA begins by recognizing that the Néel state is located at one extremity of the Hilbert space in terms of Hamming distance relative to other configurations [11]. The PXP Hamiltonian acts as a hopping operator within this constrained space, allowing transitions that increase or decrease the number of domain walls (i.e., changes in the spin configuration) while respecting the Rydberg blockade constraint.

The FSA systematically constructs a basis by following the forward-scattering paths generated by successive applications of the Hamiltonian. Starting from the initial state $|v_0\rangle = |\mathbb{Z}_2\rangle$, each subsequent vector is generated by applying H to the previous one while orthogonalizing against earlier vectors to maintain linear independence:

$$|v_1\rangle \propto H\,|v_0\rangle \tag{2.23}$$

$$|v_{n+1}\rangle \propto H\,|v_n\rangle - \beta_n\,|v_{n-1}\rangle \tag{2.24}$$

where β_n ensures orthonormality at each step. This iterative process is mathematically equivalent to generating a Krylov subspace — the linear subspace spanned by the vectors $\{|v_0\rangle, H\,|v_0\rangle, H^2\,|v_0\rangle, \dots\}$ — or, equivalently, to performing a Lanczos tridiagonalization centered around the initial state. This procedure constructs an orthonormal basis in which the Hamiltonian has a tridiagonal form, capturing the dominant directions of the dynamics projected from the initial state [74].

In this basis, the Hamiltonian takes the form of a tridiagonal matrix, with nonzero elements only connecting neighboring basis vectors. The resulting matrix has a perfectly tridiagonal structure, as shown in Fig. 11, reflecting the constraint that the dynamics only couples successive forward-scattering states:

$$H_{\text{FSA}} = \sum_n \beta_n \left(|v_n\rangle\langle v_{n+1}| + |v_{n+1}\rangle\langle v_n|\right). \tag{2.25}$$

The dimension of the FSA basis scales linearly with system size and corresponds to the maximum reachable Hamming distance from the initial state. For the Néel state in a chain of length L, the number of basis vectors is $L/2 + 1$, reflecting the maximum number of allowed excitations under the blockade constraint.

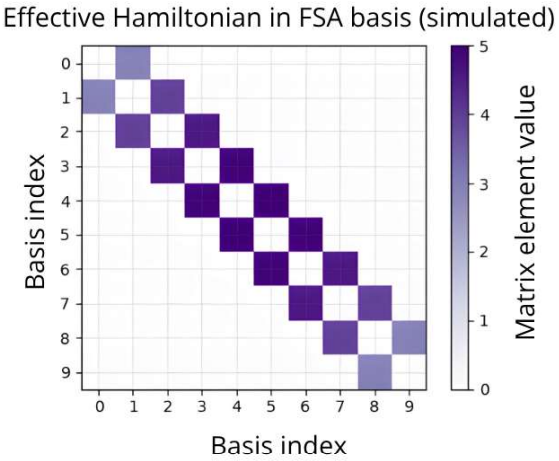

Figura 11 – Matrix representation of the Hamiltonian projected onto the FSA basis. The tridiagonal structure reflects the restriction of dynamics to successive basis states $|v_n\rangle$, characteristic of forward-scattering processes.

The tridiagonal form of H_{FSA} captures the essential feature of the dynamics: the system coherently oscillates between the extremal states of the tower, leading to the periodic revivals observed in real-time evolution. This effective dynamics is highly reminiscent of a large spin precessing under a transverse field, with the analogy becoming particularly evident when examining the structure of the scarred eigenstates.

Effective $\mathfrak{su}(2)$ dynamics

The tridiagonal structure of the Hamiltonian in the FSA basis is not merely a mathematical artifact but reflects a deeper physical organization within the constrained Hilbert space of the PXP model. Understanding this structure is essential for explaining why the system exhibits robust nonthermal dynamics and periodic revivals when initialized in the Néel state. In particular, the FSA subspace possesses an approximate $\mathfrak{su}(2)$ algebraic structure, where the forward-scattering basis states form a ladder analogous to that of a collective spin. This correspondence provides not only an intuitive picture of the scar dynamics, but also a concrete explanation for the nearly harmonic energy spacing observed in the scar tower. The effective spin picture plays a central role in understanding the stability of quantum many-body scars and will serve as a foundation for the perturbative analysis discussed in the following chapters.

The tridiagonal form of the Hamiltonian projected onto the FSA basis naturally suggests a correspondence with an effective $\mathfrak{su}(2)$ algebra. In this picture, the forward-

scattering basis vectors $|v_n\rangle$ play the role of spin states in a collective spin-S system, with $S = L/2$ for a chain of length L.

The basis states can be identified with eigenstates of the S^z operator, such that

$$S^z |v_n\rangle = (n - M/2) |v_n\rangle , \tag{2.26}$$

where $M = L/2$ is the maximum Hamming distance (or the maximum number of allowed forward-scattering steps from the initial state). The raising and lowering operators act as

$$S^+ |v_n\rangle \propto |v_{n+1}\rangle , \quad S^- |v_n\rangle \propto |v_{n-1}\rangle . \tag{2.27}$$

The tridiagonal connectivity of the FSA Hamiltonian — with nearly uniform off-diagonal elements between $|v_n\rangle$ and $|v_{n\pm1}\rangle$ — closely mirrors the structure of the S^x operator in the S^z-diagonal basis of a collective spin. In particular, since $S^x = \frac{1}{2}(S^+ + S^-)$ generates transitions between adjacent spin states, we can approximate the projected Hamiltonian as

$$H_{\text{FSA}} \approx \alpha S^x. \tag{2.28}$$

This leads to coherent oscillations analogous to Rabi flopping between the extremal spin states, as the system undergoes a precession-like motion in the effective spin space. Starting from an extremal state such as $|v_0\rangle$, the dynamics traverse the ladder of scarred eigenstates in a periodic manner. The energy spectrum within the FSA subspace resembles that of a large spin in a transverse field, resulting in an approximately harmonic level structure that reinforces the coherence of the revivals observed in the PXP model.

The ladder structure of the scarred eigenstates is illustrated in Fig. 12, where each level corresponds to one of the FSA basis vectors, and the raising and lowering operators connect adjacent levels.

The resulting organization of the scarred eigenstates within the FSA subspace is illustrated in Fig. 12. Each level represents one of the FSA basis vectors, and the effective raising and lowering operators connect neighboring levels, forming a ladder analogous to that of a collective spin precessing in a transverse field.

Limitations and generalizations

While the Forward Scattering Approximation provides a remarkably accurate description of the scarred subspace and captures the essential mechanism behind the revival dynamics in the PXP model, it remains an approximation with intrinsic limitations. The FSA captures only a small fraction of the total Hilbert space, specifically the subspace connected to the Néel state through successive forward-scattering processes. As a result, it accurately describes the scarred eigenstates responsible for the observed nonthermal dynamics but fails to capture the thermal bulk of the spectrum.

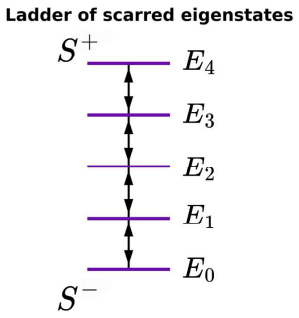

Figura 12 – Schematic representation of the scarred eigenstates within the FSA subspace. Each level corresponds to one of the FSA basis vectors, and the effective raising and lowering operators S^+ and S^- connect neighboring levels, forming a ladder analogous to that of a collective spin in a transverse field. This visualization highlights the approximate $\mathfrak{su}(2)$ structure underlying the dynamics captured by the FSA..

Moreover, the FSA neglects interference paths that involve backward-scattering processes or more complex trajectories within the constrained Hilbert space. These processes contribute to the gradual leakage of probability amplitude from the scar subspace into the thermal continuum, ultimately leading to the imperfect nature of the revivals and the eventual thermalization observed at very long timescales.

Despite these limitations, the conceptual framework behind the FSA has inspired generalizations to other systems. Notably, exact scar towers have been constructed in models such as the spin-1 Affleck–Kennedy–Lieb–Tasaki (AKLT) chain [51], the spin-1 XY model [52], and in the context of the Hubbard model through the η-pairing mechanism [42]. In these cases, the scarred eigenstates are stabilized by exact spectrum-generating algebras, making the scar subspace completely decoupled from the thermal continuum.

These generalizations demonstrate that scar dynamics is not restricted to the PXP model but rather represents a broader phenomenon that can emerge in various constrained or symmetry-protected systems. Understanding both the strengths and the limitations of the FSA framework is essential, as it provides the conceptual foundation for analyzing how quantum many-body scars respond to perturbations, a question that will be addressed in the following chapters.

3 Perturbations on the PXP model

The discovery of quantum many-body scars (QMBS) in the PXP model has challenged conventional notions of ergodicity and thermalization in nonintegrable systems [10]. As discussed in the previous chapter, the scarred eigenstates form an approximately equidistant tower embedded within the thermal spectrum, sustained by an effective $\mathfrak{su}(2)$ dynamical structure. This emergent algebraic organization confines the dynamics to a small subspace when the system is initialized in special product states, such as the Néel state $|\mathbb{Z}_2\rangle$, leading to coherent oscillations and long-lived revivals.

However, this nonthermal behavior is known to be fragile under various types of perturbations [75]. From both an experimental and theoretical perspective, understanding the stability of quantum many-body scars is crucial. In realistic platforms, such as Rydberg atom arrays, imperfections are inevitable. These include local disorder, fluctuations in coupling strengths, and inaccuracies in the preparation of the initial state [9]. Theoretically, perturbations serve as probes that reveal how robust the scarred subspace is: whether the effective $\mathfrak{su}(2)$ dynamics can be preserved, or whether leakage into the thermal bulk becomes dominant.

Previous studies have shown that even weak perturbations can suppress revivals, enhance entanglement growth, or destroy the regular spectral structure associated with the scar tower [75, 76]. On the other hand, certain fine-tuned or symmetry-preserving deformations can stabilize the scarred dynamics, demonstrating that the phenomenon lies on a delicate balance between kinetic constraints and Hamiltonian symmetries.

In this chapter, we systematically explore different classes of perturbations and their impact on the stability of QMBS in the PXP model. We distinguish between perturbations to the Hamiltonian—such as disorder, interaction terms, and Schrieffer-Wolff corrections—and imperfections in the initial state. Each of these mechanisms can be understood in terms of their effect on the preservation or breakdown of the effective scar subspace, and consequently, on the deformation or collapse of the tower structure introduced in Chapter 2.

The analysis presented here not only clarifies the nature of scar stability but also provides a conceptual foundation for the numerical investigations in the following chapters.

3.1 Classification of Perturbations

Understanding the stability of quantum many-body scars requires a systematic classification of perturbations according to how they affect the constrained dynamics and

the scarred subspace. From the perspective of the effective $\mathfrak{su}(2)$ dynamics introduced in Chapter 2, perturbations can be broadly characterized based on whether they preserve the forward-scattering ladder structure or introduce processes that induce leakage into the thermal bulk.

Perturbations can be grouped into two primary categories:

- **Perturbations to the Hamiltonian**: These include modifications to the interaction terms, local disorder, and additional couplings that may or may not respect the kinetic constraints imposed by the Rydberg blockade. Some perturbations preserve the blockade constraint and act within the constrained Hilbert space (e.g., projected disorder), while others allow the system to access configurations outside the constrained subspace (e.g., unprojected disorder or beyond-PXP corrections).
- **Defects in the initial state**: Even when the Hamiltonian remains unchanged, imperfect state preparation can significantly affect the dynamics. Deviations from the ideal Néel state reduce the overlap with the scarred eigenstates and, consequently, suppress revivals. These imperfections effectively act as a perturbation to the initial condition, changing the projection of the initial state onto the scarred subspace.

A finer classification can also be made according to symmetry considerations. Some perturbations preserve the spatial inversion symmetry (parity) or other discrete symmetries of the PXP model, while others explicitly break them. The impact of perturbations is tightly linked to whether they respect or deform the emergent $\mathfrak{su}(2)$ structure responsible for the scar tower. Symmetry-preserving perturbations may deform the ladder while retaining its qualitative features, whereas symmetry-breaking perturbations often lead to the collapse of the tower.

Table 1 summarizes the different perturbations studied in this work, classifying them according to whether they act on the Hamiltonian or the initial state, and whether they preserve or break the scar subspace structure.

3.2 Effects of initial state defects

A central aspect of quantum many-body scar dynamics is the strong dependence on the choice of initial state. In particular, the revival phenomena observed in the PXP model are closely tied to specific configurations, most notably the Néel-like state $|\mathbb{Z}_2\rangle$, which displays high overlap with a small set of atypical eigenstates and gives rise to long-lived coherent oscillations [11, 22].

In experimental realizations, however, imperfections in state preparation are inevitable and may result in local deviations from the ideal pattern [9]. Although the direct

impact of such local imperfections on scarred dynamics remains an open question, it is reasonable to expect that even minor changes to the initial configuration can significantly affect the system's evolution. In particular, whether or not a perturbation respects the kinetic constraint may influence the degree to which the dynamics remain confined within the scarred subspace.

Motivated by this, we examine two distinct types of single-site deviations from the ideal $|\mathbb{Z}_2\rangle$ pattern. In the first case, a spin initially in the down state is flipped up, placing two adjacent up spins side by side and thus violating the Rydberg blockade constraint. In the second case, a spin that was originally up is flipped down, which preserves the blockade but breaks the perfect alternation pattern of the initial state. These configurations allow us to probe different aspects of the dynamics: the former challenges the validity of the constrained manifold, while the latter explores the robustness of scarring within the projected subspace.

We emphasize that this section is devoted to the physical motivation and classification of the initial state perturbations. The numerical results and dynamical consequences of these defects will be presented and analyzed in Chapter 4.2.

3.2.1 Up-flip defect: blockade violation

We begin by analyzing the case in which a spin initially in the down state is flipped up within the $|\mathbb{Z}_2\rangle$ pattern. This leads to the formation of three consecutive spin-up sites in the configuration, explicitly violating the Rydberg blockade condition that prohibits neighboring excitations. A graphical representation of the modified state is given by

$$|\mathbb{Z}_2^{\uparrow}\rangle = |\cdots \bullet \circ \bullet \underline{\bullet} \bullet \circ \cdots\rangle\,, \tag{3.1}$$

where $\bullet$ denotes a spin-up, $\circ$ a spin-down, and the underlined site indicates the flipped spin. In this example, the central defect results in the subsequence $|\bullet\ \bullet\ \bullet\rangle$, which is dynamically forbidden in the ideal PXP model.

This type of defect naturally models experimental imperfections, such as spontaneous excitations or local addressing errors during state initialization [9]. Its presence provides a direct probe into how robust the revival dynamics are when the initial state includes configurations outside the constrained Hilbert space for which the Hamiltonian was designed

From a theoretical perspective, the presence of this defect introduces components in the initial state that are dynamically connected to a much larger portion of the full Hilbert space. While the ideal PXP Hamiltonian restricts the dynamics to a constrained subspace, the up-flip defect allows for leakage into forbidden sectors, potentially leading to faster decoherence, thermalization, or suppression of revivals.

In the next subsection, we turn to a second type of defect that does not violate the blockade constraint, but still breaks the spatial symmetry of the initial configuration.

3.2.2 Down-flip defect: constrained subspace modification

We now consider a different type of defect, in which a spin that is up in the original $|\mathbb{Z}_2\rangle$ configuration is flipped down. Unlike the up-flip defect discussed previously, this modification does not violate the Rydberg blockade constraint, since no pair of adjacent spin-up sites is created. However, the alternation pattern that defines the $|\mathbb{Z}_2\rangle$ state is broken, and the resulting state no longer belongs to the forward-scattering subspace typically associated with strong revivals.

The modified state can be represented as

$$|\mathbb{Z}_2^{\downarrow}\rangle = |\cdots \bullet \circ \underline{\circ} \circ \bullet \circ \cdots\rangle\,, \tag{3.2}$$

where the underlined site indicates the spin-down flip applied to a position that was originally spin-up. This leads to a configuration in which two neighboring spins are simultaneously in the down state—a situation that is allowed by the blockade, but absent in the ideal $|\mathbb{Z}_2\rangle$ pattern.

This type of defect is relevant in experiments where state preparation errors may involve missing excitations, either due to loss of atoms or imperfect addressing. Because the resulting state still lies within the constrained Hilbert space, its dynamics are governed entirely by the PXP Hamiltonian. Nevertheless, the initial state's overlap with the scarred eigenstates is expected to be strongly reduced, which may result in a suppression of coherent revivals.

By comparing this case with the up-flip defect, we can distinguish between effects due to leakage from the constrained subspace and those arising from perturbations that remain internal to it.

3.3 Corrections from the Schrieffer-Wolff expansion

Recall that the effective PXP model can be derived from a one-dimensional chain of Rydberg atoms operating under the strong blockade regime, where the van der Waals interaction between neighboring excited atoms prohibits simultaneous excitations on adjacent sites. In this regime, the dynamics is well described by a constrained Hilbert space governed by a projected Hamiltonian.

In realistic setups the Rabi frequency Ω used to drive the transitions between ground and excited states can vary across the chain. This site-dependent Rabi coupling, denoted by Ω_i, arises from imperfections in laser profiles, inhomogeneities in the atomic

arrangement, or intentional site addressing. As a result, even the leading-order effective model that captures the constrained dynamics becomes spatially inhomogeneous:

$$H_{\text{eff}} = \sum_i \Omega_i \, P_{i-1} X_i P_{i+1}, \tag{3.3}$$

where $P_i = |0\rangle\langle 0|$ projects site i onto the ground state and X_i is the Pauli-X operator acting on site i. This spatial variation breaks the uniformity of spin rotations across the chain, disrupting the coherent evolution that underlies many-body revivals. In the ideal case of constant $\Omega_i = \Omega$, all allowed spin flips occur with the same strength, enabling collective dynamics and enhancing the visibility of scarred oscillations.

However, in realistic implementations, the blockade constraint does not emerge as an exact projection but rather as a large energy penalty in the microscopic Hamiltonian. This raises the natural question of how higher-order corrections, arising from virtual transitions into forbidden configurations, affect the dynamics.

To address this, we consider the effective Hamiltonian obtained via a Schrieffer-Wolff (SW) transformation, which perturbatively projects the full dynamics onto the constrained subspace while accounting for the influence of virtual excitations. The detailed derivation of this correction is presented in Appendix A.

The leading correction appears at second order and corresponds to a correlated two-site hopping process that preserves the blockade constraint. The corrected Hamiltonian takes the form

$$\delta H_{\text{SW}} = \sum_j g_j \, P_{j-1} \left(\sigma_j^+ \sigma_{j+1}^- + \sigma_j^- \sigma_{j+1}^+ \right) P_{j+2}, \tag{3.4}$$

where the coupling constant is given by

$$g_j = \frac{\Omega_j (\Omega_{j-1} + \Omega_{j+1})}{8V}, \tag{3.5}$$

with V representing the nearest-neighbor interaction energy between excited atoms. This term reflects a physically motivated correction derived from the microscopic Rydberg Hamiltonian, where the system briefly visits energetically forbidden states through virtual processes before returning to the constrained subspace.

From a physical standpoint, this correction enhances the connectivity within the constrained Hilbert space. It allows for coherent two-site transitions that depend on the blockade condition of the surrounding sites. Previous studies have shown that including such terms can improve the spectral structure associated with quantum many-body scars, increase the overlap with scarred eigenstates, and stabilize revivals by mitigating leakage into thermalizing sectors [24, 75].

In this thesis, we analyze how the inclusion of the Schrieffer-Wolff correction affects scar dynamics, particularly focusing on fidelity revivals and correlation functions. Our implementation follows the perturbative framework derived in Appendix A, and the analysis is carried out both in isolation and in combination with other perturbations.

3.4 Disordered Hamiltonian Perturbations

In experimental quantum simulators, disorder is practically unavoidable, arising from small imperfections such as fluctuations in trapping potentials, laser intensities, and local electromagnetic fields [77, 78]. In Rydberg atom arrays, these imperfections manifest as spatial inhomogeneities of the Rabi frequencies, fluctuations in local detunings, and occasional atom loss [79, 80]. Understanding how such sources of disorder affect the stability of quantum many-body scars is essential, both for the correct interpretation of experimental results and for assessing the fundamental robustness of nonthermal dynamics.

In this work, we explore two distinct classes of disordered perturbations applied to the PXP model. The first class consists of unconstrained disorder, where local operators act on all configurations without enforcing the Rydberg blockade constraint. This type of perturbation allows the system to access forbidden states outside the constrained Hilbert space, providing a way to probe the resilience of scars when the constraint is explicitly broken.

The second class consists of projected disorder, in which the perturbations are conditioned on the blockade constraint being satisfied. This preserves the constrained Hilbert space but introduces spatial inhomogeneities that deform the dynamics internally. Projected disorder enables us to examine how sensitive scarred dynamics are to perturbations that respect the constraint but disrupt the coherent interference patterns responsible for revivals.

These two complementary approaches allow us to disentangle the role of the constrained structure itself from the effects of disorder within the scar-supporting subspace.

3.4.1 Effects of unprojected disorder

We begin by considering generic local disorder acting independently on each site along all spin directions. The perturbation is described by the Hamiltonian

$$\delta H = \sum_{i=1}^{L} \left(h_X^i X_i + h_Y^i Y_i + h_Z^i Z_i \right), \tag{3.6}$$

where the coefficients h_α^i for $\alpha \in X, Y, Z$ are drawn independently from a uniform distribution within a symmetric interval $[-W/2, W/2]$. This type of perturbation introduces disorder along all three axes of the Bloch sphere and acts without any projection operators enforcing the blockade constraint.

This is the simplest possible way of introducing a perturbation that acts locally on a single site, without considering any constraint or projection. Perturbations of this form are commonly employed in studies of Ising-like models and other lattice spin systems

to probe thermalization, localization, and ergodicity breaking. However, it is important to emphasize that this is not the direct motivation in the present context, where our focus is on using it as a tool to test the robustness of the scarred dynamics under generic constraint-breaking deformations.

Since the operators X_i, Y_i, and Z_i act unconditionally, the system is no longer restricted to the constrained Hilbert space defined by the Rydberg blockade. The dynamics can explore any configuration, including those that violate the blockade condition by creating neighboring excitations.

This behavior is represented symbolically in Figure 13c. In this illustration, the removal of the constraint is depicted as the ability of the dynamics to access a broader region of the state space. While the figure is not a literal representation of the many-body Hilbert space, it serves as a conceptual aid to contrast constrained and unconstrained dynamics. Without the constraint, the dynamics can explore a much larger portion of the Hilbert space, potentially leading to rapid thermalization, enhanced entanglement growth, and the suppression of revivals.

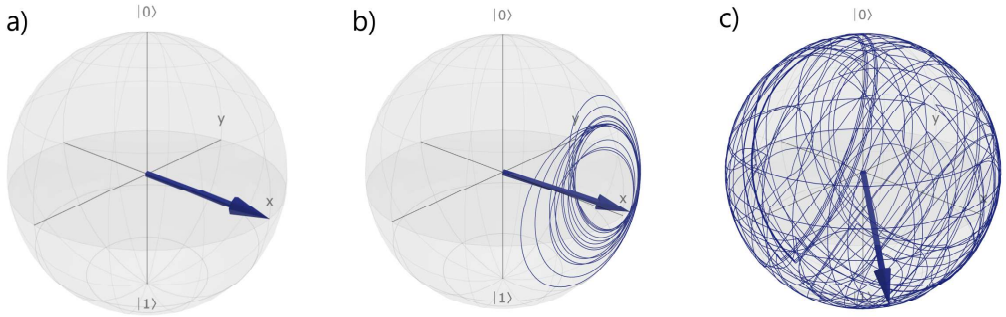

Figura 13 – Schematic representation of the effect of Hamiltonian perturbations on the dynamics. The state evolution is represented symbolically as trajectories on a Bloch sphere for illustrative purposes. Panel (a) indicates the initial state, while panel (b) shows the restricted dynamics under a projected Hamiltonian that preserves the Rydberg blockade constraint. Panel (c) illustrates the dynamics when nonprojected perturbations are included, allowing access to states outside the constrained subspace. The figure is not a literal depiction of many-body state evolution, but rather a conceptual aid to contrast the two types of dynamical behavior. Created with Bloch Sphere Simulator [81]

This perturbation allows us to probe the sensitivity of scarred dynamics to generic symmetry-breaking deformations and constraint violations. Furthermore, it provides a baseline against which we can compare the effect of projected disorder terms that act within the constrained subspace.

3.4.2 Effects of projected disorder

We now turn to a modified version of the disordered perturbation, in which the operators are projected to act only within the constrained Hilbert space defined by the Rydberg blockade. The corresponding Hamiltonian is

$$\delta H_{\text{proj}} = \sum_{i=1}^{L} \left(h_X^i P_{i-1} X_i P_{i+1} + h_Y^i P_{i-1} Y_i P_{i+1} + h_Z^i P_{i-1} Z_i P_{i+1} \right), \tag{3.7}$$

where $P_i = |0\rangle\langle 0|$ projects site i onto the spin-down state, ensuring that each operator acts only if both neighboring sites are also down. The coefficients h_α^i for $\alpha \in X, Y, Z$ are drawn from the same random distribution used in the unprojected case.

This projected version preserves the blockade constraint by construction. The dynamics remain fully confined to the constrained Hilbert space, but the spatial inhomogeneity introduced by the random local fields breaks the translational symmetry and modifies the structure of the effective dynamics internally.

Unlike the unconstrained disorder, which allows leakage into forbidden configurations, the projected disorder acts as an internal deformation of the PXP model. It tests the robustness of scarred dynamics to constraint-preserving perturbations, which do not alter the accessible Hilbert space but can still disrupt the fine-tuned interference patterns responsible for nonthermal behavior.

Projected disorder of this type has been employed in previous studies of constrained spin models [24, 82, 83] to explore how randomness affects nonergodic dynamics within kinetically constrained manifolds. In our case, it provides a complementary perspective: while the unconstrained disorder probes the breakdown of the blockade constraint, the projected disorder isolates the role of internal inhomogeneity within the scar-supporting subspace.

This conceptual distinction is represented symbolically in Figure 13b, where the dynamics are confined to a restricted region of the state space due to the blockade constraint, but still subject to random deformations. As in the previous case, the figure is not a literal depiction of the many-body Hilbert space, but serves as a useful visual aid to contrast the nature of constrained dynamics with and without disorder.

These two types of perturbations allow us to probe distinct aspects of scar stability: the unprojected disorder tests the resilience of nonthermal behavior when the system is allowed to leave the constrained subspace, while the projected version isolates the role of local inhomogeneity within the scar-supporting manifold. In the results chapter, we analyze the impact of both perturbations on observables such as fidelity, spatial correlations, and entanglement entropy.

Tabela 1 – Summary of the perturbations studied in this work, their relation to the constrained subspace, their physical motivation, and their purpose in analyzing the stability of quantum many-body scars.

Perturbation	Subspace preserved?	Physical motivation	Purpose
Initial state defects	Depends (blockade violation: No; constrained defect: Yes)	Experimental imperfections in state preparation	Probe sensitivity to local errors; modify initial overlap with scarred eigenstates
SW correction	Yes	Derived from microscopic Rydberg Hamiltonian via Schrieffer-Wolff expansion	Introduce realistic corrections within the constrained dynamics; enrich kinetic pathways
Unprojected disorder	No	Computational probe; standard in spin models (e.g., Ising-like systems)	Test scar robustness beyond the constrained manifold; evaluate impact of constraint-breaking deformations
Projected disorder	Yes	Generalized PXP with spatially inhomogeneous couplings	Explore how internal disorder affects coherence and revivals within the constrained subspace

4 Numerical Results: Stability Analysis of Quantum Many-Body Scars

This chapter presents the numerical investigation of the perturbations introduced in Chapter 3, focusing on their impact on the stability of quantum many-body scars in the PXP model. Building on the previously established conceptual framework, we analyze how different mechanisms—including initial-state defects, Hamiltonian corrections, and disorder—affect revival dynamics, entanglement growth, and spectral signatures. The results of this research were published in 2025 *Physica Scripta* [84].

The numerical approach combines exact diagonalization techniques with time-evolution simulations on finite chains. By evaluating a set of complementary observables — fidelity, bipartite entanglement entropy, and spectral overlap — we systematically quantify the degree to which each perturbation preserves, deforms, or destroys the scarred subspace responsible for nonthermal dynamics.

The chapter is organized as follows. Section 4.1 provides an overview of the numerical methods and defines the observables employed in the analysis. Section 4.2 presents the results for initial state defects, Schrieffer-Wolff corrections, and disordered perturbations, respectively. A comparative analysis summarizing the key findings is provided in Section 4.3.

4.1 Overview of Methods and Observables

This section presents the numerical framework used throughout this chapter to simulate the dynamics of the PXP model and its perturbations. The computational strategy combines exact diagonalization and time evolution of finite spin chains, considering both constrained and unconstrained dynamics. This includes the construction of the Hilbert space, the implementation of Hamiltonians that enforce the Rydberg blockade or explicitly break it, and the definition of observables used to quantify revival dynamics, entanglement growth, and spectral signatures associated with quantum many-body scars. All simulations are implemented using the Quantum Toolbox in Python (QuTiP) [85].

4.1.1 Numerical strategy

The numerical analysis developed in this work is based on exact diagonalization and time evolution of finite-size quantum chains. Simulations are implemented using the Quantum Toolbox in Python (QuTiP) [85], complemented by custom scripts developed for constrained Hilbert space construction [86].

The Hilbert space of a spin-$\frac{1}{2}$ chain with L sites has dimension 2^L, corresponding to all possible spin configurations in the computational basis. In the presence of the Rydberg blockade, this space is reduced to a constrained manifold where simultaneous excitation of neighboring sites is forbidden. The dimension of this constrained Hilbert space grows according to the Fibonacci sequence: for a chain of L sites, it is given by F_{L+2}, where F_n is the nth Fibonacci number. This exponential reduction relative to the full 2^L space has significant consequences for both the computational efficiency and the dynamical properties of the system.

The simulation strategy adopts two complementary approaches depending on the type of analysis. For time evolution, the full Hilbert space of the spin chain is constructed, with the blockade constraint enforced dynamically through the structure of the Hamiltonian itself. Specifically, terms like $P_{i-1}X_iP_{i+1}$ ensure that spin flips at site i only if both neighboring sites are down. In cases where the blockade is intentionally broken — such as in simulations involving unprojected disorder — the Hamiltonian is modified accordingly, allowing access to the full unconstrained Hilbert space. This formulation allows the same computational framework to handle both constrained and unconstrained dynamics, without the need to explicitly construct the reduced Hilbert space. Time evolution is computed using QuTiP's `sesolve` function, which solves the Schrödinger equation under unitary dynamics.

In contrast, for spectral analyses — including the calculation of bipartite entanglement entropy and the overlap between the initial state and the eigenstates of the Hamiltonian — the constrained Hilbert space is explicitly constructed. This involves generating the set of basis vectors that satisfy the Rydberg blockade condition and projecting the Hamiltonian onto this subspace before diagonalization. This step is essential for accessing the eigenstate structure relevant to scarred dynamics, as diagonalizing the full Hilbert space would be both computationally inefficient and physically meaningless in this context.

All Hamiltonians are constructed using QuTiP's operator framework, defining local operators and assembling full-chain terms via tensor products. Additional perturbations, such as site-dependent disorder and Schrieffer-Wolff corrections, are incorporated by modifying the local coefficients or including multi-site interaction terms. Further implementation details are available in the project's public repository [86]

4.2 Results

4.2.1 Dynamics with Initial State Defects

In this subsection, we present a detailed analysis of the quantum dynamics of different initial states in the PXP model. Our goal is to investigate how the choice of initial state influences the fidelity, nearest-neighbor correlations, and entanglement entropy growth, providing a quantitative understanding of the stability of quantum many-body scars in relation to state preparation. This analysis is essential to connect our theoretical results with experimental implementations in Rydberg atom chains, where imperfections in state preparation can significantly affect the robustness of quantum oscillations.

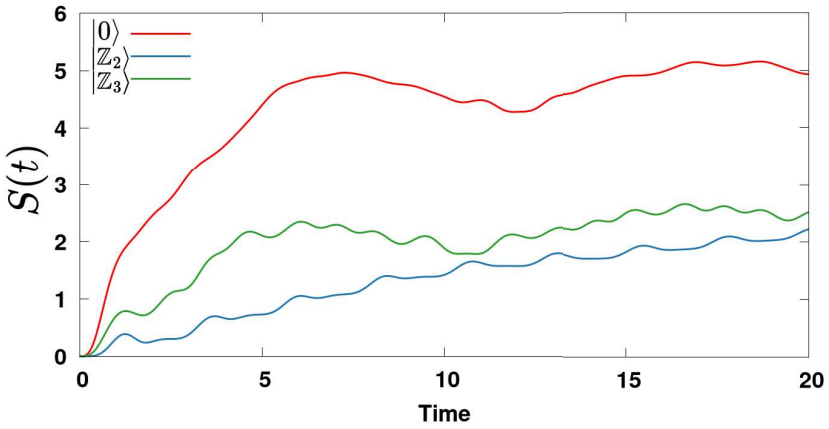

Figura 14 – Time evolution of the bipartite entanglement entropy $S(t)$ for the initial states $|\mathbb{Z}_0\rangle$, $|\mathbb{Z}_2\rangle$, and $|\mathbb{Z}_3\rangle$ in the PXP model for a system size of $L = 18$ sites. The state $|\mathbb{Z}_0\rangle$ increases rapidly and approaches the Page value, indicating rapid thermalization, whereas $|\mathbb{Z}_2\rangle$ and $|\mathbb{Z}_3\rangle$ display a slower entropy growth, consistent with the presence of quantum many-body scars.

Figure 14 shows the time evolution of the bipartite entanglement entropy $S(t)$ for three distinct initial states: $|0\rangle$, $|\mathbb{Z}_2\rangle$, and $|\mathbb{Z}_3\rangle$. As expected from previous studies of quantum many-body scars, $|\mathbb{Z}_2\rangle$ and $|\mathbb{Z}_3\rangle$ exhibit a substantially slower growth of entanglement entropy compared to $|0\rangle$, which is typically regarded as a thermal initial state. This behavior reflects the constrained dynamics and effective $\mathfrak{su}(2)$ structure that support the scarring phenomenon in the PXP model.

Because of this slow growth of entanglement entropy exhibited by $|\mathbb{Z}_2\rangle$ and $|\mathbb{Z}_3\rangle$, these states are particularly interesting for probing the stability of scars. Hence, we focus on these initial states in the subsequent analysis, where we introduce controlled local defects and investigate their impact on the scarred dynamics.

The thermal state $|0\rangle$

To establish a baseline for thermal behavior in the PXP model, we analyze the time evolution of the fully polarized state $|0\rangle$, where all spins are initially in the down configuration. This state is typically regarded as a thermal initial condition and serves as a reference for ergodic dynamics in constrained spin chains.

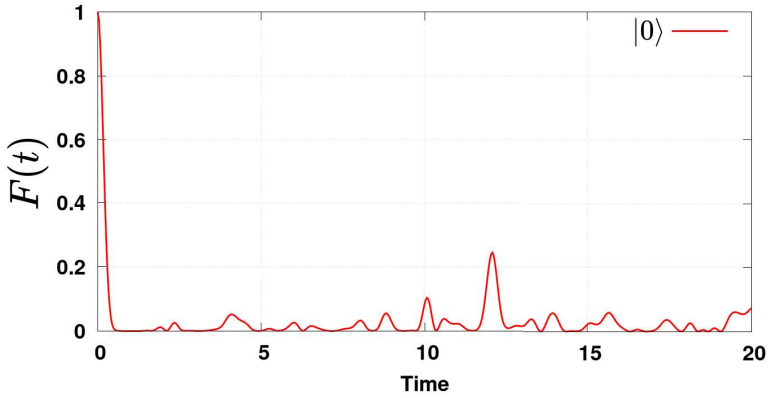

(a)

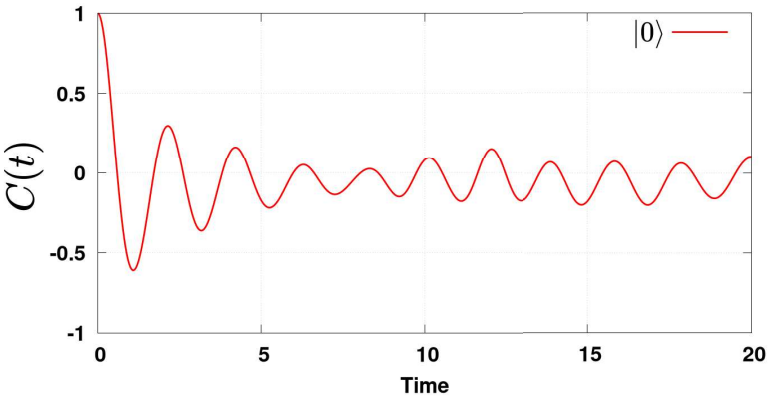

(b)

Figura 15 – (a) Time evolution of the fidelity $F(t)$ and (b) nearest-neighbor correlation $C(t)$ for the thermal state $|0\rangle$ in the PXP model with $L = 18$ sites. Both observables exhibit rapid relaxation without coherent oscillations, indicating thermal behavior.

As shown in Fig. 15, the fidelity $F(t)$ quickly decays and exhibits only small, irregular oscillations with low amplitude. This behavior signals the absence of coherent revivals and is consistent with ergodic dynamics. The nearest-neighbor correlation $C(t)$ starts from its maximal value of 1, as expected for a product state of all spins down, and subsequently oscillates around zero without returning to its initial configuration. These features reflect the loss of memory of the initial state and support the interpretation of $|0\rangle$ as a thermal benchmark.

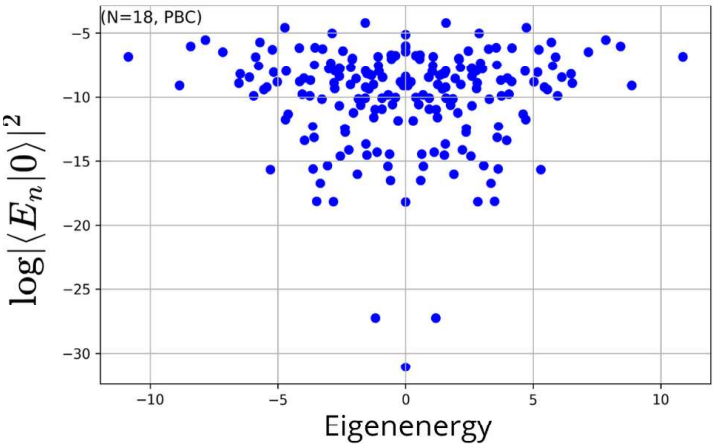

Figura 16 – Spectral overlap of the initial state $|0\rangle$ with the eigenstates of the PXP model with $L = 18$ sites. The broad distribution of overlap values indicates a strong mixing of the initial state with many eigenstates, consistent with the thermal behavior of the system.

This thermal behavior is further confirmed by the spectral properties shown in Fig. 16, where the overlaps between $|0\rangle$ and the energy eigenstates are broadly distributed throughout the spectrum. Unlike scarred states, no concentration of weight on special eigenstates is observed. This delocalized overlap structure signals strong hybridization with many eigenstates, which is a hallmark of thermalization in isolated quantum systems.

The clear contrast between the thermal dynamics of $|0\rangle$ and the atypical behavior observed for scarred states like $|\mathbb{Z}_2\rangle$ and $|\mathbb{Z}_3\rangle$, discussed in the next sections, provides a useful reference point for identifying and interpreting signatures of weak ergodicity breaking in the PXP model.

States $|\mathbb{Z}_2\rangle$

Figures 17a and 17b show the time evolution of the fidelity $F(t)$ and the nearest-neighbor correlation $C(t)$, respectively, for the initial states $|\mathbb{Z}_2\rangle$, $|\mathbb{Z}_2^{\uparrow}\rangle$, and $|\mathbb{Z}_2^{\downarrow}\rangle$ (defined in Section 3.1, see Eqs. 3.1 and 3.2). Surprisingly, despite breaking the blockade constraint, $|\mathbb{Z}_2^{\uparrow}\rangle$ maintains a higher fidelity over time compared to $|\mathbb{Z}_2^{\downarrow}\rangle$. This unexpected behavior is a consequence of a local freezing effect, illustrated in Figure 18.

The up-flip defect introduces three consecutive up spins ($\uparrow\uparrow\uparrow$) in the chain. This configuration effectively blocks further spin flips in the adjacent sites due to the Rydberg blockade, forming a local region that remains static during the time evolution. This frozen region prevents the dynamics from fully exploring the Hilbert space, thereby preserving the fidelity of the initial state despite being outside the constrained subspace.

In contrast, $|\mathbb{Z}_2^{\downarrow}\rangle$, while remaining within the constrained subspace, allows the

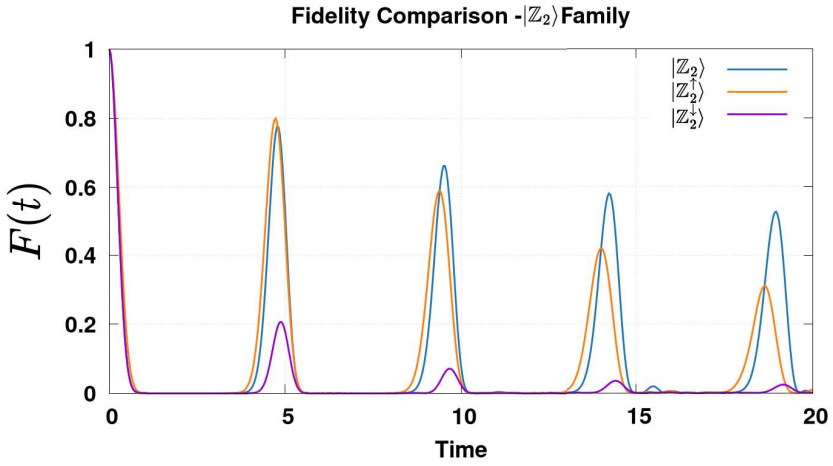

(a)

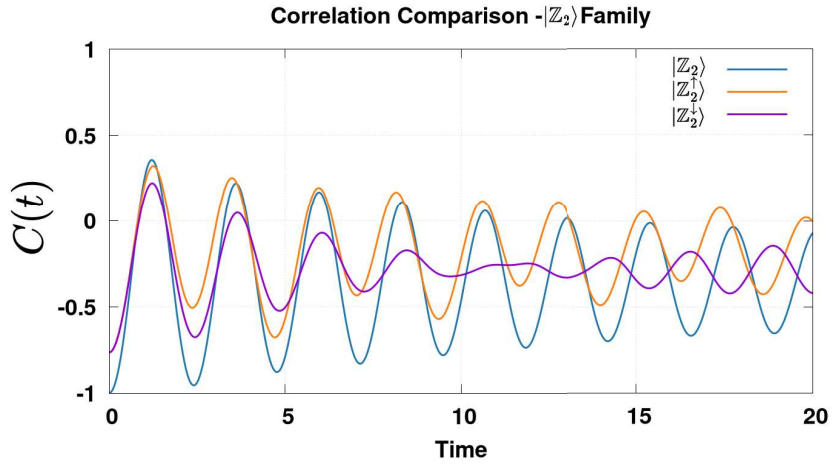

(b)

Figura 17 – (a) Time evolution of the fidelity $F(t)$ and (b) nearest-neighbor correlation $C(t)$ for the initial states $|\mathbb{Z}_2\rangle$ (blue), $|\mathbb{Z}_2^{\uparrow}\rangle$ (orange), and $|\mathbb{Z}_2^{\downarrow}\rangle$ (purple) in the PXP model with $L = 18$ sites. The up-flip defect shows a slower fidelity decay than the down-flip defect, consistent with the formation of a frozen region (see Fig. 18).

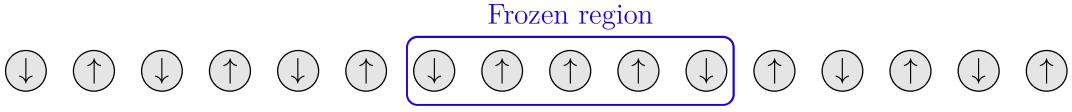

Figura 18 – Schematic illustration of a frozen region generated by the up-flip defect $|\mathbb{Z}_2^{\uparrow}\rangle$. The three consecutive up spins and their neighboring down spins remain static during the time evolution due to the blockade constraint, forming an extended frozen region.

dynamics to spread more freely throughout the system. The fidelity decays more rapidly than in the $|\mathbb{Z}_2^{\uparrow}\rangle$ case, indicating a stronger mixing with thermal states. The correlation function $C(t)$ for $|\mathbb{Z}_2^{\downarrow}\rangle$ shows a less regular pattern: initial oscillations are disrupted by irregularities that break the revival structure, although some oscillations persist at later times.

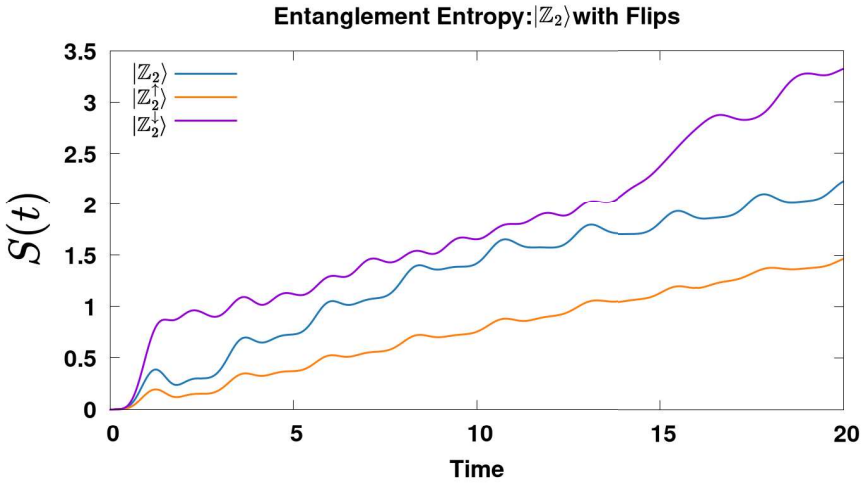

Figura 19 – Time evolution of the bipartite entanglement entropy $S(t)$ for the initial states $|\mathbb{Z}_2\rangle$ (blue), $|\mathbb{Z}_2^{\uparrow}\rangle$ (orange), and $|\mathbb{Z}_2^{\downarrow}\rangle$ (purple) in the PXP model with $L = 18$ sites. The down-flip defect exhibits a faster increase in entanglement, reflecting a stronger tendency toward thermalization, whereas the up-flip defect shows a slower entropy growth due to the formation of a partially frozen region. The unperturbed $|\mathbb{Z}_2\rangle$ state shows intermediate behavior between these two cases.

Figure 19 presents the time evolution of the bipartite entanglement entropy $S(t)$ for these initial states. Consistent with the previous results, the $|\mathbb{Z}_2^{\downarrow}\rangle$ state exhibits the fastest entropy growth, approaching the thermal regime more quickly. The ideal state $|\mathbb{Z}_2\rangle$ shows a moderate growth rate, while the $|\mathbb{Z}_2^{\uparrow}\rangle$ state displays a significantly slower increase of entanglement due to the local freezing effect. This highlights how small perturbations in the initial state can substantially influence the entanglement dynamics and, consequently, the stability of quantum scars.

To further probe the differences in the dynamical structure of these states, we analyze the spectral overlap of the initial state with the system's eigenstates. As shown in Figure 20, the overlap spectrum for $|\mathbb{Z}_2\rangle$ reveals a small number of scarred eigenstates that are clearly separated and well-structured. In contrast, the overlap spectrum for $|\mathbb{Z}_2^{\downarrow}\rangle$ is more distributed across a larger number of eigenstates, indicating stronger hybridization with thermal modes. This broader distribution dilutes the scar signatures and correlates with the more rapid decay of fidelity observed in the time evolution.

Since the initial state $|\mathbb{Z}_2^{\uparrow}\rangle$ breaks the blockade constraint, it lies outside the constrained subspace of the PXP model. As a result, its spectral decomposition would include a large number of states from the unconstrained Hilbert space, making a direct

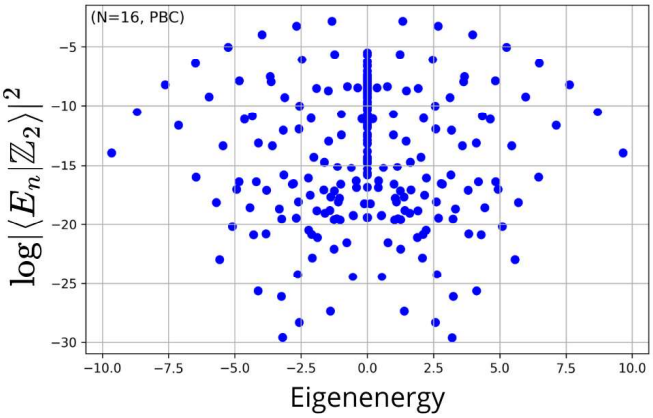

(a)

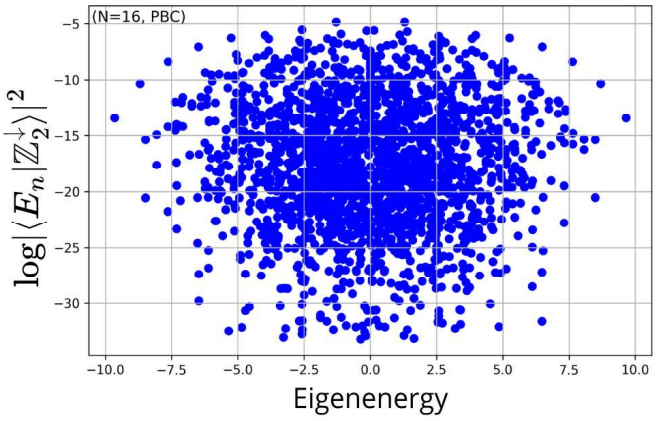

(b)

Figura 20 – (a) Spectral overlap for the initial state $|\mathbb{Z}_2\rangle$ and (b) for $|\mathbb{Z}_2^{\downarrow}\rangle$, computed for the PXP model with $L = 16$ sites. The state $|\mathbb{Z}_2\rangle$ displays a small number of scarred eigenstates that are clearly separated and well structured, whereas $|\mathbb{Z}_2^{\downarrow}\rangle$ shows a broader distribution of overlap across many eigenstates, indicating stronger hybridization with thermal modes.

comparison with the scarred eigenstates of the PXP model less meaningful. Therefore, we focus our spectral overlap analysis on the states that remain within the constrained subspace, namely $|\mathbb{Z}_2\rangle$ and $|\mathbb{Z}_2^{\downarrow}\rangle$.

It is also important to mention that the spectral overlap calculations presented here were performed for chains with $L = 16$ sites due to computational limitations. Nonetheless, the qualitative behavior of the overlap structure and the conclusions drawn from it remain the same for larger chains.

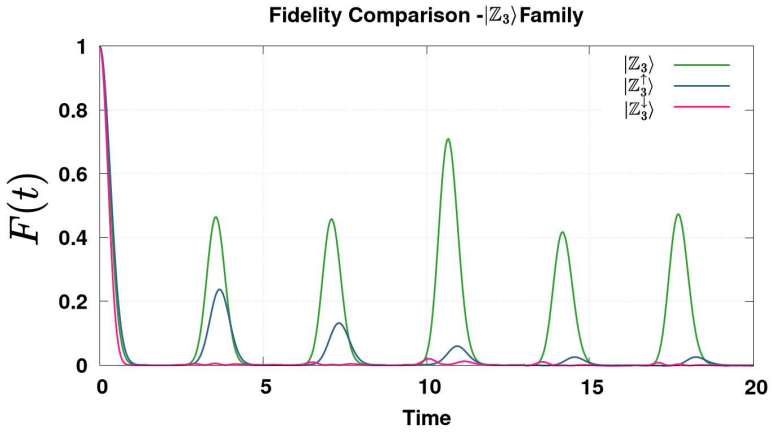

(a)

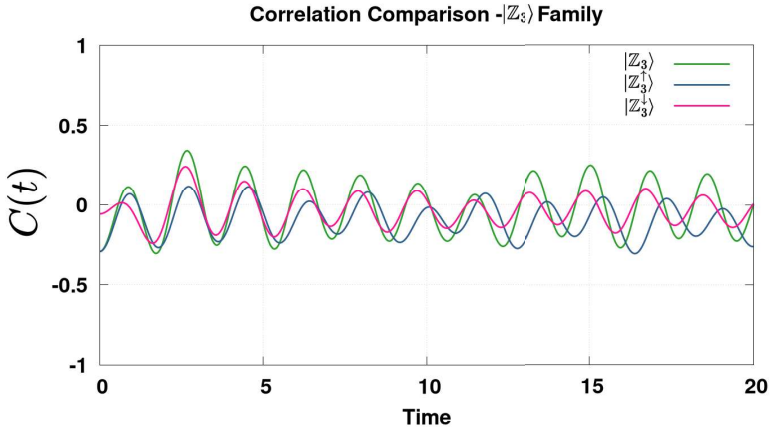

(b)

Figura 21 – (a) Time evolution of the fidelity $F(t)$ and (b) nearest-neighbor correlation $C(t)$ for the initial states $|\mathbb{Z}_3\rangle$ (green), $|\mathbb{Z}_3^{\uparrow}\rangle$ (blue), and $|\mathbb{Z}_3^{\downarrow}\rangle$ (pink) in the PXP model with $L = 18$ sites.

States $|\mathbb{Z}_3\rangle$

Figures 21a and 21b show the time evolution of the fidelity $F(t)$ and the nearest-neighbor correlation $C(t)$ for the initial states $|\mathbb{Z}_3\rangle$, $|\mathbb{Z}_3^{\uparrow}\rangle$, and $|\mathbb{Z}_3^{\downarrow}\rangle$. The state $|\mathbb{Z}_3^{\uparrow}\rangle$ is obtained by flipping a down spin to up near the center of the chain, while $|\mathbb{Z}_3^{\downarrow}\rangle$ results from flipping an up spin to down — both constructed analogously to the $\mathbb{Z}_2$ case discussed in Section 3.1. For the ideal $|\mathbb{Z}_3\rangle$ state, the fidelity shows a prominent revival peak after two smaller peaks, suggesting an initial interference with other states before the dominant revival emerges.

The delayed revival observed for the state $|\mathbb{Z}_3\rangle$, in contrast with the faster revival of $|\mathbb{Z}_2\rangle$, can be partially understood by analyzing the structure of the connectivity graph generated by the PXP constraints, shown in Figures 22a and 22b. The state $|\mathbb{Z}_2\rangle$ is directly connected to three other configurations by such allowed transitions. In contrast, $|\mathbb{Z}_3\rangle$ has only two direct neighbors. This difference in immediate connectivity implies that $|\mathbb{Z}_2\rangle$

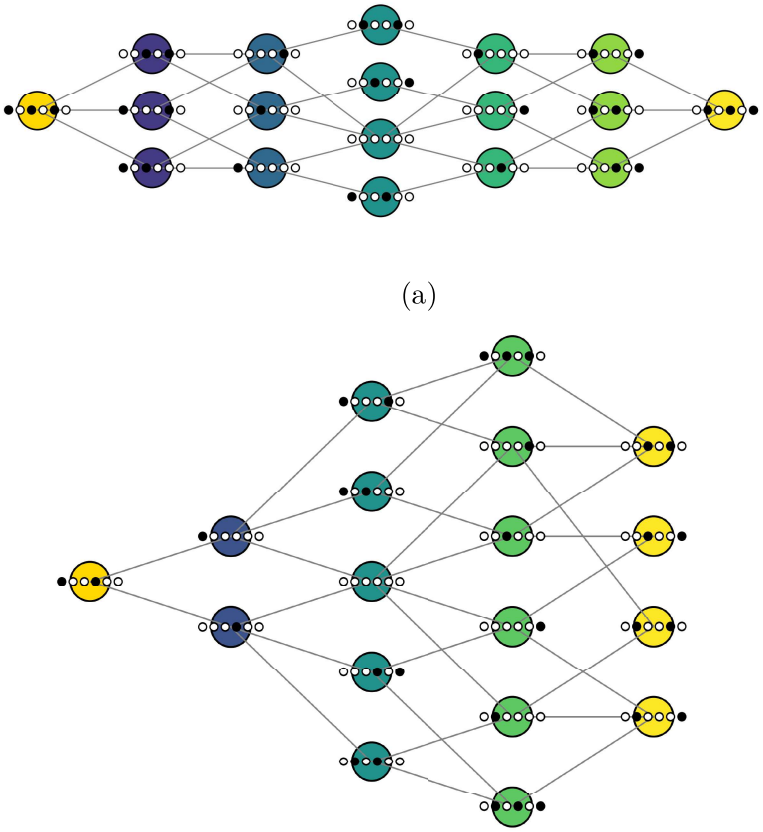

(a)

(b)

Figura 22 – (a) Connectivity graph starting from $|\mathbb{Z}_2\rangle$ and (b) from $|\mathbb{Z}_3\rangle$ for the PXP model with $L = 6$ sites and periodic boundary conditions. Each node represents a basis state of the constrained Hilbert space, and edges correspond to allowed transitions under the PXP Hamiltonian (Hamming distance one and satisfying blockade constraints). The two graphs illustrate the sets of states that are dynamically reachable from each initial configuration under the PXP dynamics.

has more return pathways via short loops in the connectivity graph. These short cycles allow faster and more efficient constructive interference, which contributes to the earlier appearance of revival peaks in the fidelity.

For $|\mathbb{Z}_3\rangle$, the fewer immediate neighbors result in fewer short paths returning to the original state, requiring the system to explore longer sequences of transitions before interference reconstructs the initial configuration, leading to a delayed revival.

For the defected states, both $|\mathbb{Z}_3^{\uparrow}\rangle$ and $|\mathbb{Z}_3^{\downarrow}\rangle$ exhibit faster thermalization compared to the pure $|\mathbb{Z}_3\rangle$ state, as evidenced by the more rapid fidelity decay. The $|\mathbb{Z}_3^{\downarrow}\rangle$ state thermalizes faster than $|\mathbb{Z}_3^{\uparrow}\rangle$, consistent with previous observations for the $\mathbb{Z}_2$ cases. However, this distinction is more evident in the fidelity than in the correlation function, which does not show a clear separation between these cases.

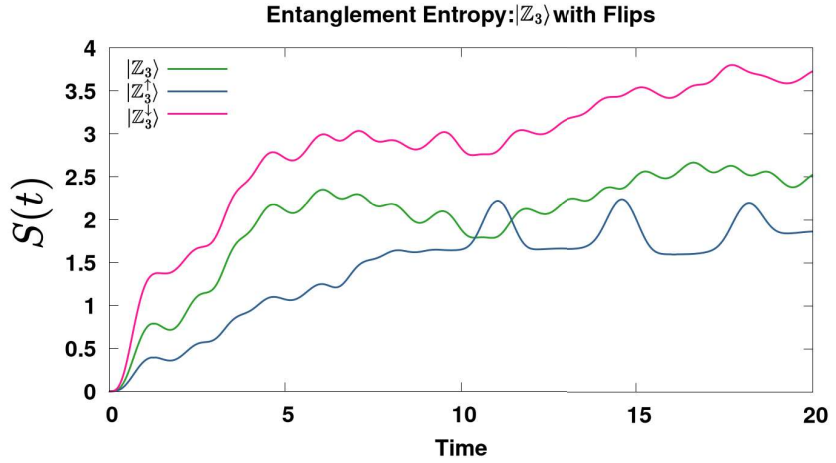

Figura 23 – Time evolution of the bipartite entanglement entropy $S(t)$ for the initial states $|\mathbb{Z}_3\rangle$ (green), $|\mathbb{Z}_3^{\uparrow}\rangle$ (blue), and $|\mathbb{Z}_3^{\downarrow}\rangle$ (pink) in the PXP model with $L = 18$ sites. The down-flip defect leads to a faster increase in entanglement, indicating a stronger tendency toward thermalization, while the up-flip defect exhibits a slower growth due to the formation of a partially frozen region. The unperturbed $|\mathbb{Z}_3\rangle$ state shows intermediate behavior between these two cases.

Figure 23 presents the time evolution of the bipartite entanglement entropy $S(t)$ for the same initial states. Interestingly, the $|\mathbb{Z}_3^{\uparrow}\rangle$ state grows somewhat more slowly than the pure $|\mathbb{Z}_3\rangle$ state but shows small oscillations at later times, indicating partial localization due to a local freezing effect. In contrast, the $|\mathbb{Z}_3^{\downarrow}\rangle$ state shows a faster growth of entropy, as expected for a state that remains in the constrained subspace but is more susceptible to thermal mixing.

The local freezing effect for $|\mathbb{Z}_3^{\uparrow}\rangle$ arises from the presence of two consecutive up spins, which together with their immediate neighbors form a frozen region of four spins. Unlike the $|\mathbb{Z}_2^{\uparrow}\rangle$ case, which freezes five spins, the smaller frozen region in the $|\mathbb{Z}_3^{\uparrow}\rangle$ state allows for some limited dynamics around the defect, contributing to the small oscillations observed in the entanglement growth.

To further investigate the structure of the scarred dynamics, we analyze the spectral overlap of these states with the system's eigenstates. As shown in Figure 24, the overlap spectrum for $|\mathbb{Z}_3\rangle$ reveals the presence of scarred eigenstates, but with a less regular and less uniform spacing compared to the $|\mathbb{Z}_2\rangle$ case. This irregularity likely arises from the odd system size ($L = 15$) and the more complex arrangement of the $|\mathbb{Z}_3\rangle$ pattern in the chain, which prevents the straightforward reflection symmetry present in the $|\mathbb{Z}_2\rangle$ case and makes the sequence of scarred states less symmetric.

Despite this less regular structure, the signature of the scarred eigenstates in the overlap spectrum of $|\mathbb{Z}_3\rangle$ remains clearly identifiable. In particular, we observe approximately 10 states with relatively regular spacing that resemble the expected scarred structure, along with about 5 additional states that appear close to these scars, showing

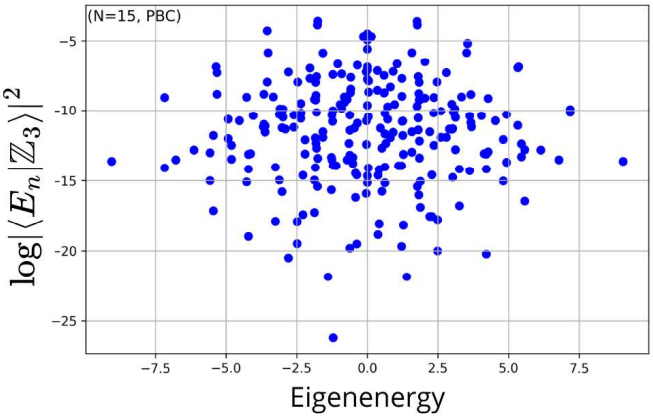

(a)

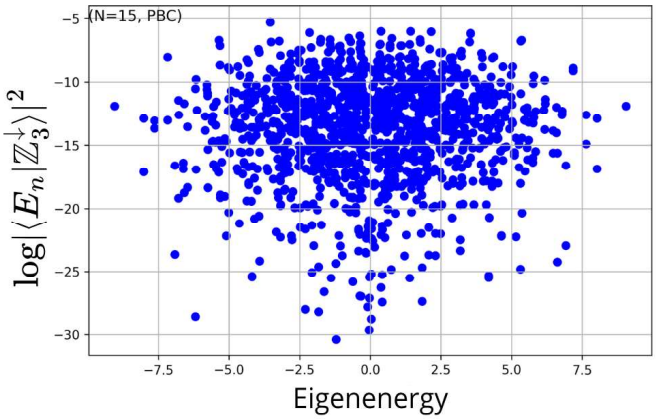

(b)

Figura 24 – (a) Spectral overlap for the initial state $|\mathbb{Z}_3\rangle$ and (b) for $|\mathbb{Z}_3^{\downarrow}\rangle$, computed for the PXP model with $L = 15$ sites. For $|\mathbb{Z}_3\rangle$, a few eigenstates with relatively large overlap remain distinguishable and approximately equally spaced in energy, indicating remnants of scarred structure. In contrast, $|\mathbb{Z}_3^{\downarrow}\rangle$ exhibits a much broader distribution of overlap over many eigenstates, showing stronger hybridization with the thermal bulk.

significant overlap. There is also a denser background of nearby states makes the structure less isolated than in the $|\mathbb{Z}_2\rangle$ case, where the scarred eigenstates stand out as distinct and well-separated peaks with overlaps much larger than the surrounding states.

In contrast, the overlap spectrum for $|\mathbb{Z}_3^{\downarrow}\rangle$ shows a much more distributed structure, with significant mixing with thermal modes, similar to the behavior observed in the $|\mathbb{Z}_2^{\downarrow}\rangle$ case. This broad distribution of overlap values indicates a strong hybridization of the initial state with many eigenstates across the spectrum, diluting the signature of the scars and leading to faster relaxation toward the thermal regime. The lack of well-defined peaks makes it more challenging to identify individual scarred eigenstates, which is consistent with the more rapid decay of fidelity observed in the time evolution. This result reinforces

the sensitivity of scarred dynamics to local perturbations in the initial state and highlights the fragile nature of scars under small modifications that respect the blockade constraint.

Like $|\mathbb{Z}_2^{\uparrow}\rangle$, the initial state $|\mathbb{Z}_3^{\uparrow}\rangle$ breaks the blockade constraint and lies outside the constrained subspace of the PXP model. As a result, its spectral decomposition would include states from the unconstrained Hilbert space, making a direct comparison with scarred eigenstates less meaningful.

It is important to mention that the spectral overlap calculations for the $\mathbb{Z}_3$ cases were performed for $L = 15$ sites to ensure that the $|\mathbb{Z}_3\rangle$ state tiles the chain perfectly under periodic boundary conditions, preserving the translational symmetry of the state. Additionally, computational limitations restrict the system size that can be diagonalized. Despite this, the qualitative conclusions drawn from the overlap analysis remain valid and consistent with the results obtained from larger chains in other analyses.

Overall, these results underscore the sensitivity of scarred dynamics to even small local perturbations of the initial state. Small defects, while seemingly minor, can significantly accelerate the decay of fidelity, alter the entanglement growth, and dilute the signature of scars in the spectral overlap. This highlights the delicate balance required to sustain nonthermal behavior in the PXP model. In the next section, we extend this analysis to perturbations directly in the Hamiltonian—beginning with the Schrieffer-Wolff corrections—to further probe the robustness of scars against more fundamental modifications of the model itself.

4.2.2 Schrieffer-Wolff Perturbations

Having examined the stability of scars under local defects in the initial state, we now turn our attention to perturbations directly in the Hamiltonian. We begin with the Schrieffer-Wolff (SW) correction, a second-order perturbative term derived from the Rydberg model that captures virtual transitions outside the constrained subspace. Our goal is to compare the dynamics under the Rydberg, PXP, and PXP+SW Hamiltonians to assess whether the inclusion of SW corrections significantly modifies the scarred dynamics observed in the pure PXP model.

Figures 25a and 25b show the time evolution of the fidelity $F(t)$ and the nearest-neighbor correlation $C(t)$ for the initial state $|\mathbb{Z}_2\rangle$ under the Rydberg, PXP, and PXP+SW Hamiltonians. The results exhibit a remarkable agreement among the three models, with only minor differences that are nearly indistinguishable at the scale of the plots.

This behavior can be understood in terms of the effective blockade constraint inherent to the Rydberg chain. The PXP model captures the leading-order dynamics by projecting the Rydberg Hamiltonian onto the constrained subspace, where no two adjacent spins can be simultaneously excited. The Schrieffer-Wolff correction introduces second-

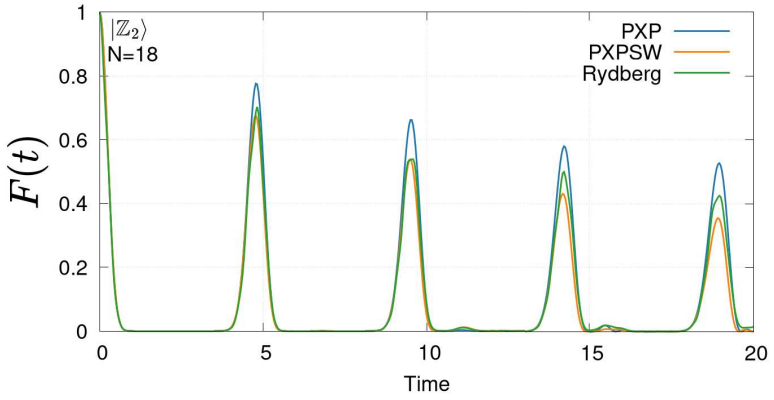

(a)

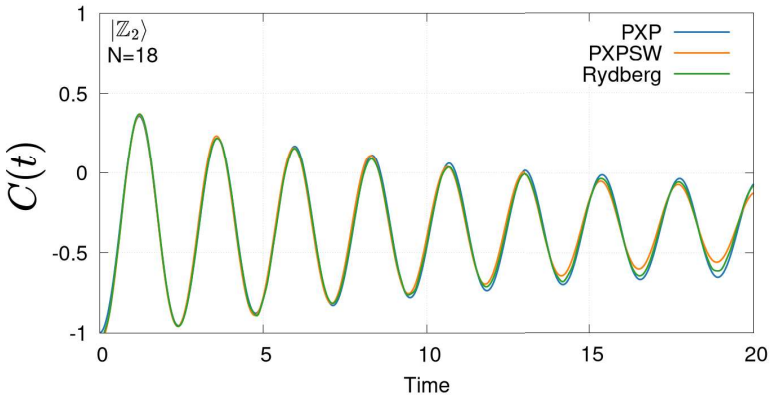

(b)

Figura 25 – (a) Time evolution of the fidelity $F(t)$ and (b) nearest-neighbor correlation $C(t)$ for the initial state $|\mathbb{Z}_2\rangle$ under the Rydberg, PXP, and PXP+SW Hamiltonians for a chain of $L = 18$ sites. The PXP model captures the main oscillatory dynamics observed experimentally, while the full Rydberg Hamiltonian introduces small deviations due to longer-range interactions. Including the Schrieffer–Wolff (SW) corrections in the PXP+SW Hamiltonian improves the agreement with the Rydberg dynamics and extends the lifetime of coherent oscillations.

order processes that account for virtual transitions outside the subspace, but projects their effects back into the constrained subspace as effective interactions. However, in the regime of strong blockade (large detuning), these virtual processes are highly suppressed, and their contribution to the dynamics is subleading. Consequently, the essential features of the scarred dynamics—such as the periodic revivals and slow growth of entanglement—are already well captured by the PXP model alone.

The robustness of the scarred dynamics against the inclusion of SW corrections underscores the emergent nature of these nonthermal states. Although the SW term introduces additional effective interactions in the constrained subspace, these corrections

do not qualitatively affect the scarring phenomenon within the time window considered. This finding validates the use of the PXP model as a minimal and effective framework to capture the essential physics of scars, without the need to incorporate higher-order corrections that only slightly perturb the dynamics. Therefore, in the following sections, we focus on the PXP model itself when analyzing the impact of further perturbations in the Hamiltonian. This allows us to isolate the key mechanisms underlying the stability and fragility of scars under more general modifications.

4.2.3 Hamiltonian Perturbations

Having discussed the stability of scars under Schrieffer-Wolff perturbations, we now turn to more general perturbations in the Hamiltonian, focusing on both projected and non-projected cases, with and without disorder. These perturbations, defined in Eqs. (3.6) and (3.7) in the previous chapter, include site-dependent local fields in the X, Y, and Z directions, either applied uniformly across all sites or drawn randomly within the range $[-W/2, W/2]$.

We analyze the impact of these perturbations on the scarred dynamics by examining the time evolution of the fidelity and the nearest-neighbor correlation for each case. Additionally, for the projected perturbation with disorder, we compute the entanglement entropy of the eigenstates to explore possible signatures of thermalization. The following subsections detail these results and highlight the key differences between projected and non-projected perturbations, as well as the role of disorder.

Projected Perturbations without Disorder

We begin by analyzing the effect of projected perturbations in the Hamiltonian without disorder. In this case, the local fields h_X^i, h_Y^i, and h_Z^i are uniform across all sites, preserving translational invariance and ensuring that all spins experience the same perturbation. The use of projection operators in the perturbation preserves the blockade constraint at each site, thereby maintaining the structure of the constrained subspace where scars emerge.

Figures 26a and 26b show the time evolution of the fidelity $F(t)$ and the nearest-neighbor correlation $C(t)$ for the initial state $|\mathbb{Z}_2\rangle$ under projected perturbations without disorder. The fidelity displays robust oscillations with well-defined revivals, similar to the unperturbed PXP case, although with a slightly reduced amplitude. The correlation function $C(t)$ also preserves its characteristic oscillations, indicating that the essential features of the scarred dynamics remain largely unaffected.

This behavior highlights the resilience of the scars under projected perturbations that preserve the blockade constraint and maintain the system within the constrained

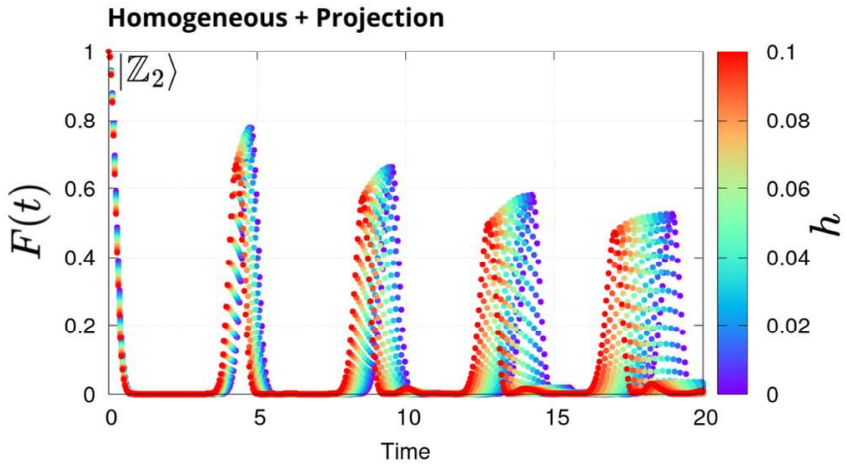

(a)

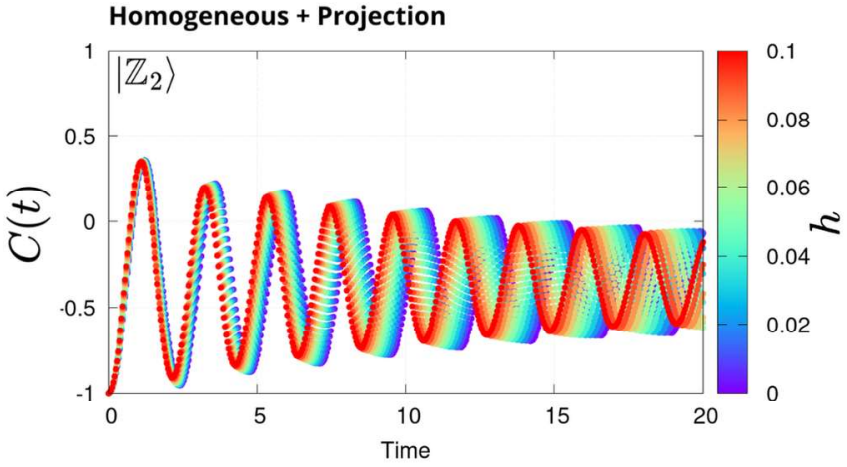

(b)

Figura 26 – (a) Time evolution of the fidelity $F(t)$ and (b) nearest-neighbor correlation $C(t)$ for the initial state $|\mathbb{Z}_2\rangle$ in the PXP model with $L = 18$ sites under projected perturbations without disorder. Both observables exhibit long-lived oscillations, indicating that the projected homogeneous perturbation preserves much of the coherent scarred dynamics observed in the unperturbed model.

subspace. The uniform nature of the perturbations ensures that no additional local randomness is introduced, which might otherwise disrupt the coherent structure of the scarred states. Overall, these results indicate that the nonthermal scarred dynamics is stable against homogeneous projected perturbations, reinforcing the picture that the scars emerge from the effective $\mathfrak{su}(2)$ structure inherent in the constrained subspace dynamics.

An additional feature observed in Figures 26a and 26b is a slight shift of the oscillations toward earlier times compared to the unperturbed PXP model. This shift suggests that the projected perturbation effectively modifies the timescale of the dynamics, leading to a faster oscillation frequency. Physically, this can be interpreted as a small renormalization of the effective interactions in the constrained subspace, which accelerates

the underlying $\mathfrak{su}(2)$-like precession responsible for the revivals.

Interestingly, despite this shift, the fidelity and correlation maintain their characteristic oscillations with only minor changes. This reinforces the interpretation that the nonthermal scarred dynamics is deeply rooted in the effective $\mathfrak{su}(2)$ structure inherent in the constrained subspace dynamics.

Non-Projected Perturbations without Disorder

We now analyze the effect of non-projected perturbations in the Hamiltonian without disorder. In this scenario, the local fields h_X^i, h_Y^i, and h_Z^i are uniform across all sites, but unlike the projected case, they are applied directly to the spin operators without the blockade projection. This allows transitions that break the blockade constraint and move the dynamics outside the constrained subspace.

Figures 27a and 27b show the time evolution of the fidelity $F(t)$ and the nearest-neighbor correlation $C(t)$ for the initial state $|\mathbb{Z}_2\rangle$ under non-projected perturbations without disorder. Compared to the projected case, the fidelity exhibits a significantly faster decay of the revival amplitudes, although they remain clearly visible. This faster decay can be attributed to the fact that the non-projected perturbation allows transitions outside the constrained subspace, effectively coupling the scarred dynamics to a larger set of configurations that do not support revivals. As a result, part of the probability amplitude leaks into states that do not contribute constructively to the scars, leading to a damping of the fidelity oscillations.

The nearest-neighbor correlation also shows a reduction in amplitude compared to the unperturbed case, though this reduction is relatively modest. The oscillatory structure of $C(t)$ remains consistent with the scarred dynamics, indicating that the local spin alignment is more robust against the non-projected perturbations than the global fidelity. Nevertheless, a comparison with the unperturbed model shows that even the local observables are affected by the perturbation, highlighting the subtle interplay between local and global signatures of the scars.

These results illustrate how the absence of projection in the perturbation increases the fragility of the scarred dynamics, even in the absence of disorder. They highlight the crucial role of the blockade constraint in stabilizing the scars by restricting the system to the effective $\mathfrak{su}(2)$ subspace that supports coherent revivals.

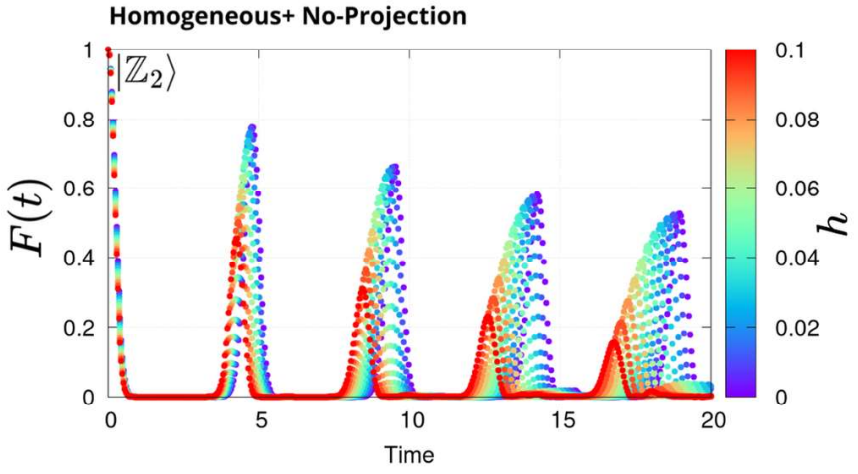

(a)

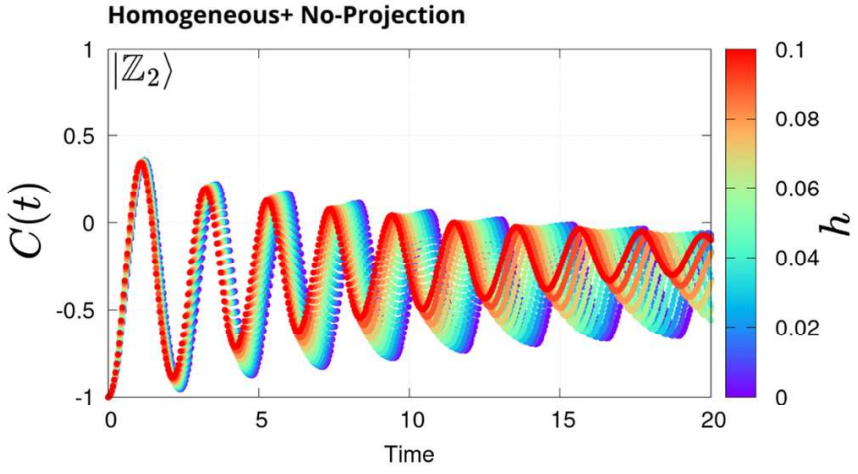

(b)

Figura 27 – (a) Time evolution of the fidelity $F(t)$ and (b) nearest-neighbor correlation $C(t)$ for the initial state $|\mathbb{Z}_2\rangle$ in the PXP model with $L = 18$ sites under non-projected perturbations without disorder. In this case, both observables show a faster decay of oscillations compared to the projected perturbation, indicating that the inclusion of off-manifold couplings leads to stronger thermalization and loss of coherence.

Projected Perturbations with Disorder

We now analyze the effect of projected perturbations in the Hamiltonian with disorder. In this case, the local fields h_X^i, h_Y^i, and h_Z^i are drawn randomly from the range $[-W/2, W/2]$ at each site, introducing local inhomogeneities while preserving the blockade constraint through the projection operators.

Figures 28a and 28b show the time evolution of the fidelity $F(t)$ and the nearest-neighbor correlation $C(t)$ for the initial state $|\mathbb{Z}_2\rangle$ under projected perturbations with disorder. Comparing with the homogeneous projected perturbations (without disorder), we observe that the main difference is a gradual decay in the amplitude of the revivals.

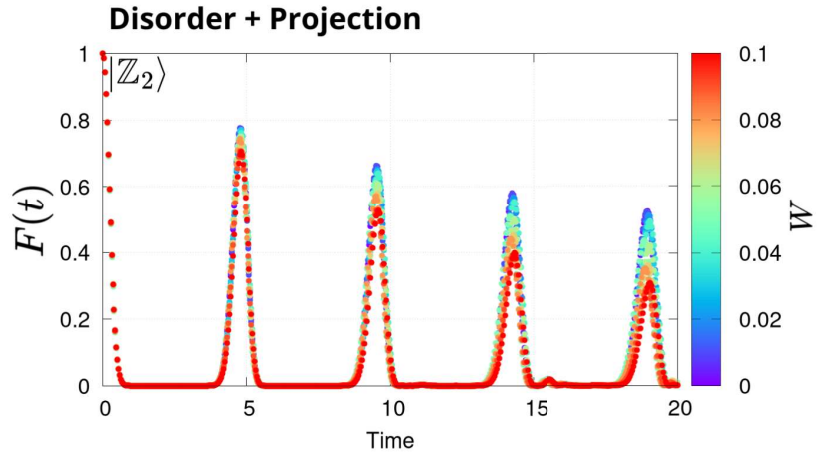

(a)

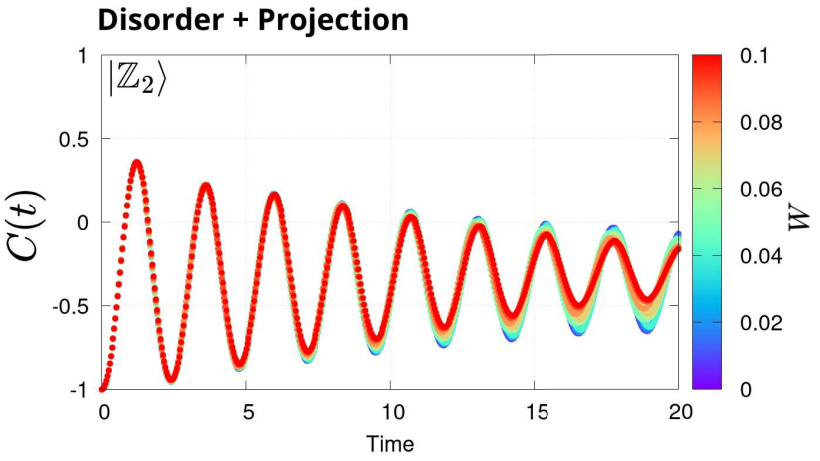

(b)

Figura 28 – (a) Time evolution of the fidelity $F(t)$ and (b) nearest-neighbor correlation $C(t)$ for the initial state $|\mathbb{Z}_2\rangle$ in the PXP model with $L = 18$ sites under projected perturbations with disorder. The introduction of disorder leads to a suppression of coherent revivals and to a faster decay of correlations, showing that even weak disorder disrupts the regular structure of the scarred dynamics.

This decay can be attributed to local dephasing effects introduced by the random fields, which slightly detune the effective precession frequencies in different parts of the chain. Interestingly, the peak positions remain closely aligned with those of the unperturbed dynamics, indicating that the global $\mathfrak{su}(2)$ structure is not significantly renormalized by the disorder—only its coherence is progressively reduced.

The correlation function exhibits a similar trend: the characteristic oscillations are preserved, but their amplitude decays slightly more noticeably than in the homogeneous case. This highlights the subtle interplay between local disorder and the blockade constraint: while the projection prevents transitions outside the constrained subspace (thus maintaining the essential scar structure), the disorder introduces small phase shifts between different regions of the chain, leading to a gradual loss of coherence and damping of the oscillations.

Overall, this scenario demonstrates that the presence of disorder within the projected subspace erodes the coherence of scarred dynamics without destroying its fundamental structure. The blockade constraint remains crucial for preserving the nonthermal features associated with the scars, even under the influence of local disorder.

Non-Projected Perturbations with Disorder

Finally, we analyze the effect of non-projected perturbations in the Hamiltonian with disorder. Here, the local fields h_X^i, h_Y^i, and h_Z^i are drawn randomly from the range $[-W/2, W/2]$ at each site, and unlike the projected case, these terms are applied directly to the spin operators without the blockade projection. This allows transitions that break the blockade constraint and enables the dynamics to escape from the constrained subspace.

Figures 29a and 29b show the time evolution of the fidelity $F(t)$ and the nearest-neighbor correlation $C(t)$ for the initial state $|\mathbb{Z}_2\rangle$ under non-projected perturbations with disorder. Compared to the projected cases, both observables show a slightly more pronounced decay of the oscillation amplitudes, reflecting the increased fragility of the scarred dynamics in the presence of transitions that break the blockade constraint. This behavior is consistent with the leakage of probability into states that do not contribute to the scarred revivals, leading to a rapid loss of coherence and a stronger damping of the revivals.

Moreover, the peak positions of the oscillations do not align perfectly across different disorder realizations. This misalignment arises because the local disorder introduces variations in the effective precession frequencies at each site, and without the projection to enforce the blockade constraint, the system evolves into a broader set of configurations that break the global $\mathfrak{su}(2)$ synchronization. As a result, the revivals become less regular and their phases lose coherence.

To quantify the effect of disorder on the amplitude of the scarred revivals in the non-projected case, we extracted the height of the first revival peak in the fidelity for different values of disorder strength W, averaging over 10 disorder realizations for each W. The resulting dependence of the amplitude on W is shown in Figure 30. While the main fidelity and correlation plots analyzed in this section focus on values of $W \leq 0.1$, where the decay is present but not yet dramatic, the fit extends up to $W = 0.5$ to capture the overall trend in the exponential decay. This shows that even moderate disorder can suppress the scarred revivals significantly, with the decay rate increasing sharply for larger values of W.

This behavior can be interpreted as a manifestation of the *orthogonality catastrophe* [87], in which the overlap between the initial state and the perturbed eigenstates decreases rapidly with increasing disorder strength. In fully thermalizing systems, the

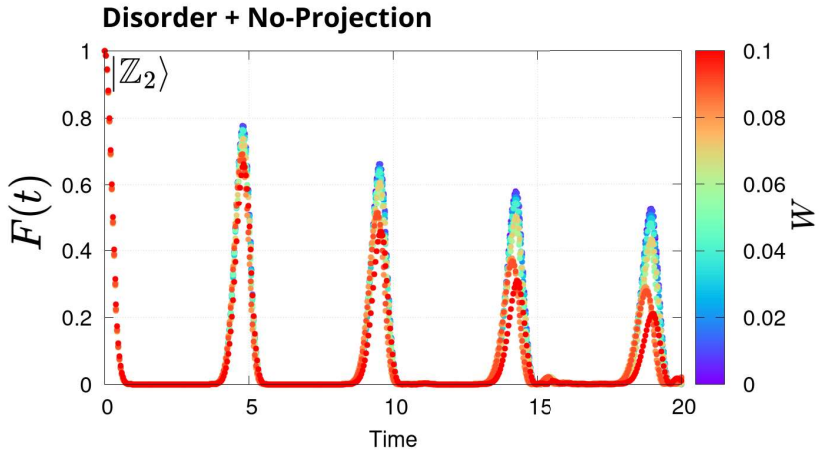

(a)

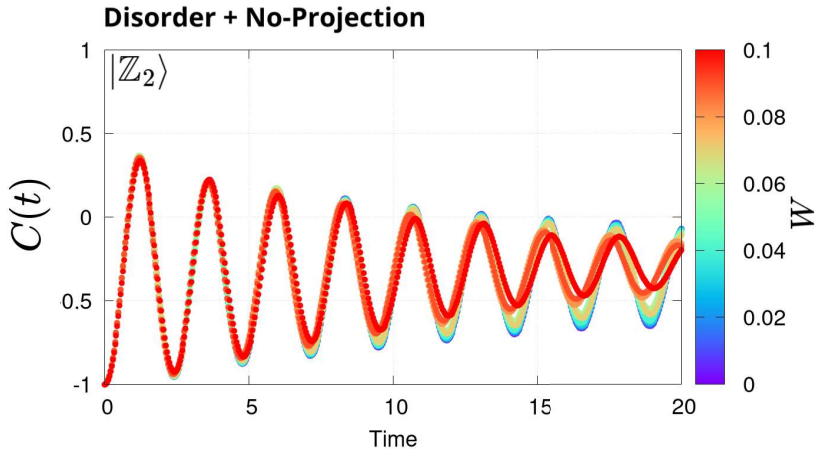

(b)

Figura 29 – (a) Time evolution of the fidelity $F(t)$ and (b) nearest-neighbor correlation $C(t)$ for the initial state $|\mathbb{Z}_2\rangle$ in the PXP model with $L = 18$ sites under non-projected perturbations with disorder. In this case, the combined effect of disorder and unprojected couplings rapidly suppresses revivals and drives the system toward thermal equilibrium, indicating that both ingredients contribute to the breakdown of the scarred dynamics.

fidelity typically decays over time with a Gaussian profile $F(t) \sim \exp[-c(Wt)^2]$, where c is a constant [88]. In contrast, many-body scars are known to generate deviations from this behavior, exhibiting periodic revivals and sustained memory of the initial state, thereby reflecting their non-ergodic nature. However, in the presence of disorder in the non-projected case, the decay of the fidelity peak amplitude as a function of disorder strength recovers a Gaussian-like dependence, signaling the onset of ergodic behavior induced by the perturbation. This highlights the fragile nature of the scars when the blockade constraint is lifted, emphasizing the critical role of the constraint in stabilizing non-thermal dynamics.

These results reveal that while the blockade constraint is traditionally considered

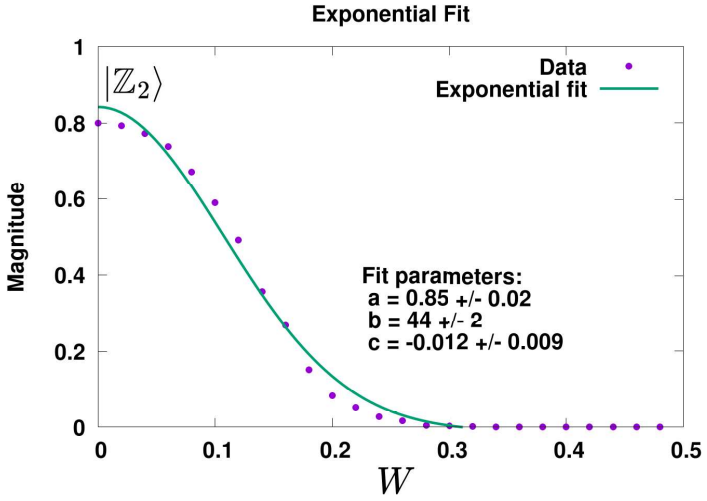

Figura 30 – Fit of the amplitude of the first revival peak in the fidelity $F(t)$ as a function of disorder strength W in the non-projected case. Each point represents the average over 10 disorder realizations, with the perturbation drawn from $[-W/2, W/2]$ at each site. The fit uses the function $f(W) = a\, e^{-bW^2} + c$, with the fitted values of a, b, and c displayed in the plot.

essential for stabilizing scars, its impact may be less decisive in the presence of disorder. Surprisingly, the fidelity revivals remain significant even in the non-projected case, particularly when disorder is included. This suggests that disorder itself — by introducing local variations that average out globally — can effectively reduce the differences between projected and non-projected cases, making both scenarios similarly sensitive to dephasing. In this sense, the role of disorder appears to be more relevant than the role of the projection in determining the decay of the scarred oscillations, highlighting the need for a deeper understanding of how different perturbations interplay with the underlying non-ergodic dynamics.

Scaling with System Size

To assess the robustness of the scarred dynamics concerning system size, we analyze the time evolution of the fidelity $F(t)$ and the nearest-neighbor correlation $C(t)$ for chains of different lengths (L). Figures 31a and 31b show these quantities for the initial state $|\mathbb{Z}_2\rangle$ with periodic boundary conditions.

For $L \geq 8$, both observables display a consistent trend: the fidelity exhibits periodic revivals with amplitudes that decay gradually as the system size increases, while the correlation function shows a similar oscillatory behavior with a less pronounced decay. This pattern indicates that the essential features of the scarred dynamics — namely, the $\mathfrak{su}(2)$-like periodicity and the presence of revivals — persist across different system sizes, even though global coherence diminishes for larger chains due to accumulated phase dispersions within the constrained subspace.

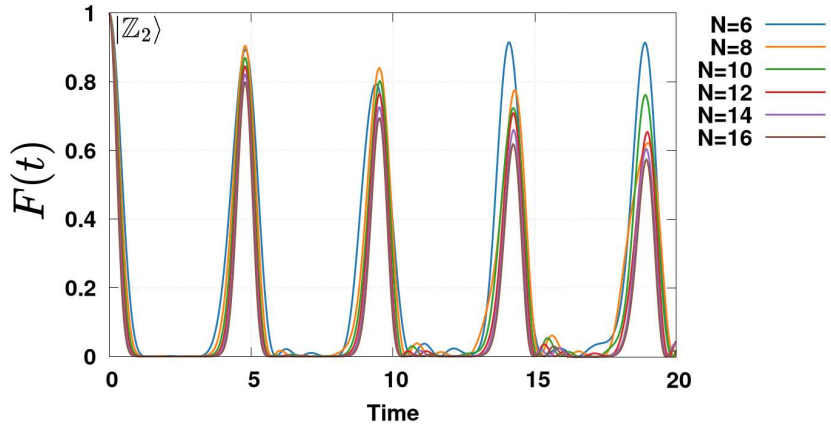

(a)

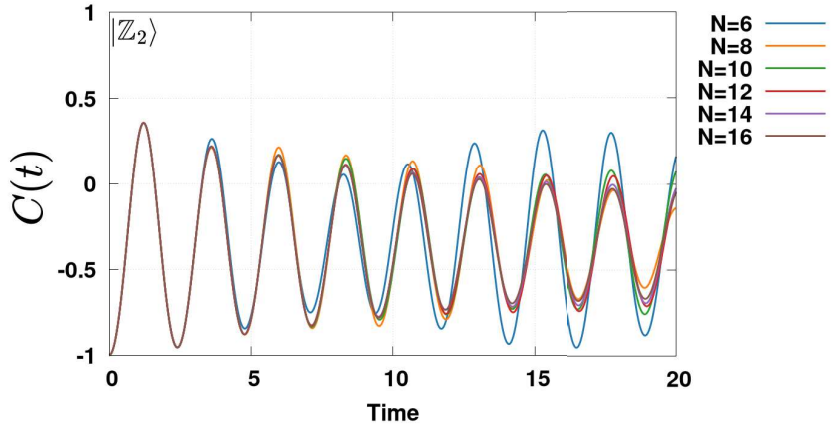

(b)

Figura 31 – (a) Time evolution of the fidelity $F(t)$ and (b) nearest-neighbor correlation $C(t)$ for the initial state $|\mathbb{Z}_2\rangle$ in the PXP model under periodic boundary conditions for different system sizes L. The revival amplitude decreases and the damping rate increases with system size, showing that finite-size effects play an important role in sustaining coherent oscillations in smaller chains.

A particularly illustrative finite-size effect appears for the smallest chain ($L = 6$). Although it also exhibits revivals, its third fidelity peak is anomalously enhanced compared to larger systems. This enhancement is consistent with finite-size recurrences: in very small Hilbert spaces, excitations are reflected more rapidly, artificially boosting the apparent coherence. Such behavior highlights the limitations of very small chains in reliably capturing the decay mechanisms relevant for larger systems.

Taken together, these results support the conclusion that chains of size $L = 18$ — as used in the main sections of this study — are sufficiently large to faithfully capture the essential features of scarred dynamics, while minimizing finite-size artifacts. This conclusion is further reinforced by the use of periodic boundary conditions, which help to

reduce boundary effects that could otherwise distort the dynamics.

Although these finite-size results demonstrate that scarred dynamics remain clearly identifiable for all system sizes accessible to exact diagonalization (up to $L = 18$ in this study), it is important to emphasize that this robustness should not be extrapolated to the thermodynamic limit. The persistence of revivals for moderate chain lengths simply reflects that, within this range, the constrained Hilbert space is still comparatively small and the initial state overlaps strongly with a limited set of nonthermal eigenstates. As L increases, however, the Hilbert space grows exponentially, providing a rapidly expanding set of accessible states into which the initial wavefunction can spread. In this limit, the accumulated phase dispersion and the increased density of thermal states inevitably suppress coherent revivals, even though the nonthermal scarred eigenstates themselves continue to exist as isolated points in the spectrum. Thus, the scaling analysis confirms that scars remain dynamically visible for the system sizes investigated here, while also aligning with the theoretical expectation that revival phenomena do not survive in the thermodynamic limit.

4.3 Comparative Summary

This chapter systematically investigated the impact of different perturbations on the scarred dynamics of the PXP model. We considered various scenarios, including initial state defects, the Schrieffer-Wolff (SW) corrections to the Hamiltonian, and both projected and non-projected perturbations, with and without disorder. We aimed to identify the key factors that influence the stability of the scarred revivals and to understand how these elements interact with the structure of the constrained subspace.

We began by analyzing the effect of local defects in the initial state, showing that even small perturbations can alter the fidelity, correlation functions, and entanglement growth. The $|\mathbb{Z}_2^{\uparrow}\rangle$ state, for example, exhibited slower entanglement growth due to the formation of local frozen regions, while the $|\mathbb{Z}_2^{\downarrow}\rangle$ state showed faster mixing with thermal modes. Nevertheless, revivals in the fidelity were still observed in both cases, highlighting the residual presence of scarred dynamics even in the presence of local defects.

Next, we considered perturbations in the Hamiltonian itself, beginning with the Schrieffer-Wolff correction derived from the Rydberg model. Surprisingly, this correction had minimal impact on the scarred dynamics within the timescales investigated: the fidelity and correlation functions remained nearly identical to those of the pure PXP model. This result underscores the robustness of the PXP approximation and justifies its use as an effective description of the scarred subspace.

For the projected homogeneous perturbations, the blockade constraint preserved the periodic revivals in both fidelity and correlation, with only a slight shift in the revival

frequency - depending on the intensity of the perturbation - due to uniform renormalization of the effective precession frequency. When disorder was introduced in the projected case, the peak positions of the revivals remained aligned, indicating that the local fluctuations averaged out globally and did not induce significant dephasing. Interestingly, a similar behavior was observed in the non-projected case with disorder, where the peak positions also remained well-aligned despite the absence of the blockade constraint. This suggests that, in the presence of disorder, the local randomness can average out globally to preserve the overall coherence of the scarred dynamics, highlighting that the interplay between projection and disorder is more subtle than initially anticipated.

In the non-projected scenarios, homogeneous perturbations allowed transitions outside the constrained subspace, leading to a more rapid decay of the fidelity revivals. Interestingly, the local correlation functions remained relatively robust, reflecting their insensitivity to the global structure of the dynamics. When disorder was introduced, both projected and non-projected cases displayed a similar behavior: the amplitudes of the revivals decayed smoothly, and the differences between the projected and non-projected cases diminished. This suggests that disorder plays a more dominant role in damping the scars than the blockade constraint does.

In summary, our results demonstrate that both the blockade constraint and the presence of disorder significantly shape the stability of the scarred dynamics, but their roles are intricately intertwined. While the blockade constraint restricts the dynamics to the constrained subspace and influences the emergence of the effective $\mathfrak{su}(2)$ structure, the disorder—through its statistical properties—can average out local variations and preserve coherence, even in the absence of projection. The interplay between these factors, along with local defects in the initial state and Hamiltonian perturbations, emerges as a key determinant of the robustness of scars in realistic systems. These insights provide a nuanced understanding of the mechanisms that govern non-ergodic dynamics in constrained quantum systems, offering guidance for future studies exploring the rich interplay between constraints, perturbations, and disorder.

5 Conclusions

This thesis investigated the stability of quantum many-body scars in the PXP model under various perturbations, focusing on local defects in the initial state, Schrieffer-Wolff corrections, and both projected and non-projected perturbations with and without disorder. Through a detailed analysis of fidelity, correlation functions, and entanglement dynamics, we explored how these perturbations interact with the underlying $\mathfrak{su}(2)$ structure that supports the scarred dynamics.

A primary focus of this work was to investigate the stability of scarred dynamics against local defects in the initial state, a scenario of high experimental relevance. We systematically compared two distinct types of single-spin-flip defects: a "down-flip" defect that preserves the Rydberg blockade constraint but disrupts the state's alternating pattern, and an "up-flip" defect that explicitly violates the constraint. Counterintuitively, the constraint-violating up-flip defect led to a more robust preservation of non-thermal signatures. We attribute this to a "local freezing" mechanism, where the resulting configuration of adjacent flipped up atoms kinetically restricts the dynamics in its vicinity, thereby protecting the system from rapid thermalization and suppressing entanglement growth. In stark contrast, by breaking the special initial structure required for scarring, the constraint-preserving down-flip defect allowed the system to explore the constrained Hilbert space more effectively, leading to faster fidelity decay and a stronger mixing with thermal eigenstates. This comparison reveals that the resilience of scars is not merely about respecting global constraints, but is intricately tied to the microscopic nature of imperfections and their ability to either freeze dynamics locally or facilitate exploration of the available phase space.

Furthermore, the robustness of the underlying model was confirmed by analyzing Schrieffer-Wolff corrections. These second-order virtual processes in the Hamiltonian had a minimal impact on the scarred dynamics, thus validating the PXP model as a reliable and effective description within the investigated timescales.

The study of Hamiltonian perturbations, in turn, revealed a nuanced interplay between the blockade constraint and the presence of disorder. In homogeneous systems, the blockade constraint proved to be paramount. Projected perturbations, which respect the constraint, only led to a small renormalization of the revival frequency, leaving the scarred dynamics largely intact. In contrast, non-projected homogeneous perturbations induced a significantly faster decay in fidelity, a direct consequence of the dynamics leaking into the unconstrained Hilbert space where scarred revivals are not supported. The introduction of disorder revealed a more complex picture. While projected disorder led to a gradual

decay of revivals due to local dephasing, the overall scarred structure was preserved by the constraint. Remarkably, when disorder was combined with non-projected perturbations, the distinction between the two scenarios became less pronounced. Our results indicate that in this case, disorder itself becomes the dominant mechanism for decoherence, with its statistical properties playing a more significant role in the decay of revivals than the leakage into the unconstrained subspace.

The validity of these conclusions was reinforced by a system-size scaling analysis, which confirmed that the dynamics observed for $L \geq 8$ are representative of the scarred regime and free from significant finite-size artifacts. This justified the choice of $L = 18$ for most of the analyses, ensuring that finite-size effects did not dominate the conclusions.

The different perturbations analyzed in this work can be grouped according to the specific mechanisms by which they affect scarred dynamics. Initial state defects simulate imperfections in state preparation and reveal how local spin flips—either preserving or violating the blockade constraint—impact the initial overlap with scarred eigenstates and the system's ability to remain confined within the scar-supporting subspace. Schrieffer-Wolff corrections, derived from an expansion of the full Rydberg Hamiltonian, preserve the constrained structure but deform the connectivity of the subspace, potentially modifying the interference pathways responsible for coherent revivals. Disordered perturbations probe the role of spatial inhomogeneity: projected disorder acts within the constrained space and introduces local dephasing, while unprojected disorder breaks the blockade constraint and induces leakage into the full Hilbert space. Each of these perturbation classes thus targets a distinct structural feature of the scarred dynamics—initial state fidelity, subspace connectivity, or spectral coherence—offering a broader perspective on the conditions required for the stability of quantum many-body scars.

In summary, this thesis reveals that the stability of quantum many-body scars is governed by a more subtle interplay than a simple dichotomy between ergodic and non-ergodic regimes. The findings highlight that the blockade constraint and disorder are the key factors shaping the scarred dynamics, but their roles are intricately intertwined. Understanding this delicate balance between uniformity, local randomness, and the underlying kinetic constraints is therefore essential for the control and eventual exploitation of coherent dynamics in complex quantum many-body systems.

Future Directions

While this work provided a systematic investigation of scar stability in the PXP model under periodic boundary conditions, several exciting avenues remain open for exploration. The insights gained here lay the groundwork for new theoretical, numerical, and experimental inquiries.

A crucial next step is to forge a stronger and more quantitative link with experimental platforms. Future work could focus on designing specific experimental protocols to test the theoretical predictions made in this thesis. For instance, one could devise methods to controllably introduce and then distinguish the dynamical signatures of the "up-flip" versus "down-flip" defects. This could also involve proposing experimental protocols to quantitatively measure the leakage of the dynamics outside the constrained Hilbert space, providing a direct probe of the constraint violation and its role in the degradation of quantum coherence.

Moreover, the dynamics explored in this thesis were unitary and time-independent. A promising direction is the inclusion of time-dependent driving fields to investigate whether Floquet engineering can be used to actively stabilize, enhance, or even create new scarred dynamics, particularly in the presence of disorder. In parallel, understanding the robustness of scars in realistic scenarios requires the study of open quantum systems. Investigating the effects of environmental coupling, dissipation, and decoherence is essential to determine how long scar-induced memory can persist in a noisy environment, which is a critical question for any potential technological application.

Finally, extending the analysis to other models and regimes would shed light on the universality of the observed phenomena. This includes exploring higher-dimensional Rydberg arrays or different constrained models like spin ladders. Such studies would benefit from employing numerical methods suitable for larger systems, such as the Density Matrix Renormalization Group (DMRG), to rigorously probe the thermodynamic limit. Within this broader scope, a systematic study of how the stability breaks down as a function of perturbation strength would be valuable. While this work confirmed the robustness of scars against weak perturbations, a future project could focus on mapping the full crossover from the scarred to the thermal regime, thus creating a more complete stability diagram. Together, these avenues of research will not only expand our fundamental understanding of non-ergodic dynamics but also pave the way for the application of quantum many-body scars in quantum technologies.

Referências

[1] Vulpiani, Angelo, Fabio Cecconi e Massimo Cencini: *Chaos: from simple models to complex systems*, volume 17. World Scientific, 2009. Citado 2 vezes nas páginas 11 e 14.

[2] Moore, Calvin C: *Ergodic theorem, ergodic theory, and statistical mechanics*. Proceedings of the National Academy of Sciences, 112(7):1907–1911, 2015. Citado 2 vezes nas páginas 11 e 14.

[3] Gallavotti, Giovanni: *Ergodicity, ensembles, irreversibility in Boltzmann and beyond*. Journal of Statistical Physics, 78:1571–1589, 1995. Citado 2 vezes nas páginas 11 e 14.

[4] Lin, Cheng Ju: *Surviving Quantum Chaos: Weak Thermalization, Prethermalization and Quantum Many-Body Scar States*. Tese de Doutoramento, California Institute of Technology, 2019. Citado 3 vezes nas páginas 11, 14 e 19.

[5] Berry, Michael Victor e Michael Tabor: *Level clustering in the regular spectrum*. Proceedings of the Royal Society of London. A. Mathematical and Physical Sciences, 356(1686):375–394, 1977. Citado 3 vezes nas páginas 11, 15 e 21.

[6] Bohigas, Oriol e Marie Joya Giannoni: *Chaotic motion and random matrix theories*. Em *Mathematical and computational methods in nuclear physics*, páginas 1–99. Springer, 1984. Citado na página 11.

[7] Deutsch, Josh M: *Quantum statistical mechanics in a closed system*. Physical review a, 43(4):2046, 1991. Citado 4 vezes nas páginas 12, 18, 19 e 20.

[8] Rigol, Marcos, Vanja Dunjko e Maxim Olshanii: *Thermalization and its mechanism for generic isolated quantum systems*. Nature, 452(7189):854–858, 2008. Citado 3 vezes nas páginas 12, 18 e 20.

[9] Bernien, Hannes, Sylvain Schwartz, Alexander Keesling, Harry Levine, Ahmed Omran, Hannes Pichler, Soonwon Choi, Alexander S Zibrov, Manuel Endres, Markus Greiner *et al.*: *Probing many-body dynamics on a 51-atom quantum simulator*. Nature, 551(7682):579–584, 2017. Citado 11 vezes nas páginas 12, 22, 24, 29, 30, 31, 32, 33, 39, 40 e 41.

[10] Turner, Christopher J, Alexios A Michailidis, Dmitry A Abanin, Maksym Serbyn e Zlatko Papić: *Weak ergodicity breaking from quantum many-body scars*. Nature

Physics, 14(7):745–749, 2018. Citado 13 vezes nas páginas 12, 17, 21, 22, 24, 28, 29, 30, 31, 32, 33, 35 e 39.

[11] Turner, CJ, AA Michailidis, DA Abanin, Maksym Serbyn e Z Papić: *Quantum scarred eigenstates in a Rydberg atom chain: Entanglement, breakdown of thermalization, and stability to perturbations.* Physical Review B, 98(15):155134, 2018. Citado 7 vezes nas páginas 12, 17, 22, 25, 28, 35 e 40.

[12] Serbyn, Maksym, Zlatko Papić e Dmitry A Abanin: *Local conservation laws and the structure of the many-body localized states.* Physical review letters, 111(12):127201, 2013. Citado 2 vezes nas páginas 12 e 20.

[13] Stöckmann, Hans Jürgen: *Quantum chaos: an introduction*, 2000. Citado na página 15.

[14] Prosen, Tomaž e Marko Robnik: *Energy level statistics in the transition region between integrability and chaos.* Journal of Physics A: Mathematical and General, 26(10):2371, 1993. Citado na página 15.

[15] Bohigas, O, MJ Giannoni e C Schmit: *Spectral properties of the Laplacian and random matrix theories.* Journal de Physique Lettres, 45(21):1015–1022, 1984. Citado na página 15.

[16] Robnik, Marko: *Improved statistics of energy levels for Aharonov-Bohm chaotic billiards.* Journal of Physics A: Mathematical and General, 25(5):1399, 1992. Citado na página 15.

[17] Wilkinson, M, M Feingold e DM Leitner: *Localization and spectral statistics in a banded random matrix ensemble.* Journal of Physics A: Mathematical and General, 24(1):175, 1991. Citado na página 15.

[18] Feingold, Mario e Asher Peres: *Distribution of matrix elements of chaotic systems.* Physical Review A, 34(1):591, 1986. Citado na página 15.

[19] Wilkinson, Michael: *Random matrix theory in semiclassical quantum mechanics of chaotic systems.* Journal of Physics A: Mathematical and General, 21(5):1173, 1988. Citado na página 15.

[20] Wigner, Eugene P: *Characteristic vectors of bordered matrices with infinite dimensions i.* The Collected Works of Eugene Paul Wigner: Part A: The Scientific Papers, páginas 524–540, 1993. Citado na página 15.

[21] Heller, Eric J: *Bound-state eigenfunctions of classically chaotic Hamiltonian systems: scars of periodic orbits.* Physical Review Letters, 53(16):1515, 1984. Citado na página 16.

[22] Serbyn, Maksym, Dmitry A Abanin e Zlatko Papić: *Quantum many-body scars and weak breaking of ergodicity.* Nature Physics, 17(6):675–685, 2021. Citado 5 vezes nas páginas 16, 22, 23, 28 e 40.

[23] Scherg, Sebastian, Thomas Kohlert, Pablo Sala, Frank Pollmann, Bharath Hebbe Madhusudhana, Immanuel Bloch e Monika Aidelsburger: *Observing non-ergodicity due to kinetic constraints in tilted Fermi-Hubbard chains.* Nature Communications, 12(1):1–8, 2021. Citado na página 16.

[24] Choi, Soonwon, Christopher J Turner, Hannes Pichler, Wen Wei Ho, Alexios A Michailidis, Maksym Serbyn, Mikhail D Lukin e Dmitry A Abanin: *Emergent SU(2) dynamics and perfect quantum many-body scars.* Physical Review Letters, 122(22):220603, 2019. Citado 4 vezes nas páginas 17, 24, 43 e 46.

[25] Neumann, John von: *Proof of the ergodic theorem and the H-theorem in quantum mechanics.* The European Physical Journal H, 35(2):201–237, 2010. Citado na página 18.

[26] Goldstein, Sheldon, Joel L Lebowitz, Roderich Tumulka e Nino Zanghì: *Long-time behavior of macroscopic quantum systems.* The European Physical Journal H, 35(2):173–200, 2010. Citado na página 18.

[27] Rigol, Marcos, Vanja Dunjko, Vladimir Yurovsky e Maxim Olshanii: *Relaxation in a completely integrable many-body quantum system: an ab initio study of the dynamics of the highly excited states of 1D lattice hard-core bosons.* Physical review letters, 98(5):050405, 2007. Citado na página 18.

[28] Rigol, Marcos e Mark Srednicki: *Alternatives to eigenstate thermalization.* Physical review letters, 108(11):110601, 2012. Citado 3 vezes nas páginas 18, 19 e 20.

[29] Srednicki, Mark: *Chaos and quantum thermalization.* Physical review e, 50(2):888, 1994. Citado 2 vezes nas páginas 18 e 20.

[30] Turner, Christopher Jack: *Weak ergodicity breaking and quantum scars in constrained quantum systems.* Tese de Doutoramento, University of Leeds, 2019. Citado 3 vezes nas páginas 19, 21 e 33.

[31] Biroli, Giulio, Corinna Kollath e Andreas M Läuchli: *Effect of rare fluctuations on the thermalization of isolated quantum systems.* Physical review letters, 105(25):250401, 2010. Citado na página 19.

[32] D'Alessio, Luca, Yariv Kafri, Anatoli Polkovnikov e Marcos Rigol: *From quantum chaos and eigenstate thermalization to statistical mechanics and thermodynamics.* Advances in Physics, 65(3):239–362, 2016. Citado na página 20.

[33] Babelon, Olivier, Denis Bernard e Michel Talon: *Introduction to classical integrable systems*. Cambridge University Press, 2003. Citado na página 20.

[34] Turner, Christopher J, Konstantinos Meichanetzidis, Zlatko Papić e Jiannis K Pachos: *Optimal free descriptions of many-body theories*. Nature communications, 8(1):1–7, 2017. Citado na página 20.

[35] Sutherland, Beautiful Models: *Years of Exactly Solved Quantum Many-Body Problems*, 2004. Citado na página 20.

[36] Abanin, Dmitry A, Ehud Altman, Immanuel Bloch e Maksym Serbyn: *Colloquium: Many-body localization, thermalization, and entanglement*. Reviews of Modern Physics, 91(2):021001, 2019. Citado na página 20.

[37] Huse, David A, Rahul Nandkishore e Vadim Oganesyan: *Phenomenology of fully many-body-localized systems*. Physical Review B, 90(17):174202, 2014. Citado na página 20.

[38] Basko, Denis M, Igor L Aleiner e Boris L Altshuler: *Metal–insulator transition in a weakly interacting many-electron system with localized single-particle states*. Annals of physics, 321(5):1126–1205, 2006. Citado na página 20.

[39] Pal, Arijeet e David A Huse: *Many-body localization phase transition*. Physical review b, 82(17):174411, 2010. Citado na página 21.

[40] Bluvstein, Dolev, Ahmed Omran, Harry Levine, Alexander Keesling, Giulia Semeghini, Sepehr Ebadi, Tout T Wang, Alexios A Michailidis, Nishad Maskara, W Wei Ho *et al.*: *Controlling quantum many-body dynamics in driven Rydberg atom arrays*. Science, 371(6536):1355–1359, 2021. Citado 2 vezes nas páginas 22 e 24.

[41] Regnault, Nicolas, Sanjay Moudgalya e B Andrei Bernevig: *Quantum many-body scars and hilbert space fragmentation: a review of exact results*. Reports on Progress in Physics, 2022. Citado 2 vezes nas páginas 22 e 23.

[42] Moudgalya, Sanjay, Nicolas Regnault e B Andrei Bernevig: *η-pairing in Hubbard models: From spectrum generating algebras to quantum many-body scars*. Physical Review B, 102(8):085140, 2020. Citado 4 vezes nas páginas 22, 23, 24 e 38.

[43] Langlett, Christopher M, Zhi Cheng Yang, Julia Wildeboer, Alexey V Gorshkov, Thomas Iadecola e Shenglong Xu: *Rainbow scars: From area to volume law*. Physical Review B, 105(6):L060301, 2022. Citado na página 22.

[44] Desaules, Jean Yves, Ana Hudomal, Christopher J Turner e Zlatko Papić: *Proposal for realizing quantum scars in the tilted 1D Fermi-Hubbard model*. Physical Review Letters, 126(21):210601, 2021. Citado 2 vezes nas páginas 23 e 24.

[45] Kim, Hyosub, YeJe Park, Kyungtae Kim, H S Sim e Jaewook Ahn: *Detailed balance of thermalization dynamics in Rydberg-atom quantum simulators.* Physical review letters, 120(18):180502, 2018. Citado na página 23.

[46] Arovas, Daniel P, Erez Berg, Steven A Kivelson e Srinivas Raghu: *The hubbard model.* Annual review of condensed matter physics, 13:239–274, 2022. Citado na página 23.

[47] Mark, Daniel K e Olexei I Motrunich: *η-pairing states as true scars in an extended Hubbard model.* Physical Review B, 102(7):075132, 2020. Citado na página 23.

[48] Affleck, Ian, Tom Kennedy, Elliott H Lieb e Hal Tasaki: *Rigorous results on valence-bond ground states in antiferromagnets.* Condensed Matter Physics and Exactly Soluble Models: Selecta of Elliott H. Lieb, páginas 249–252, 2004. Citado na página 23.

[49] Mark, Daniel K, Cheng Ju Lin e Olexei I Motrunich: *Unified structure for exact towers of scar states in the Affleck-Kennedy-Lieb-Tasaki and other models.* Physical Review B, 101(19):195131, 2020. Citado na página 23.

[50] Moudgalya, Sanjay, Nicolas Regnault e B Andrei Bernevig: *Entanglement of exact excited states of Affleck-Kennedy-Lieb-Tasaki models: Exact results, many-body scars, and violation of the strong eigenstate thermalization hypothesis.* Physical Review B, 98(23):235156, 2018. Citado 2 vezes nas páginas 23 e 24.

[51] Moudgalya, Sanjay, Stephan Rachel, B Andrei Bernevig e Nicolas Regnault: *Exact excited states of nonintegrable models.* Physical Review B, 98(23):235155, 2018. Citado 3 vezes nas páginas 23, 24 e 38.

[52] Iadecola, Thomas e Marko Žnidarič: *Exact localized and ballistic eigenstates in disordered chaotic spin ladders and the Fermi-Hubbard model.* Physical Review Letters, 123(3):036403, 2019. Citado 3 vezes nas páginas 23, 24 e 38.

[53] Dooley, Shane: *Robust quantum sensing in strongly interacting systems with many-body scars.* PRX Quantum, 2(2):020330, 2021. Citado 2 vezes nas páginas 23 e 24.

[54] Desaules, Jean Yves, Francesca Pietracaprina, Zlatko Papić, John Goold e Silvia Pappalardi: *Extensive multipartite entanglement from su (2) quantum many-body scars.* Physical Review Letters, 129(2):020601, 2022. Citado na página 23.

[55] Gillmeister, Konrad, Denis Golež, Cheng Tien Chiang, Nikolaj Bittner, Yaroslav Pavlyukh, Jamal Berakdar, Philipp Werner e Wolf Widdra: *Ultrafast coupled charge and spin dynamics in strongly correlated NiO.* Nature communications, 11(1):4095, 2020. Citado na página 24.

[56] Hu, Wanzheng, Stefan Kaiser, Daniele Nicoletti, Cassandra R Hunt, Isabella Gierz, Matthias C Hoffmann, M Le Tacon, T Loew, B Keimer e Andrea Cavalleri: *Optically enhanced coherent transport in YBa 2 Cu 3 O 6.5 by ultrafast redistribution of interlayer coupling.* Nature materials, 13(7):705–711, 2014. Citado na página 24.

[57] Yuan, Dong, Shun Yao Zhang, Yu Wang, L M Duan e Dong Ling Deng: *Quantum information scrambling in quantum many-body scarred systems.* Physical Review Research, 4(2):023095, 2022. Citado na página 24.

[58] Zhang, Pengfei, Hang Dong, Yu Gao, Liangtian Zhao, Jie Hao, Jean Yves Desaules, Qiujiang Guo, Jiachen Chen, Jinfeng Deng, Bobo Liu *et al.*: *Many-body Hilbert space scarring on a superconducting processor.* Nature Physics, 19(1):120–125, 2023. Citado na página 24.

[59] Wildeboer, Julia, Alexander Seidel, NS Srivatsa, Anne EB Nielsen e Onur Erten: *Topological quantum many-body scars in quantum dimer models on the kagome lattice.* Physical Review B, 104(12):L121103, 2021. Citado na página 24.

[60] McClarty, Paul A, Masudul Haque, Arnab Sen e Johannes Richter: *Disorder-free localization and many-body quantum scars from magnetic frustration.* Physical Review B, 102(22):224303, 2020. Citado na página 24.

[61] Lin, Cheng Ju, Anushya Chandran e Olexei I Motrunich: *Slow thermalization of exact quantum many-body scar states under perturbations.* Physical Review Research, 2(3):033044, 2020. Citado na página 24.

[62] Papić, Zlatko: *Weak ergodicity breaking through quantum many-body scars.* Nature Physics, 17(6):672–673, 2021. Citado na página 24.

[63] Pan, Lei e Hui Zhai: *Composite spin approach to the blockade effect in Rydberg atom arrays.* Physical Review Research, 4(3):L032037, 2022. Citado na página 24.

[64] Labuhn, Henrik, Daniel Barredo, Sylvain Ravets, Sylvain de Léséleuc, Tommaso Macrì, Thierry Lahaye e Antoine Browaeys: *Tunable two-dimensional arrays of single Rydberg atoms for realizing quantum Ising models.* Nature, 534(7609):667–670, 2016. Citado na página 24.

[65] Browaeys, Antoine e Thierry Lahaye: *Many-body physics with individually controlled Rydberg atoms.* Nature Physics, 16(2):132–142, 2020. Citado 2 vezes nas páginas 24 e 25.

[66] Gallagher, T. F.: *Rydberg Atoms.* Cambridge University Press, 1994. Citado na página 24.

[67] Šibalić, Nikola e Charles S Adams: *Rydberg physics*. IOP Publishing, 2018. Citado na página 24.

[68] Saffman, Mark, Thad G Walker e Klaus Mølmer: *Quantum information with Rydberg atoms*. Reviews of modern physics, 82(3):2313–2363, 2010. Citado na página 24.

[69] Robicheaux, Francis e JV Hernández: *Many-body wave function in a dipole blockade configuration*. Physical Review A, 72(6):063403, 2005. Citado na página 25.

[70] Bravyi, Sergey, David P DiVincenzo e Daniel Loss: *Schrieffer–Wolff transformation for quantum many-body systems*. Annals of physics, 326(10):2793–2826, 2011. Citado na página 26.

[71] Sun, Bo e Francis Robicheaux: *Numerical study of two-body correlation in a 1D lattice with perfect blockade*. New Journal of Physics, 10(4):045032, 2008. Citado na página 29.

[72] Olmos, B, R González-Férez e I Lesanovsky: *Collective Rydberg excitations of an atomic gas confined in a ring lattice*. Physical Review A, 79(4):043419, 2009. Citado na página 29.

[73] Hudomal, Ana, Jean Yves Desaules, Bhaskar Mukherjee, Guo Xian Su, Jad C Halimeh e Zlatko Papić: *Driving quantum many-body scars in the PXP model*. Physical Review B, 106(10):104302, 2022. Citado na página 30.

[74] Saad, Yousef: *Iterative Methods for Sparse Linear Systems*. SIAM, 2003. Citado na página 35.

[75] Lin, C J e Soonwon Choi: *Exact quantum many-body scar states in the Rydberg-blockaded atom chain*. Physical Review B, 101(22):220304, 2020. Citado 2 vezes nas páginas 39 e 43.

[76] Schecter, Michael e Thomas Iadecola: *Weak Ergodicity Breaking and Quantum Many-Body Scars in Spin-1 X Y Magnets*. Physical review letters, 123(14):147201, 2019. Citado na página 39.

[77] Hauke, Philipp, Fernando M Cucchietti, Luca Tagliacozzo, Ivan Deutsch e Maciej Lewenstein: *Can one trust quantum simulators?* Reports on Progress in Physics, 75(8):082401, 2012. Citado na página 44.

[78] Gross, Christian e Immanuel Bloch: *Quantum simulations with ultracold atoms in optical lattices*. Science, 357(6355):995–1001, 2017. Citado na página 44.

[79] De Léséleuc, Sylvain, Daniel Barredo, Vincent Lienhard, Antoine Browaeys e Thierry Lahaye: *Analysis of imperfections in the coherent optical excitation of single atoms to Rydberg states*. Physical Review A, 97(5):053803, 2018. Citado na página 44.

[80] Mondragon-Shem, Ian, Maxim G Vavilov e Ivar Martin: *Fate of quantum many-body scars in the presence of disorder*. PRX Quantum, 2(3):030349, 2021. Citado na página 44.

[81] Herb, Konstantin: *Bloch Sphere simulator*. `https://bloch.kherb.io/`, 2023. Accessed: 2024, July 03. Citado na página 45.

[82] O'Dea, Brendan, Wen Wei Ho, Soonwon Choi, Hannes Pichler, Mikhail D. Lukin, Dmitry A. Abanin e Maksym Serbyn: *From tunnels to towers: Quantum scars from Lie algebras and q-deformations*. Physical Review Letters, 125(14):140603, 2020. Citado na página 46.

[83] Khemani, Vedika, Michael Hermele e Rahul M. Nandkishore: *Localization from Hilbert space shattering: From theory to physical realizations*. Physical Review B, 101(17):174204, 2020. Citado na página 46.

[84] Chioquetta, Alessandra e Raphael C Drumond: *Stability of quantum many-body scars on PXP model*. Physica Scripta, 100(6):065980, 2025. Citado na página 48.

[85] Johansson, J.R., P.D. Nation e Franco Nori: *QuTiP: An open-source Python framework for the dynamics of open quantum systems*. Computer Physics Communications, 183(8):1760–1772, 2012, ISSN 0010-4655. `https://www.sciencedirect.com/science/article/pii/S0010465512000835`. Citado na página 48.

[86] Chioquetta, Alessandra: *ScarsProject*, março 2024. `https://github.com/A-Chioquetta/ScarsProject`. Citado 2 vezes nas páginas 48 e 49.

[87] Anderson, P. W.: *Infrared Catastrophe in Fermi Gases with Local Scattering Potentials*. Phys. Rev. Lett., 18:1049, 1967. Citado na página 67.

[88] Quan, H. T., Z. Song, X. F. Liu, P. Zanardi e C. P. Sun: *Decay of Loschmidt Echo Enhanced by Quantum Criticality*. Phys. Rev. Lett., 96:140604, 2006. Citado na página 68.

Apêndices

APÊNDICE A – Schrieffer-Wolff Transformation for the PXP Model: Explicit Derivation

We now present the full derivation of the second-order Schrieffer-Wolff (SW) correction for the PXP model with site-dependent Rabi frequencies Ω_j, leading to an effective flip-flop interaction between neighboring sites, conditioned on the Rydberg blockade.

A.1 Schrieffer-Wolff Formalism: Perturbative Expansion and Equivalence of Approaches

The Schrieffer-Wolff transformation relies on a unitary rotation of the Hamiltonian to eliminate, order by order, the coupling between the constrained subspace $\mathcal{C}$ and its complement $\mathcal{C}^{\perp}$. This is achieved by introducing an anti-Hermitian generator S, such that the effective Hamiltonian becomes:

$$H_{\text{eff}} = e^{S} H e^{-S} = H + [S, H] + \frac{1}{2}[S, [S, H]] + \mathcal{O}(S^3). \tag{A.1}$$

The generator S is chosen to satisfy the decoupling condition at first order:

$$\mathcal{Q}\,(H + [S, H])\,\mathcal{P} = 0, \tag{A.2}$$

where $\mathcal{P}$ and $\mathcal{Q} = 1 - \mathcal{P}$ are projectors onto $\mathcal{C}$ and $\mathcal{C}^{\perp}$, respectively.

Solving this condition for S and substituting back, the second-order correction to the effective Hamiltonian is given by:

$$H_{\text{eff}}^{(2)} = \frac{1}{2}\mathcal{P}[S, V]\mathcal{P}. \tag{A.3}$$

Alternatively, by inserting the explicit expression for S in terms of V and H_0, one can show that this is equivalent to:

$$H_{\text{eff}}^{(2)} = -\frac{1}{2}\mathcal{P}V\frac{1}{H_0}V\mathcal{P}. \tag{A.4}$$

A.2 Schrieffer-Wolff Expansion

Starting from the full Hilbert space, we decompose the Hamiltonian as:

$$H = H_0 + V, \tag{A.5}$$

where H_0 acts entirely within the blockade-forbidden subspace $\mathcal{C}^\perp$ and contains the diagonal energy penalty for violating the Rydberg constraint. While V contains the off-diagonal terms that couple the constrained subspace $\mathcal{C}$ to its complement $\mathcal{C}^\perp$.

Thus, the second-order correction reads:

$$\delta H_{\text{SW}} = -\frac{1}{2}\mathcal{P}V\frac{1}{H_0}V\mathcal{P}. \tag{A.6}$$

A.2.1 Structure of the Perturbation V

The full unconstrained Hamiltonian with site-dependent drives is:

$$H = \sum_j \Omega_j \sigma_j^x. \tag{A.7}$$

The perturbation V contains only the terms that connect $\mathcal{C}$ and $\mathcal{C}^\perp$:

$$V = \sum_j \Omega_j \left(P_j \sigma_j^x Q_j + Q_j \sigma_j^x P_j\right), \tag{A.8}$$

where $P_j = (1 - n_{j-1})(1 - n_{j+1})$ projects onto configurations where site j is allowed to flip without violating the blockade, and $Q_j = 1 - P_j$ projects onto blockade-violating configurations at site j.

A.2.2 Energy Denominator Approximation

Within $\mathcal{C}^\perp$, the dominant energy scale is the cost of having adjacent excitations, denoted by V. For a state with two adjacent excitations, the energy penalty is $2V$, leading to the approximation:

$$\frac{1}{H_0} \approx \frac{1}{2V}. \tag{A.9}$$

A.2.3 Evaluation of the Operator Products

We focus on second-order processes where V acts first on site j, promoting the system to a blockade-violating state at site j or its neighbors, and then returns via action on site k. The relevant term is:

$$-\frac{1}{2}\Omega_j\Omega_k\,\mathcal{P}\left(P_j\sigma_j^x Q_j\frac{1}{2V}Q_k\sigma_k^x P_k\right)\mathcal{P}. \tag{A.10}$$

Due to the locality of V and the blockade constraints, nonzero contributions arise only when $k = j-1$ or $k = j+1$, corresponding to two distinct virtual excitation paths:

- Path 1: First flip at site j, then at $j+1$ (right neighbor).
- Path 2: First flip at site j, then at $j-1$ (left neighbor).

Expanding the spin operators as $\sigma_j^x = \sigma_j^+ + \sigma_j^-$ and projecting back onto $\mathcal{C}$, we obtain for each path:

$$\delta H_{\mathrm{SW}}^{(j+1)} = \frac{\Omega_j\Omega_{j+1}}{8V}\,P_{j-1}\left(\sigma_j^+\sigma_{j+1}^- + \sigma_j^-\sigma_{j+1}^+\right)P_{j+2}, \tag{A.11}$$

and

$$\delta H_{\mathrm{SW}}^{(j-1)} = \frac{\Omega_j\Omega_{j-1}}{8V}\,P_{j+1}\left(\sigma_j^+\sigma_{j-1}^- + \sigma_j^-\sigma_{j-1}^+\right)P_{j-2}. \tag{A.12}$$

A.2.4 Final Compact Form of the Second-Order Correction

After evaluating the contribution from each pair of neighboring sites, the total second-order Schrieffer-Wolff correction takes the form:

$$\delta H_{\mathrm{SW}} = \sum_j\left[\frac{\Omega_j\,\Omega_{j-1}}{8V}\,P_{j+1}\left(\sigma_j^+\sigma_{j-1}^- + \sigma_j^-\sigma_{j-1}^+\right)P_{j-2} + \frac{\Omega_j\,\Omega_{j+1}}{8V}\,P_{j-1}\left(\sigma_j^+\sigma_{j+1}^- + \sigma_j^-\sigma_{j+1}^+\right)P_{j+2}\right]. \tag{A.13}$$

In this expression, the first term corresponds to virtual processes involving sites $(j, j-1)$, while the second term involves $(j, j+1)$. Each contribution includes its own set of projectors to enforce the Rydberg blockade condition.

To express the result in a more compact and symmetric form, the first term can be reindexed by shifting $j \to j+1$, yielding:

$$\sum_j\frac{\Omega_{j+1}\Omega_j}{8V}\,P_{j+2}\left(\sigma_{j+1}^+\sigma_j^- + \sigma_{j+1}^-\sigma_j^+\right)P_{j-1}. \tag{A.14}$$

Combining this reindexed term with the original $(j, j+1)$ contribution, and carefully adjusting the dummy indices, the total correction can be written as:

$$\delta H_{\mathrm{SW}} = \sum_j g_j\,P_{j-1}\left(\sigma_j^+\sigma_{j+1}^- + \sigma_j^-\sigma_{j+1}^+\right)P_{j+2}, \tag{A.15}$$

where the effective site-dependent coupling g_j is:

$$g_j = \frac{\Omega_j \left(\Omega_{j-1} + \Omega_{j+1}\right)}{8V}. \tag{A.16}$$

This compact form makes explicit that both second-order virtual excitation paths, through neighbors $j-1$ and $j+1$, contribute to the flip-flop process between sites j and $j+1$. The presence of the external projectors P_{j-1} and P_{j+2} ensures that the Rydberg blockade condition remains satisfied before and after the action of the operators.

APÊNDICE B – Extra results for $L = 20$

This appendix presents additional simulations performed for a system size of $L = 20$, complementing the results shown in the main chapters for chains up to $L = 18$. Although increasing the system size is in principle desirable for understanding finite-size trends, the computational cost grows significantly with both the system size and the disorder strength. As a consequence, for $L = 20$ it was possible to simulate perturbations only up to $W = 0.05$, instead of $W = 0.1$ used in the main text.

Because the accessible range of perturbation strengths is smaller, the qualitative effects seen at $L = 18$ become much less pronounced at $L = 20$. In particular:

- **For homogeneous perturbations**, the smaller accessible values of W produce a shift in the revival frequency that is still visible, but noticeably more subtle than in the $W \leq 0.1$ cases discussed in the main text.
- **For disordered perturbations**, the dynamics corresponding to different disorder strengths become extremely similar within the available range, making it challenging to distinguish clear differences between curves.
- **Projected vs. non-projected cases** follow the same qualitative trends observed at smaller system sizes, but the contrast between them is significantly reduced due to the limited perturbation strength.

For these reasons, the $L = 20$ results are included here only as supplementary material and are not used to support the main conclusions.

Homogeneous perturbation

This section presents the dynamics under homogeneous perturbations for both projected and non-projected cases.

Projected

Figures 32a and 32b show the fidelity and nearest-neighbor correlation for the projected perturbation.

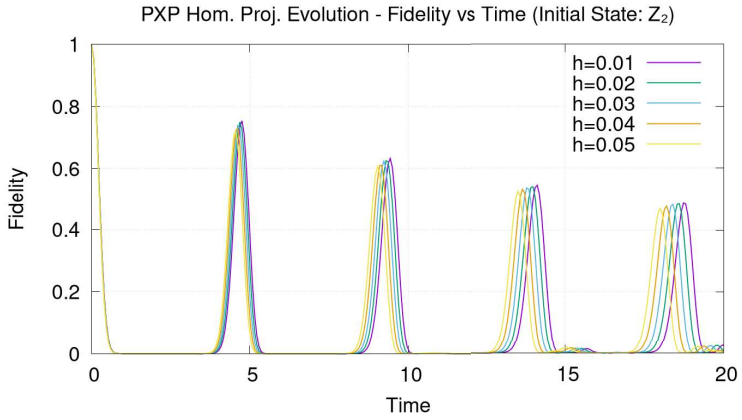

(a)

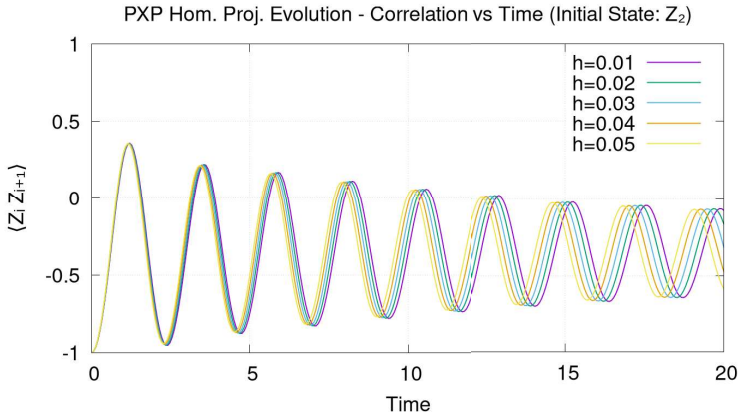

(b)

Figura 32 – (a) Fidelity and (b) nearest-neighbor correlation $C(t)$ for the homogeneous projected perturbation at $L = 20$. The accessible perturbation strengths produce only a small frequency shift, consistent with the observations at $L = 18$.

Non-projected

Figures 33a and 33b show the corresponding results for the non-projected homogeneous perturbation.

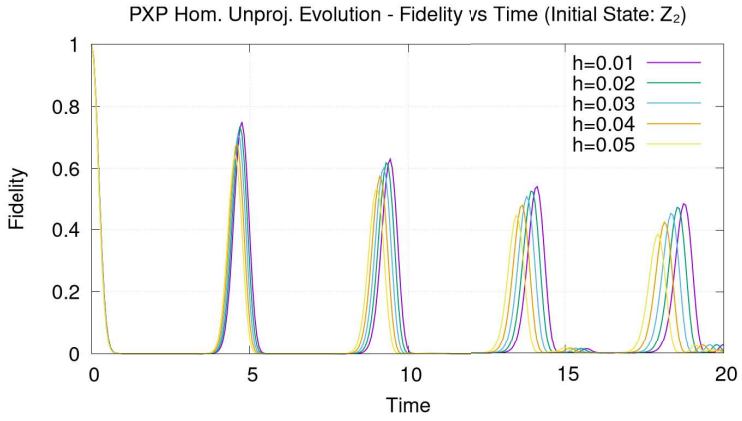

(a)

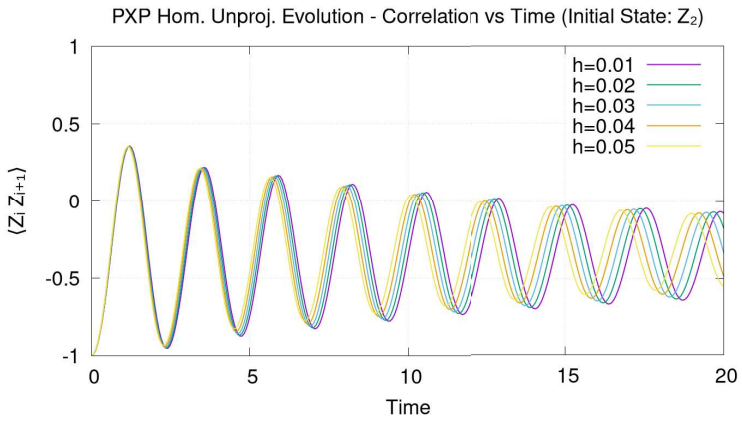

(b)

Figura 33 – (a) Fidelity and (b) nearest-neighbor correlation $C(t)$ for the homogeneous non-projected perturbation at $L = 20$. The decay of the revivals is slightly more pronounced than in the projected case, in agreement with the $L = 18$ results.

Disordered perturbation

This section shows the dynamics with random disorder for both projected and non-projected perturbations.

Projected

Figures 34a and 34b present the time evolution for the disordered projected perturbation.

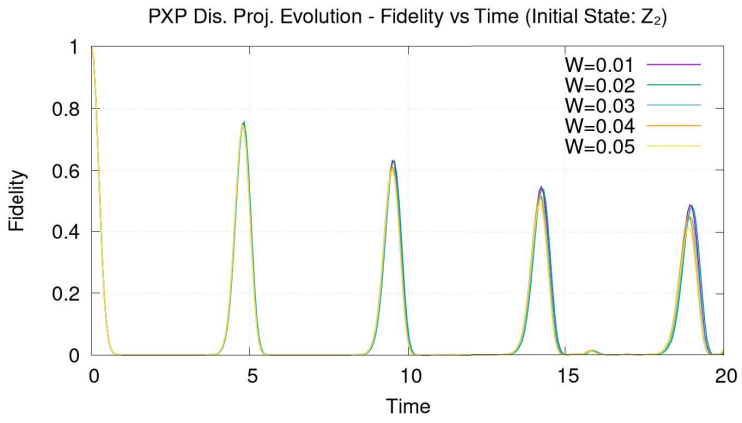

(a)

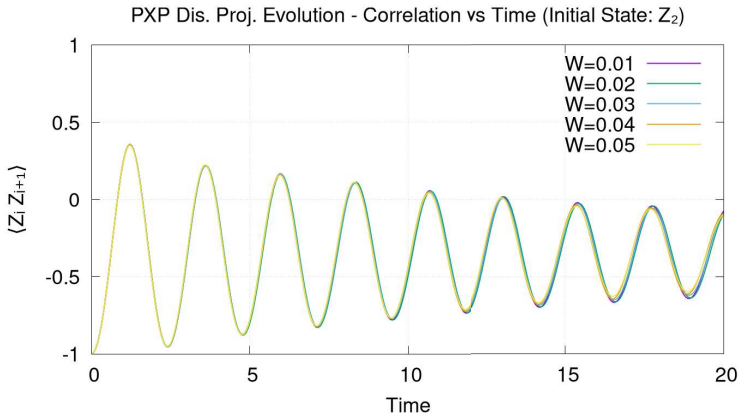

(b)

Figura 34 – (a) Fidelity and (b) nearest-neighbor correlation $C(t)$ for the disordered projected perturbation at $L = 20$. Within the accessible disorder range, the curves show very small differences between disorder strengths, consistent with the global averaging effects discussed in the main conclusions.

Non-projected

Figures 35a and 35b show the corresponding results for non-projected perturbations with disorder.

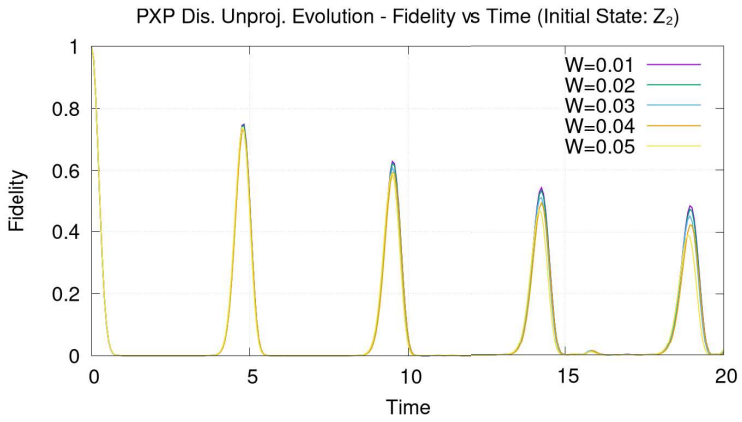

(a)

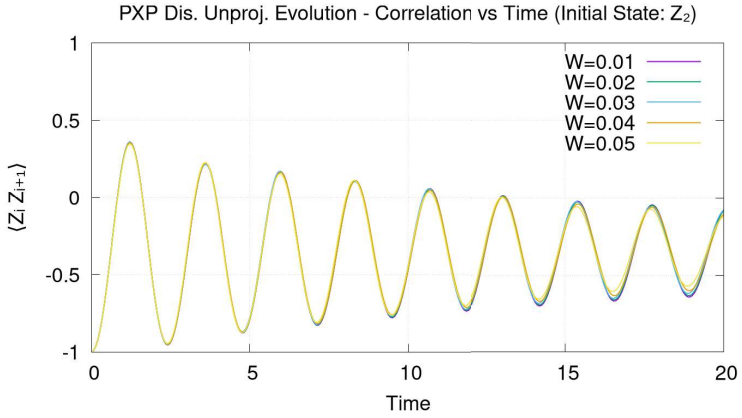

(b)

Figura 35 – (a) Fidelity and (b) nearest-neighbor correlation $C(t)$ for the disordered non-projected perturbation at $L = 20$. The similarity between different W values and between projected and non-projected cases reflects the fact that the disorder dominates the dynamics within the accessible range.